

SOURCE PROCESSES OF SHALLOW AND DEEP EARTHQUAKES AS IMAGED BY THE
BACK-PROJECTION METHOD

by

Haiyang L. Kehoe

Copyright © Haiyang L. Kehoe 2023

A Dissertation Submitted to the Faculty of the

DEPARTMENT OF GEOSCIENCES

In Partial Fulfillment of the Requirements

For the Degree of

DOCTOR OF PHILOSOPHY

In the Graduate College

THE UNIVERSITY OF ARIZONA

2023

THE UNIVERSITY OF ARIZONA
GRADUATE COLLEGE

As members of the Dissertation Committee, we certify that we have read the dissertation

prepared by: Haiyang L. Kehoe

titled: Source Processes of Shallow and Deep Earthquakes as Imaged by the Back-
Projection Method

and recommend that it be accepted as fulfilling the dissertation requirement for the Degree of
Doctor of Philosophy.

Eric D. Kiser

Eric Kiser

Date: Apr 3, 2023

Christopher Harig

Christopher Harig

Date: Apr 3, 2023

Susan L. Beck

Susan Beck

Date: Apr 3, 2023

Roy Johnson

Roy Johnson Apr 3, 2023 14:39 PDT

Roy Johnson

Date: Apr 3, 2023

Final approval and acceptance of this dissertation is contingent upon the candidate's submission
of the final copies of the dissertation to the Graduate College.

I hereby certify that I have read this dissertation prepared under my direction and recommend
that it be accepted as fulfilling the dissertation requirement.



Eric D. Kiser

Eric Kiser

Date: Apr 3, 2023

Department of Geosciences

ACKNOWLEDGEMENTS

This work exists only because of the creativity (and patience) of my advisor, Eric Kiser. From teaching me how to compile FORTRAN code during my first semester of grad school to reading this very dissertation, you have shared the tools, knowledge, and enthusiasm not only necessary to study earthquakes, but to remain excited by such a prospect for a lifetime to come. Thanks also for the water in Joshua Tree after I severely miscalculated my ability to hike the nodes around the middle of a desert wearing jeans and a black t-shirt.

I would also like to thank Susan Beck for inviting me to visit the department when I was still an undergraduate physics student with no real experience in geophysics, and for encouraging me to come to Arizona to learn source seismology despite my lack of interest in seismic tomography! I had to write an entire dissertation on the former to fully appreciate the latter, but I'm excited to use everything I learned in your classes and our group meetings to continue exploring the earth during my post-doc.

This dissertation is the product of countless discussions with current and former GSAT members (Audrey Dunham, Colton Lynner, Daniel Portner, David Moussa, Dani DellaGiustina, Emily Rodriguez, and Sankha Subhra Mahanti)—thank you especially for sharing your GMT scripts when mine would inevitably fail. Those who expanded my research interests by sharing their own (Heather Ford, Amanda Hughes, Michael Kassela, Paul Okubo, Ken Gourley, Min Chen, Han Bao, Cassie Hanagan, Jordan Wang, Tshering Lama Sherpa, Brian Toner, Caden Howlett, Brandon Tober, Tyler Kuehn, Chance Ronemus, Sean Ahdi, Morgan Moschetti, Priscilla Martinez, and Jenna Biegel), thank you.

There are several Arizona professors who made their courses both informative and entertaining. Randy Richardson and George Zandt (Inverse Methods), Roy Johnson (Signal Processing), Chris Harig (Physics of the Earth), and Rick Bennett (Crustal Deformation) provided much of the theoretical and practical knowledge necessary to carry out my research projects in graduate school and beyond.

Kiriaki Xiluri-Lauria deserves a special thank you for keeping my workstation running—no easy task considering the mélange of poorly written code used to complete this dissertation (some of which was mistaken for a computer virus, but that's another story).

To my friends and fellow Arizona Geosciences students, thank you for the help navigating grad school and life in general, but for also making my time at Arizona an immensely enjoyable experience. I'll fondly remember the good times we had across Tucson—everywhere from Gould-Simpson to the Buffet—and I'm looking forward to continuing these memories in new cities as we embark on the next chapters of our lives and careers.

To Jon Topielski, thank you for the steady supply of wisdom and coffee that fueled much of this dissertation and for imparting on me the joy of learning, asking questions, and pursuing a dream. Thank you especially for always helping me be a greener goat.

To Emilia Caylor, Bella, and Porcini—nice to meet you! Thank you for listening to my practice talks, pushing me to do my best, and teaching me how to thrive in difficult and unexpected situations. The next cappuccino is on me.

To my family, my mom and dad, Haixing, Jazz, and Amadeus, thank you for your endless support and encouragement, making this all possible.

TABLE OF CONTENTS

| | |
|--|-----------|
| LIST OF FIGURES | 7 |
| LIST OF TABLES | 9 |
| ABSTRACT | 10 |
| INTRODUCTION | 12 |
| SUMMARY OF WORK | 17 |
| Summary of Methods | 18 |
| Summary of Results | 20 |
| REFERENCES | 31 |
| APPENDIX A: THE RUPTURE PROCESS OF THE 2018 M_W 6.9 HAWAII EARTHQUAKE AS IMAGED BY A GENETIC ALGORITHM-BASED BACK-PROJECTION TECHNIQUE | |
| Abstract | 36 |
| Key Points | 37 |
| Plain Language Summary | 37 |
| 1. Introduction | 38 |
| 2. Methods | 42 |
| 3. Data | 44 |
| 4. Results | 45 |
| 5. Discussion and Conclusions | 48 |
| Acknowledgments | 51 |
| References | 52 |

| | |
|---|------------|
| Supporting Information | 58 |
| Introduction | 58 |
| Text AS1 | 58 |
| Text AS2 | 60 |
| APPENDIX B: EVIDENCE OF A SUPERSHEAR TRANSITION ACROSS A FAULT | |
| STEPOVER | 71 |
| Abstract | 72 |
| Key Points | 72 |
| Plain Language Summary | 72 |
| 1. Introduction | 73 |
| 2. Data and Methods | 76 |
| 3. Regional Back-Projection Result | 78 |
| 4. Independent Supershear Validation | 82 |
| 5. Discussion and Conclusions | 86 |
| Acknowledgments | 90 |
| References | 91 |
| Supporting Information | 98 |
| Introduction | 98 |
| Text BS1 | 98 |
| APPENDIX C: MOMENT-DEPENDENT RUPTURE PROPERTIES OF DEEP-FOCUS | |
| EARTHQUAKES NEAR IZU-BONIN | 110 |
| Abstract | 111 |
| 1. Introduction | 111 |

| | |
|---|------------|
| 2. Data | 115 |
| 3. Methods | 115 |
| 3.1. Conventional back-projection method | 115 |
| 3.2. Genetic algorithm-based station selection method | 117 |
| 3.3. Image deconvolution back-projection method | 118 |
| 3.4. Average rupture velocity vector | 121 |
| 3.5. Nodal plane classification | 122 |
| 3.6. Estimation of the back-projection smearing artifact | 123 |
| 3.7. Earthquake rupture validation with teleseismic data | 124 |
| 3.8. Summary of Methods | 124 |
| 4. Results | 126 |
| 4.1. Regional back-projection results | 126 |
| 4.2. Teleseismic back-projection results | 132 |
| 5. Discussion | 133 |
| 5.1. Moment-length scaling, b values, and fractal dimension | 133 |
| 5.2. Rupture properties | 141 |
| 5.3. Fault plane orientations | 145 |
| 6. Conclusions | 149 |
| References | 153 |
| Supporting Information | 163 |
| Introduction | 163 |
| Text CS1. | 163 |

LIST OF FIGURES

| | |
|---|----|
| Figure 1. Composite map of study regions. | 17 |
| Figure 2. Genetic algorithm source image improvement. | 19 |
| Figure 3. Summary of the 2018 Hawai‘i mainshock back-projection results. | 22 |
| Figure 4. Summary of the 2017 Komandorsky Islands mainshock back-projection results. | 25 |
| Figure 5. Summary of the Izu-Bonin deep-focus back-projection results in map view. | 28 |
| Figure 6. Summary of the Izu-Bonin deep-focus back-projection results in cross-section. | 30 |
| | |
| Figure A1. Geographic map of Hawai‘i. | 41 |
| Figure A2. Distribution of stations. | 42 |
| Figure A3. Summary of results. | 48 |
| Figure AS1. Synthetic test of a spatial jump in the location of slip. | 63 |
| Figure AS2. Synthetic test of a bilateral rupture. | 64 |
| Figure AS3. Genetic algorithm population evolution. | 65 |
| Figure AS4. Genetic algorithm source image improvement. | 66 |
| Figure AS5. Detailed distribution of stations in (a) Japan, (b) Alaska, and (c) the continental United States. | 67 |
| Figure AS6. Synthetic point source tests. | 68 |
| Figure AS7. Synthetic point source tests with and without southern hemisphere stations. | 69 |
| | |
| Figure B1. Geographic map of the study area and the back-projection station distribution. | 74 |
| Figure B2. Summary of the 2017 Komandorsky Islands mainshock back-projection results. | 81 |
| Figure B3. Far-field surface wave observations for supershear rupture validation. | 85 |

| | |
|--|-----|
| Figure B4. Schematic representation of the southeastern rupture of the 2017 Komandorsky Islands earthquake. | 88 |
| Figure BS1. Genetic algorithm optimization curve. | 101 |
| Figure BS2. Genetic algorithm source image improvement. | 102 |
| Figure BS3. Mainshock frequency dependence. | 103 |
| Figure BS4. Teleseismic station distribution and back-projection result. | 104 |
| Figure BS5. Epicentral distances of back-projection source locations as a function of time. | 106 |
| Figure BS6. Back-projection locations of aftershocks along the southeastern rupture. | 107 |
| | |
| Figure C1. Overview of the study area. | 114 |
| Figure C2. Summary of the back-projection method using the 2013 Mw 6.5 mainshock event as an example. | 125 |
| Figure C3. Map summarizing the regional back-projection results. | 130 |
| Figure C4. Cross-sections associated with the dashed lines in Figure C3. | 132 |
| Figure C5. Moment-length plot for the rupture lengths constrained by the regional back-projection method. | 141 |
| Figure C6. The relationship between (a) moment magnitude and rupture trend and (b) moment magnitude and the absolute value of rupture plunge. | 145 |
| Figure C7. Moment relationships with fault plane (a) strike, (b) dip, and (c) rake. | 149 |
| Figure CS1. Synthetic IDBP results using deconvolution events located at different depths. | 166 |
| Figure CS2. Rupture and smearing properties of the mainshock events imaged by this study. | 166 |
| Figure CS3. Map summarizing the global back-projection results. | 168 |
| Figure CS4. Double couple components of the mainshock events imaged in this study. | 169 |

LIST OF TABLES

| | |
|--|-----|
| Table C1. Nodal plane classification criteria. | 122 |
| Table C2. Reported mainshock event properties. | 127 |
| Table C3. Mainshock rupture properties determined by the regional back-projection analysis. | 127 |
| Table C4. Nodal plane classifications. | 128 |
| Table C5. Summary of observed b values and moment magnitude ranges from previous studies (Mao et al., 2022; Zhan, 2017) using global compilations of earthquake catalogs near warm subduction zones (including South America, the Philippines, Japan-Kuril, and Izu-Bonin- Mariana). | 139 |
| Table CS1. Back-projection grid volume dimensions and spacing for each mainshock presented in this study. | 170 |
| Table CS2. Alignment events used for each mainshock back-projection analysis. | 171 |
| Table CS3. Station selection events used for each mainshock back-projection analysis. | 171 |
| Table CS4. Mainshock rupture properties determined by the teleseismic back-projection analysis. | 172 |
| Table CS5. Epsilon (GCMT) and percent DC (USGS) values indicating the double couple component of each mainshock events imaged in this study. | 172 |

ABSTRACT

The physical mechanisms governing earthquakes clarify the dynamic processes at Earth's plate boundaries and inform the evaluation of global seismic hazards. One effective method of interrogating these mechanisms involves imaging earthquake source processes with the back-projection method, which time-reverses seismograms recorded at arrays of seismometers to determine the spatiotemporal evolution of the sources of seismic waves. This method benefits from dense and large aperture arrays and has therefore gained considerable utility with the advent of seismic networks such as the Hi-net array in Japan and the USArray in North America. As instrumentation has improved, so have the techniques enhancing the resolution of back-projection images. Such developments in instrumentation and methodology have discerned increasingly finer scale details of the largest earthquake ruptures and lowered the magnitude threshold required to determine the finite source processes of smaller earthquakes.

This dissertation outlines improvements to the back-projection method that image the rupture properties of earthquakes across diverse depth ranges and tectonic environments. First, a novel genetic algorithm-based back-projection technique using data recorded at teleseismic distance windows (30° – 90°) images the complex source process of the 2018 Mw 6.9 Hawai'i earthquake, revealing the heterogenous frictional properties of the décollement hosting this event and informing hazard estimates of future large magnitude events near Kīlauea (Appendix A). Second, the acceleration of the 2017 Mw 7.7 Komandorsky Islands earthquake to supershear speeds across a fault stepover is observed for the first time in nature using a similar back-projection method and regional (0° – 35°) seismic data (Appendix B). This type of supershear transition, having only been previously documented by numerical modeling efforts, has significant implications on the evaluation of the elevated seismic hazards associated with

supershear earthquakes, particularly in analog tectonic environments near large population centers (e.g., the San Andreas Fault). Third, an image deconvolution back-projection method benefitting from the previously described station selection method at regional distance windows (0° – 21°), is used to constrain the rupture properties of 19 $M_w > 6$ deep-focus (hypocentral depth > 300 km) earthquakes near Izu-Bonin (Appendix C). The location of these events beneath the Hi-net array in Japan resolves each source process in three spatial dimensions and time. We find evidence that rupture direction depends on reported seismic moment and attribute this observation to a change in the prevailing causal mechanism of deep-focus earthquakes at a critical seismic moment, itself a function of the thickness of the metastable olivine wedge within the interior of the subducting Izu-Bonin slab. This study, only made possible by the methodological improvements developed throughout this dissertation, illuminates details of deep-focus earthquakes that have remained enigmatic since their discovery.

INTRODUCTION

The seismic waves generated by earthquakes are recorded by seismometers distributed across the surface of the earth. These observations have long informed the tectonic processes responsible for earthquakes as well as the natural hazards resulting from them. The establishment of early seismic networks provided direct constraints on the source of seismic waves and produced numerous major discoveries advancing the field of seismology. The detection of earthquakes at increasingly lower magnitudes established the relationship between earthquake frequency and magnitude (Gutenberg & Richter, 1944). The routine location of earthquake hypocenters revealed the boundaries of Earth's tectonic plates (e.g., Barazangi & Dorman, 1969) and the presence of subducting slabs accommodating deep earthquakes (Wadati, 1928). The systematic determination of focal mechanisms confirmed the double-couple source model and contextualized patterns of earthquake slip within the emerging theory of plate tectonics (e.g., Isacks et al., 1968; Sykes, 1967). Accurate hypocenters and focal mechanisms were crucial to the validation and development of plate tectonics, an effort largely supported by robust seismic networks such as the World-Wide Standardized Seismographic Network (WWSSN). The uniform instrumentation, regular calibration procedures, and accessible data sharing practices established by the WWSSN set a precedent for modern networks that continue to operate on much of the same principles (Agnew, 2002).

A keystone of modern seismology is the near real-time analysis of data recorded by seismic networks following an earthquake. The calculation of origin times, hypocenters, magnitudes, and focal mechanisms provides crucial information guiding disaster response efforts and the evaluation of secondary hazards such as tsunamis and landslides. While earthquakes are often approximated as simple point sources to allow the rapid determination and dissemination

of this information, real earthquakes often exhibit complexity in both space and time, propagating along faults over finite distances and time intervals. Earthquakes can exhibit considerable source complexity, often spanning multiple segments of natural fault systems at various rupture speeds. Kinematic descriptions of the entire earthquake source process and the detailed quantification of rupture properties (e.g., rupture speed, direction, length, duration) remains crucial not only to our understanding of the physical processes controlling earthquakes, but the assessment of associated hazards.

Earthquake source processes are constrained using a variety of methods and geophysical observations (e.g., seismic, geodetic, tsunami). Finite-fault slip models determine the kinematic evolution of slip on a fault but require assumptions of the fault plane and rupture velocity to invert for the location and timing of slip (e.g., Hartzell & Heaton, 1983; Ji et al., 2002; Olson & Apsel, 1982). Fault plane dimensions, orientation, and geometry are approximated using centroid moment tensor solutions, aftershock locations, empirical fault scaling relationships, mapped faults, and context of the surrounding tectonic environment. Rupture velocities are obtained from alternate methods (e.g., Lay et al., 2017; Ye et al., 2016) or otherwise approximated as a function of the hypocentral depth and duration (e.g., Goldberg et al., 2022; Koch et al., 2019) where shallower depths and longer durations between the origin and centroid times typically indicate slower rupture velocities. While finite-fault slip inversions are frequently and often rapidly performed (e.g., Hayes, 2011; Hayes et al., 2011), the *a priori* information required by this approach fails to characterize earthquakes that occur on complex fault systems with nonuniform rupture velocities. Finite-fault models of deep earthquakes are further limited by the absence of mapped fault systems and the relative scarcity of aftershocks that may otherwise outline seismogenic zones (Frohlich, 2006). The slip distributions identified by finite-fault inversion

methods may differ among published studies despite adequate fitting of the observed data and uncertainties in final models likely arise from subjective selections of data, model parameters, and inversion techniques (Beresnev, 2003; Mai et al., 2016). Independent source imaging methods such as the back-projection method therefore complement (and occasionally guide) finite-fault modeling studies.

The back-projection method images complex earthquake source processes across diverse tectonic environments and depths (e.g., Ishii et al., 2005; Kiser et al., 2011; Kiser & Ishii, 2017; Krüger & Ohrnberger, 2005; Meng et al., 2014). The method requires no *a priori* assumptions of fault geometry nor rupture velocity, and no formal inversion of the seismic data occurs. Instead, grid points are initialized near a hypocenter and predicted travel times are calculated between each grid point and station using a reference Earth velocity model. At each grid point, seismograms recorded by the array are time-reversed by their predicted travel times and stacked. At the locations and times where seismic energy originates, time-shifted seismograms will constructively interfere and produce high-amplitude features. Elsewhere, time-shifted seismograms will destructively interfere and produce low-amplitude features. The subsequent back-projection result characterizes the spatiotemporal evolution of the earthquake source process.

The first back-projection studies imaged the extensive ~1,200 km long rupture of the 2004 Mw 9.1 Sumatra-Andaman earthquake using *P* waves recorded at teleseismic distance windows (30° – 90°) to minimize interference with other seismic phases (Ishii et al., 2005; Krüger & Ohrnberger, 2005). Back-projection studies using global networks (e.g., the Global Seismographic Network) benefit from the extensive aperture and uniform orientation of globally distributed stations with respect to any recorded earthquake, but the large station spacing of

global networks results in ray paths that transit highly heterogenous Earth structure, thus degrading the coherent arrival of waveforms across the array as well as the resolution of the final source models. The combination of dense regional seismic arrays maintains much of the waveform coherence observed across single arrays while benefiting from improved distance and azimuthal station coverage (Kiser & Ishii, 2012, 2017). Studies following this approach perform isolated back-projection analyses using the individual arrays before applying array-specific weights and time-shifts that normalize the contribution of each array and maximize the coherency of the combined result. The incorporation of all available seismic data in a back-projection analysis is therefore problematic because waveform coherency, station spacing, and array coverage must all be considered to optimize the resolution of earthquake source models.

The larger relative aperture of seismic arrays at closer regional distance windows ($< 30^\circ$) may resolve greater rupture complexity than teleseismic back-projection studies, but data recorded at regional distances are susceptible to artifacts caused by the arrival of unwanted seismic phases (e.g., mantle transition zone triplications, depth phases). Smearing artifacts, emerging as high-amplitude features along the ray path that propagate at the speed of the seismic phase used in the back-projection analysis (Kiser & Ishii, 2017), may also degrade back-projection resolution. Smearing along teleseismic ray paths with steep takeoff angles prevents conventional back-projection analyses from resolving the depth-dependent rupture process, and instead, such studies ignore the depth direction altogether to focus on the lateral extent of rupture. Data recorded at regional distance windows may otherwise resolve the depth-dependent rupture process, especially in cases where ray paths with both upward and downward takeoff angles from the source are captured by the array, but data containing incoherent arrivals from unwanted seismic phases must first be removed.

The work presented in this dissertation aims to improve the resolution of back-projection images by removing the seismic data responsible for artifacts obscuring the real source properties of earthquakes. In parallel with global improvements in seismic instrumentation, the internet and open data sharing policies have made seismic data both abundant and accessible. Array-processing methods such as back-projection, however, may be encumbered by incoherent, noisy, or otherwise flawed data that inhibit the determination of earthquake source processes. This is in large part due to the heterogenous Earth, imposing imperfect station coverage across its surface and muddling seismic waves traveling through its interior. Unraveling the rupture properties of earthquakes and the tectonic processes producing them not only requires the continued expansion of seismic observatories, but the development of novel methods that make full use of these growing datasets.

SUMMARY OF WORK

The following sections summarize the methodological improvements and subsequent results obtained by each of the three appended studies comprising this dissertation (Appendices A–C). The geographic regions of each study are combined in Figure 1.

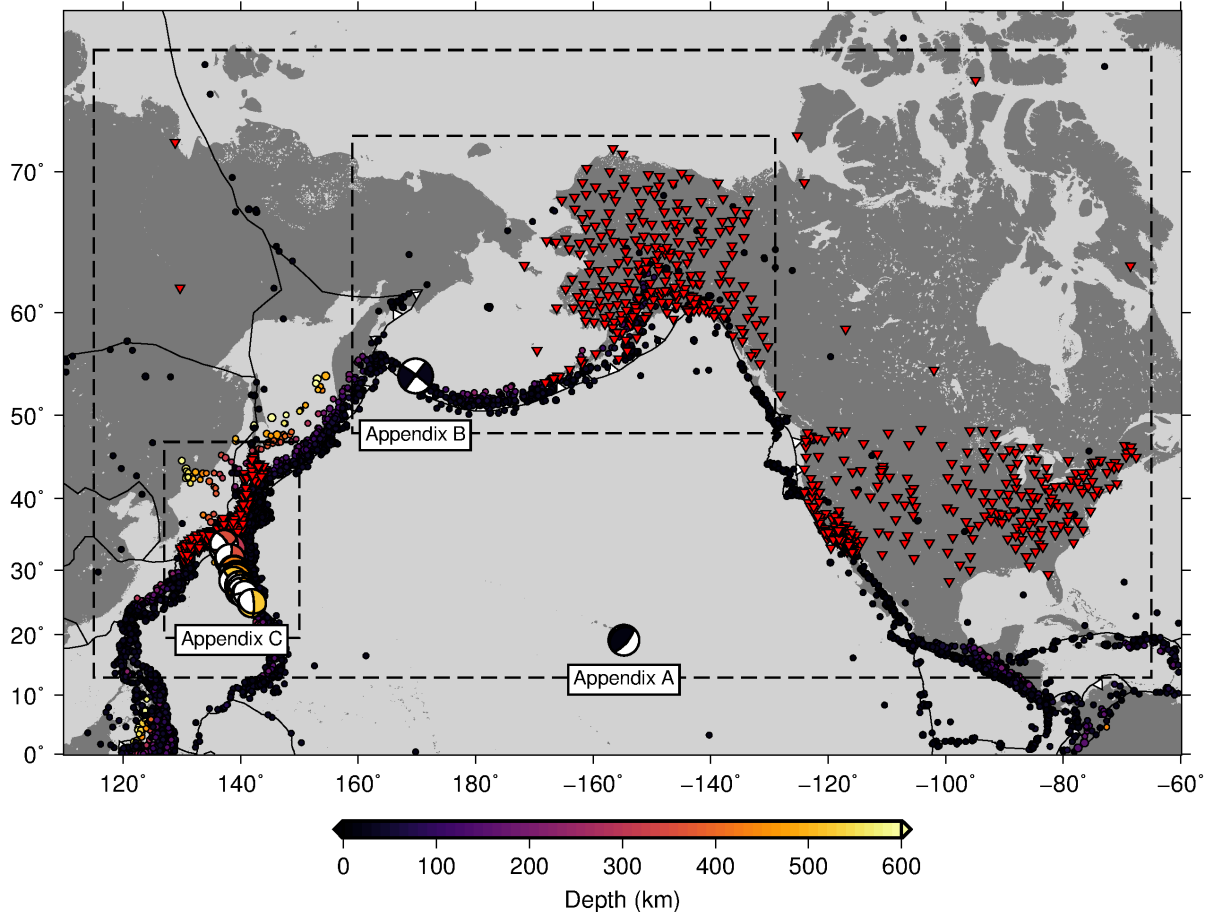


Figure 1. Composite map of study regions. Individual study areas are enclosed by dashed black boxes. The Global Centroid Moment Tensor (GCMT: Dziewonski et al., 1981; Ekström et al., 2012) solutions are colored by event depth and show the locations of the events imaged throughout this dissertation. The red triangles show the locations of the stations used in each study. The magnitude-scaled depth-colored circles show seismicity with magnitude greater

than 5 between the years 2000–2020 as cataloged by the International Seismological Centre (ISC; Bondár & Storchak, 2011).

Summary of Methods

This dissertation improves upon the back-projection method by implementing algorithmic approaches to seismic array design and digital image processing that minimize potential artifacts in resulting models of earthquake source processes. A novel genetic algorithm-based station selection method is developed to find a subset of stations that reduces back-projection artifacts resulting from the combination of teleseismic distributions of stations (Appendix A) and the use of regional distributions of stations (Appendices B–C). Small magnitude earthquakes have small rupture areas and durations, and the back-projection method should therefore resolve small events as point sources in space and time. A reasonable assumption can be made that any imaged energy outside of this spatiotemporal point source is the result of artifacts uncharacteristic of the true source process. The genetic algorithm-based station selection method operates on this principle by searching for a subset of stations that images a small magnitude reference event near the mainshock hypocenter as a point source. An optimal subset of stations can be found by brute force, but such a process requires exponential increases in computational time with linear increases in the number of total stations from which a subset is desired. Modern dense seismic networks continuously record seismic data at hundreds of stations, necessitating the use of a genetic algorithm (Holland, 1992) that efficiently solves this problem by finding a near-optimal subset of stations imaging a small magnitude reference event as a point source (Figure 2). The same subset of stations is then used to resolve the mainshock rupture process, removing any data responsible for artifacts obscuring the true

earthquake source process. This station selection procedure is applied to each study presented in this dissertation, automatically selecting data that improves the spatiotemporal resolution of back-projection source models and revealing rupture complexity that informs our understanding of earthquake and tectonic processes.

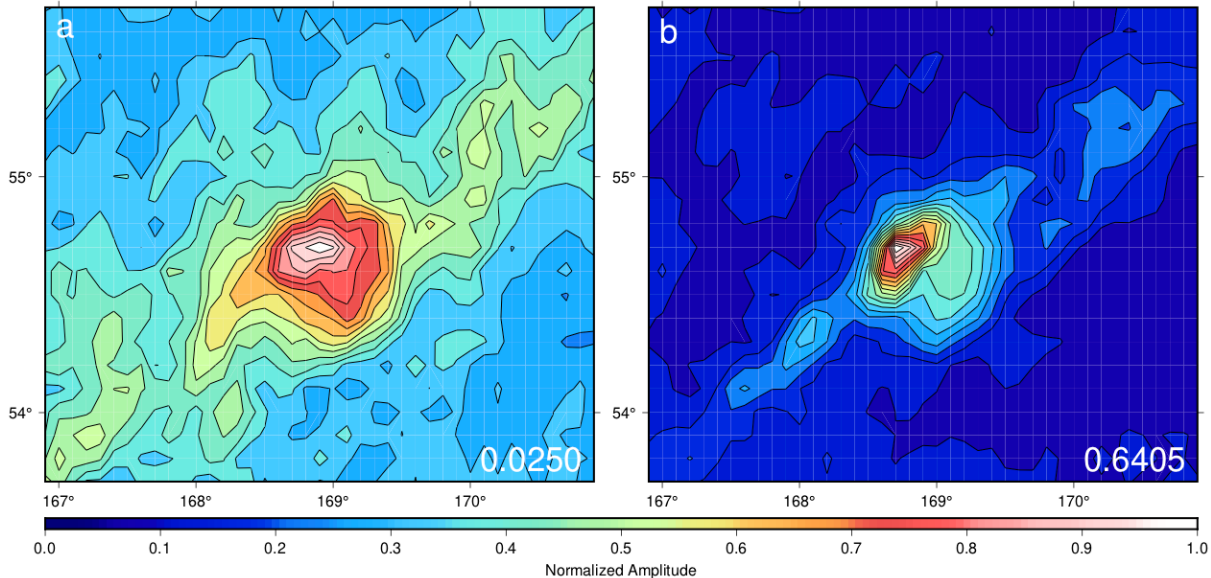


Figure 2. Genetic algorithm source image improvement. The genetic algorithm-based station selection method is applied to a nearby magnitude 5.1 foreshock of the Mw 7.7 Komandorsky Islands earthquake. (a) The back-projection result of the foreshock with the full seismic network. (b) The back-projection result of the foreshock with the optimized seismic network. The fitness of each result, which approaches one for a perfect spatiotemporal point source, is displayed in the bottom right corner of each panel.

An image deconvolution back-projection method following Wang et al. (2016) is implemented to systematically constrain the first order rupture properties of deep-focus earthquakes near Izu-Bonin (Appendix C). The proximity of the Hi-net array in Japan provides unprecedented constraints on the depth-dependent rupture process of the deep-focus earthquakes

in this region but smearing artifacts resulting from imperfect station coverage degrade the lateral resolution of the back-projection results. Conventional back-projection images are the convolution of the seismic array response and the discrete earthquake source process. Again invoking the idea that small magnitude events are resolved by the back-projection method as spatiotemporal point sources, the array response is approximated by imaging a small magnitude reference event. Severe artifacts represented by this estimated array response are removed from the mainshock back-projection result by image deconvolution, revealing the true sources of radiated seismic energy. Ruptures in this region are subsequently imaged in three spatial dimensions and time, informing our understanding of the mechanisms controlling deep-focus earthquakes.

Summary of Results

The first study (Appendix A) investigates the 2018 Mw 6.9 Hawai‘i earthquake, which occurred near the south flank of Kīlauea during an intense episode of volcanic activity. Large magnitude events in this region likely occur on a décollement that separates the volcanic edifice of Kīlauea from the underlying oceanic crust. The improved spatiotemporal resolution provided by the genetic algorithm-based back-projection technique reveals a complex source process consisting of four distinct rupture segments. The primary feature of this earthquake involves a slow, westward propagating rupture segment that overlaps with previously observed slow slip events (Figure 3), indicating that stress accumulation on the décollement is not completely relieved by these slow slip events alone. Future large magnitude events in this region may generate both strong ground shaking and tsunami waves impacting populated areas and infrastructure on the island of Hawai‘i. Precise constraints on the areas of the décollement most

likely to rupture and experience significant amounts of slip directly supports the estimation of seismic and tsunami hazards near Kīlauea.

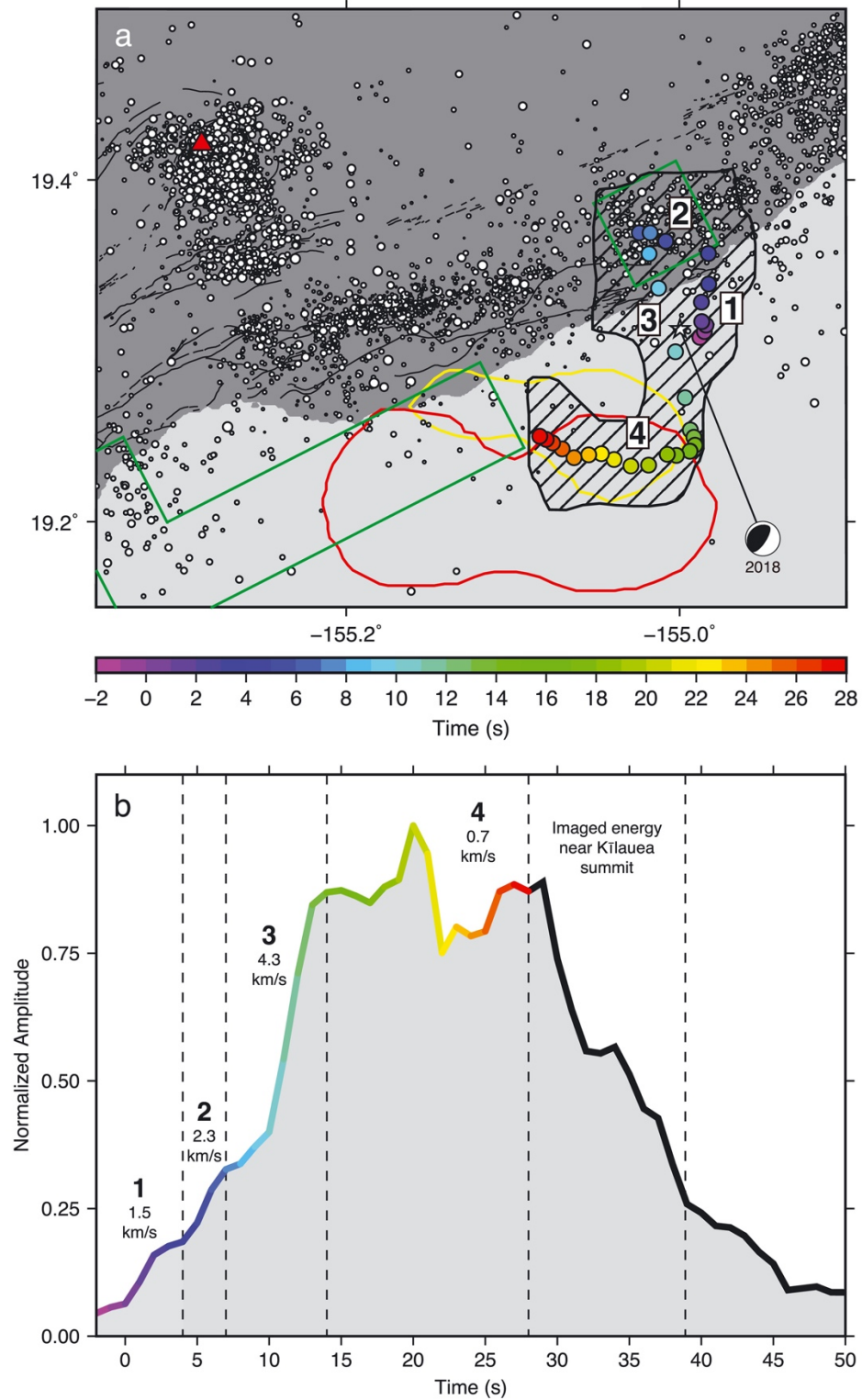


Figure 3. Summary of the 2018 Hawai‘i mainshock back-projection results. (a) The rainbow dots, determined from a coherence-based back-projection approach (Ishii, 2011), show the central source locations of the 2018 Mw 6.9 earthquake. The color of the dots indicates rupture time with respect to the hypocentral time (0 s). The individual segments of the overall rupture are labeled in white boxes. The white star is the National Earthquake Information Center epicenter, and black hatched area shows the estimated rupture area of the imaged earthquake. The red and yellow lines show the locations of periodic and aperiodic slow slip events, respectively (Foster et al., 2013). The green boxes show the distribution of largest slip (greater than 10 m) from the 1975 Mw 7.7 event (Owen & Bürgmann, 2006). The magnitude-scaled white dots show the post-mainshock seismicity located by the Hawaiian Volcano Observatory (<https://doi.org/10.7914/SN/HV>). The black lines are faults. The dark and light gray background areas show onshore and offshore regions, respectively. (b) The normalized amplitude of high-frequency energy release as a function of time, determined from the linear back-projection result, is shown for the 2018 Mw 6.9 earthquake. The rainbow line of the source time function corresponds to the rainbow dots used in (a). The western rupture (Segment 4) shows the highest normalized amplitude.

The second study (Appendix B) uses a similar genetic algorithm-based station selection method and data recorded at regional distance windows (0° – 35°) to analyze the 2017 Mw 7.7 Komandorsky Islands earthquake. The improved method resolves earthquake propagation across multiple fault segments indicative of a fault stepover system. The rupture accelerates to supershear speeds, or in excess of the local shear wave speed, following a rupture jump across two offset fault segments (Figure 4). Supershear ruptures are often coincident with planar strike-

slip faults, but numerical modeling efforts additionally indicate the feasibility of supershear transitions across complex fault systems (e.g., Ryan & Oglesby, 2014). The detailed rupture process constrained by the back-projection method using an optimal seismic array reveals the first observation of a supershear transition across a fault stepover in nature. Supershear earthquakes elevate seismic hazard by producing strong ground motion at far distances from the ruptured fault. Understanding the mechanisms responsible for supershear earthquakes is critical to the evaluation of seismic hazards in all strike-slip environments.

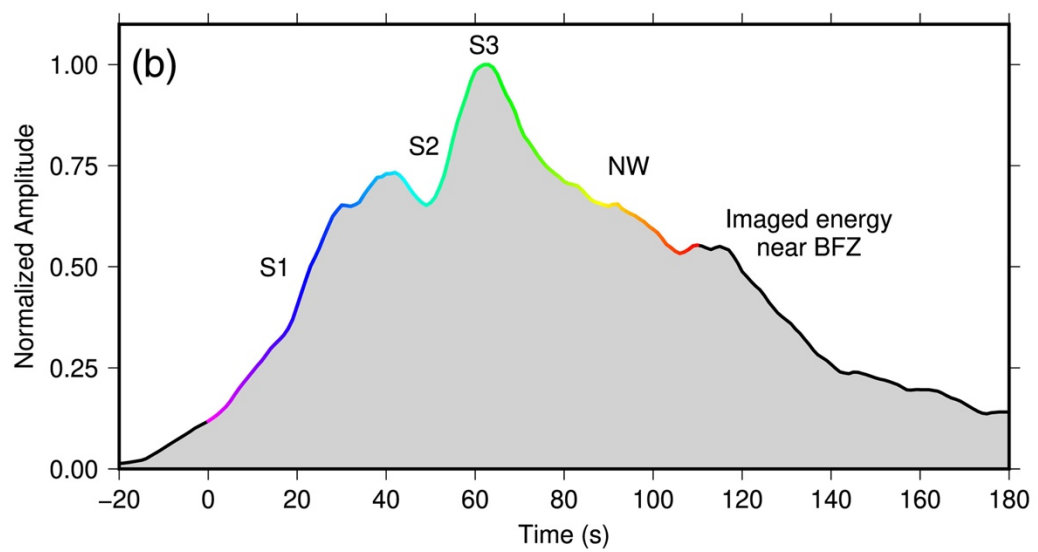
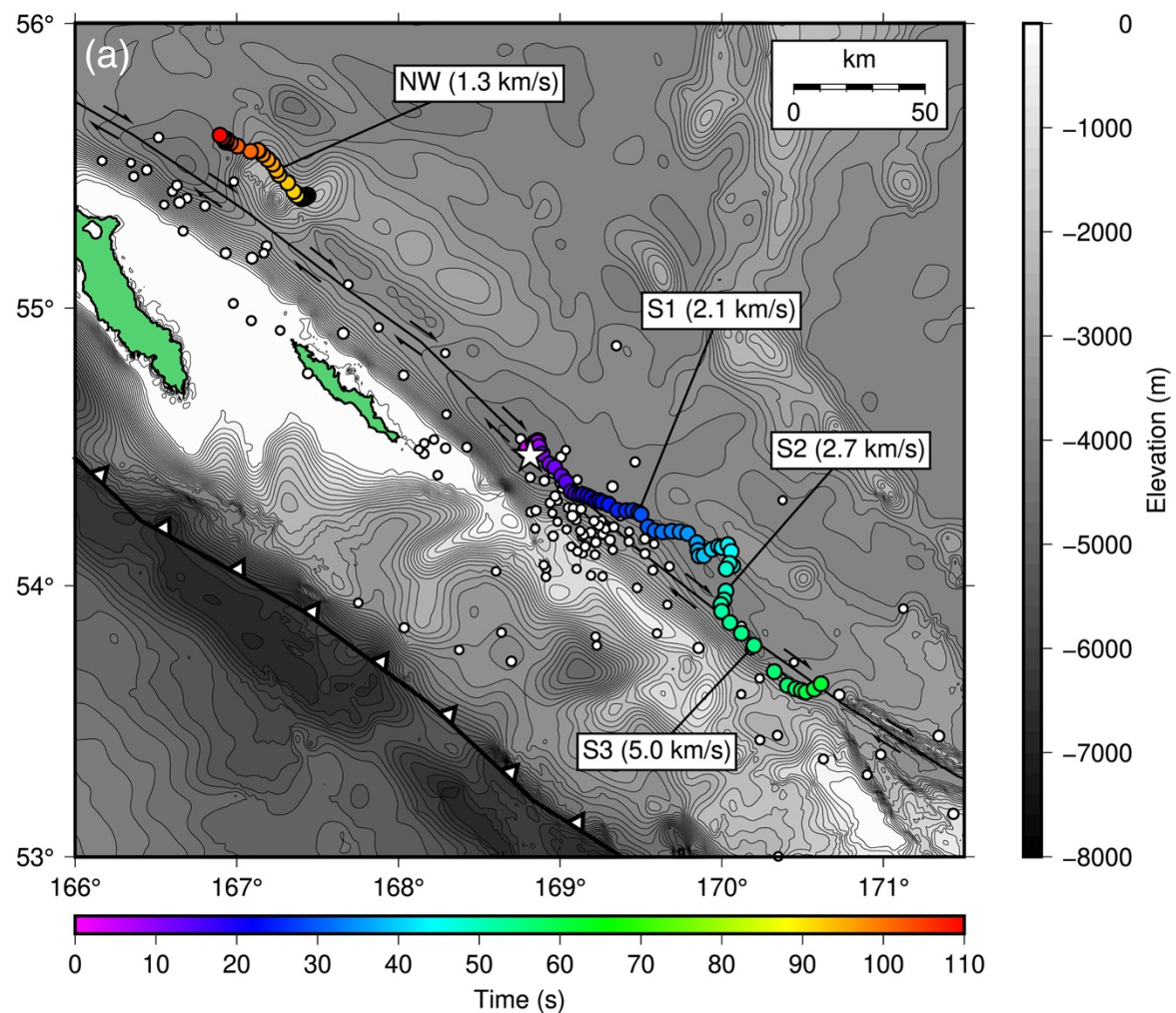


Figure 4. Summary of the 2017 Komandorsky Islands mainshock back-projection results. (a) The white star shows the epicenter of the 2017 Komandorsky Islands earthquake. The rainbow dots are determined from the coherence-based back-projection result using the optimized network and show the central source locations of the mainshock rupture. The color of the dots indicates the time with respect to origin time (0 s). The labels S1, S2, and S3 show the locations of the first, second, and third segments of the southeastern rupture, respectively. The label NW shows the location of the imaged northwestern rupture. Bathymetry contours are plotted every 200 m. The Aleutian Trench is shown as a black line with white triangles on the overriding plate. The Bering Fracture Zone (BFZ) is shown as a black line with right-lateral strike-slip arrows. The area between the Aleutian Trench and BFZ is the Komandorsky Sliver. The two green islands are the Komandorsky Islands. The magnitude scaled white dots are aftershocks above magnitude 4 for three weeks after the mainshock. (b) The normalized amplitude of energy release as a function of time is determined from the linear back-projection result and shown for the 2017 Komandorsky Islands earthquake. The rainbow line of the source time function and the labels correspond to the rainbow dots and labels used in (a).

The third study (Appendix C) images the rupture process of deep-focus earthquakes near Izu-Bonin. An image deconvolution back-projection method, an optimal subset of Hi-net stations in Japan, and a three-dimensional velocity model are used to determine the rupture properties of 19 Mw 6.0–7.1 earthquakes in this region (Figures 5–6). The fault plane orientations of 10 events are uniquely determined by comparing the imaged rupture processes with independently determined nodal planes of GCMT solutions. The rupture properties and fault plane orientations of each event classify according to their reported moment magnitude, implicating two distinct

moment-dependent physical mechanisms governing deep-focus earthquakes in this region. Deep-focus earthquakes are studied less than their shallow counterparts, but robust instrumentation and improved methodological approaches image their source processes in greater detail and to lower magnitudes. The determination of source processes reveals the physical mechanisms by which deep-focus earthquakes operate, information that remains crucial to our understanding of slab structure and subduction zone dynamics.

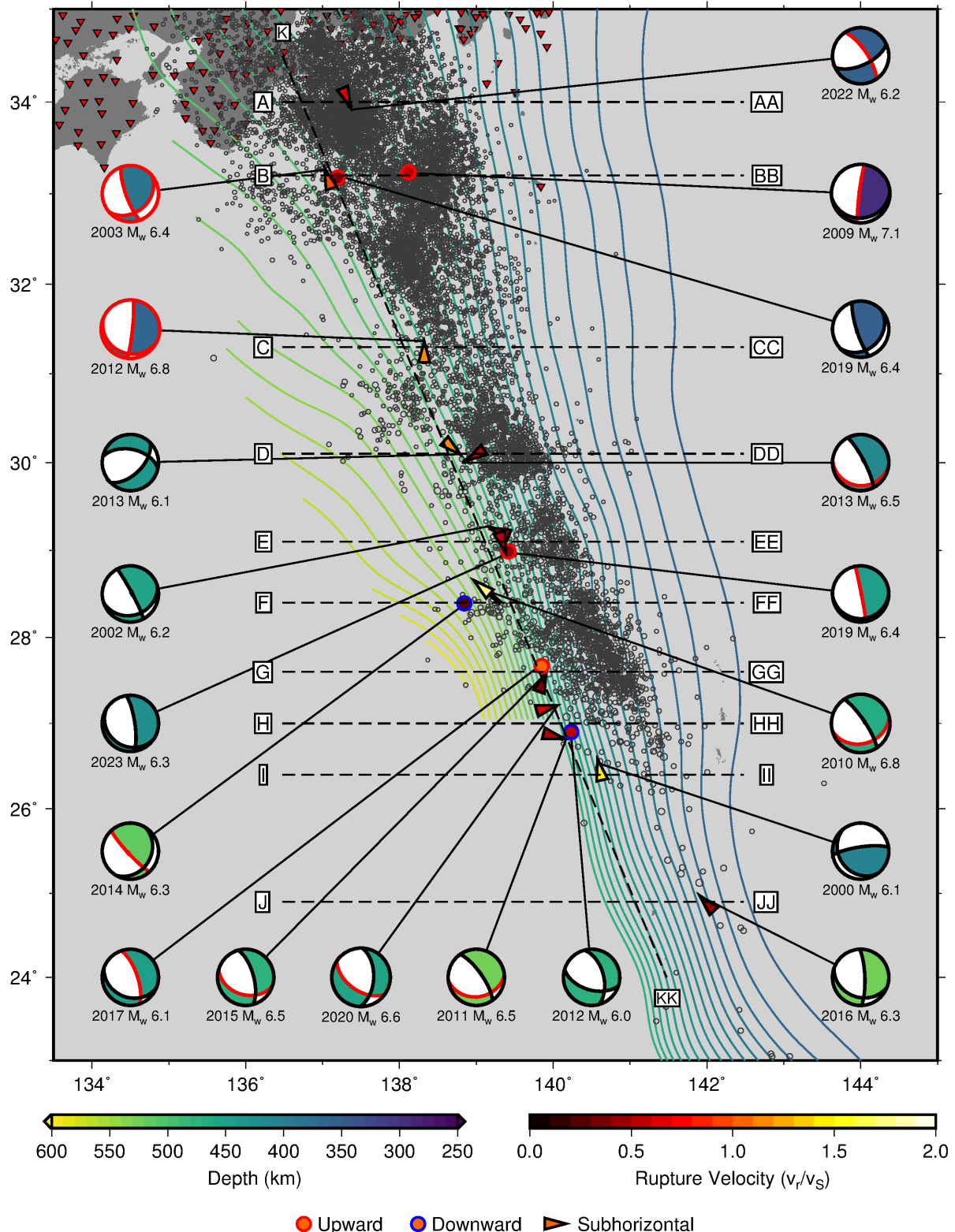


Figure 5. Summary of the Izu-Bonin deep-focus back-projection results in map view. The red triangles show the locations of Hi-net stations. The depth-colored contours show the subducting slabs (Hayes et al., 2018). The magnitude-scaled black open circles show all Japan Meteorological Agency (JMA: https://www.data.jma.go.jp/svd/eqev/data/bulletin/hypo_e.html) cataloged seismicity with depths greater than 250 km between the years 2000–2020. The colored arrows and circles show the rupture speed and direction as determined by the regional back-projection analysis. Arrows are used for subhorizontal ruptures ($\leq 45^\circ$) while circles are used for subvertical ruptures ($> 45^\circ$). The arrows and circles are colored by their rupture velocity, normalized to the local shear wave speed at the observed rupture depth. Upward propagating ruptures are outlined in red, downward propagating ruptures are outlined in blue, and subhorizontally propagating ruptures are outlined in black. The depth-colored GCMT solutions associated with each event are plotted at the edges of the figure for clarity. Nodal planes of the GCMT solutions are colored according to the nodal plane classification scheme. A single red nodal plane indicates rupture on that single fault plane, two red nodal planes indicate rupture on both nodal planes, and two black nodal planes indicate rupture on neither nodal plane. The labeled dashed lines show the locations of the 11 cross-sections shown in Figure 6.

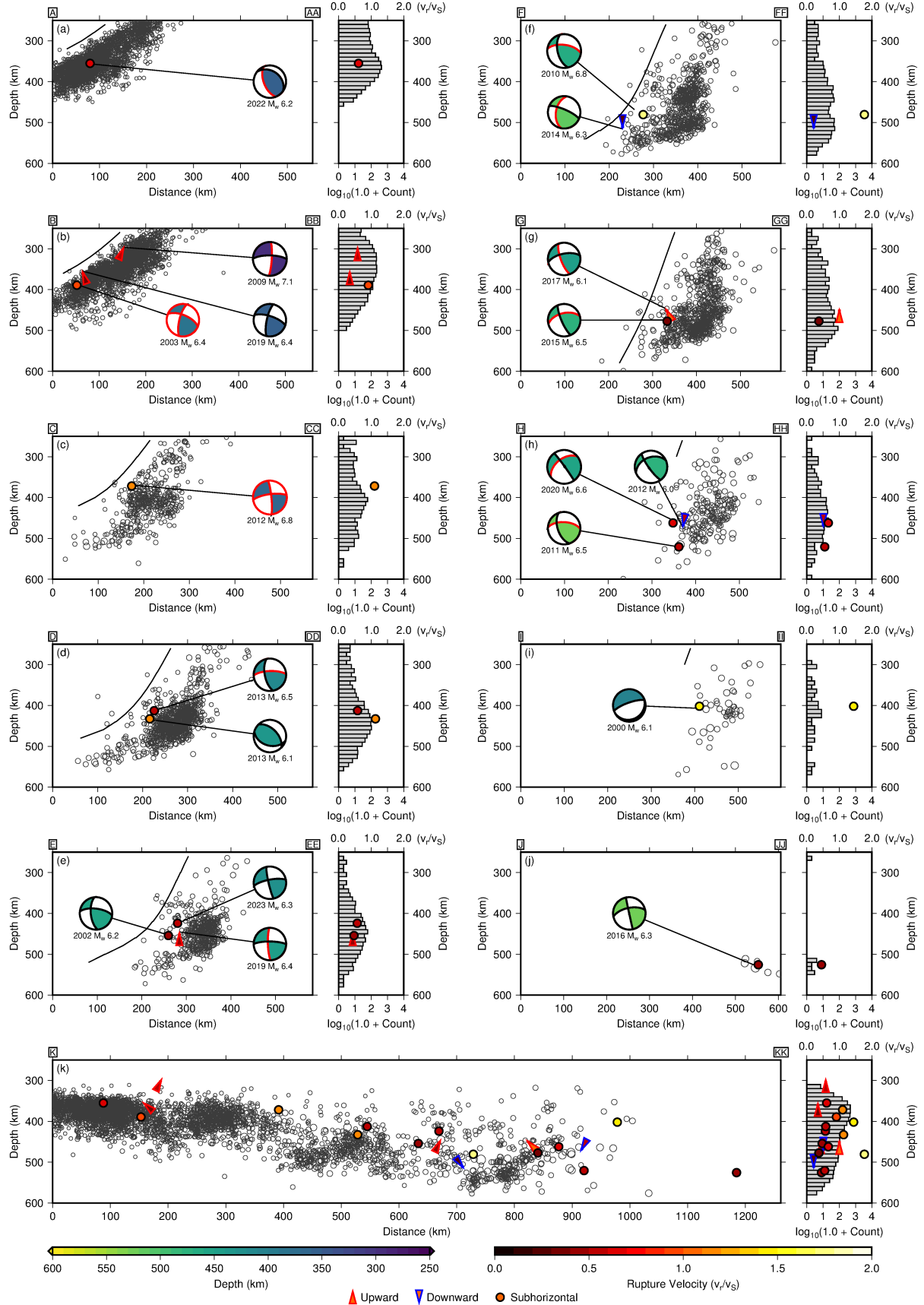


Figure 6. Summary of the Izu-Bonin deep-focus back-projection results in cross-section. (a–k)

Within each geographic cross-section plot (left of each subpanel), a black line showing the slab, magnitude-scaled black open circles showing JMA seismicity, colored GCMT solutions, and colored rupture vectors are projected onto the vertical plane of each cross-section. Nodal planes of the GCMT solutions are colored according to the nodal plane classification scheme. A single red nodal plane indicates rupture on that single fault plane, two red nodal planes indicate rupture on both nodal planes, and two black nodal planes indicate rupture on neither nodal plane. A histogram (right of each subpanel) shows the depth dependence of JMA seismicity within 50 km of the cross-section. Rupture velocities associated with the mainshock events of each cross-section are plotted on top of the JMA background seismicity histogram. Upward propagating ruptures are shown as arrows outlined in red, downward propagating ruptures are shown as arrows outlined in blue, and subhorizontally propagating ruptures are shown as circles outlined in black.

Earthquakes, while represented on most maps as a single point in space and time, exhibit a considerable degree of rupture complexity. Ruptures may extend hundreds of kilometers over several minutes, span multiple segments of a complex fault system, and exhibit broad ranges of rupture speeds and directions. As Appendices A–C will show, detailed source models reveal the physical properties of the faults that host earthquakes and the causal mechanisms that govern them, thereby informing our understanding of tectonic processes and their associated hazards.

REFERENCES

- Agnew, D. C. (2002). History of Seismology. In *IASPEI International Handbook of Earthquake and Engineering Seismology* (pp. 3–13).
- Barazangi, M., & Dorman, J. (1969). World seismicity maps compiled from ESSA, Coast and Geodetic Survey, epicenter data, 1961–1967. *Bulletin of the Seismological Society of America*, 59(1), 369–380. <https://doi.org/10.1785/BSSA0590010369>
- Beresnev, I. A. (2003). Uncertainties in Finite-Fault Slip Inversions: To What Extent to Believe? (A Critical Review). *Bulletin of the Seismological Society of America*, 93(6), 2445–2458. <https://doi.org/10.1785/0120020225>
- Bondár, I., & Storchak, D. (2011). Improved location procedures at the International Seismological Centre. *Geophysical Journal International*, 186(3), 1220–1244. <https://doi.org/10.1111/J.1365-246X.2011.05107.X>
- Dziewonski, A. M., Chou, T.-A., & Woodhouse, J. H. (1981). Determination of earthquake source parameters from waveform data for studies of global and regional seismicity. *Journal of Geophysical Research: Solid Earth*, 86(B4), 2825–2852. <https://doi.org/10.1029/JB086iB04p02825>
- Ekström, G., Nettles, M., & Dziewoński, A. M. (2012). The global CMT project 2004–2010: Centroid-moment tensors for 13,017 earthquakes. *Physics of the Earth and Planetary Interiors*, 200–201, 1–9. <https://doi.org/10.1016/J.PEPI.2012.04.002>
- Foster, J. H., Lowry, A. R., & Brooks, B. A. (2013). Fault frictional parameters and material properties revealed by slow slip events at Kilauea volcano, Hawai‘i. *Geophysical Research Letters*, 40(23), 6059–6063. <https://doi.org/10.1002/2013GL058234>

- Frohlich, C. (2006). *Deep Earthquakes*. Cambridge University Press.
<https://doi.org/10.1017/CBO9781107297562>
- Goldberg, D. E., Koch, P., Melgar, D., Riquelme, S., & Yeck, W. L. (2022). Beyond the Teleseism: Introducing Regional Seismic and Geodetic Data into Routine USGS Finite-Fault Modeling. *Seismol. Res. Lett.*, 93, 3308–3323. <https://doi.org/10.1785/0220220047>
- Gutenberg, B., & Richter, C. F. (1944). Frequency of earthquakes in California. *Bulletin of the Seismological Society of America*, 34(4), 185–188.
<https://doi.org/10.1785/BSSA0340040185>
- Hartzell, S. H., & Heaton, T. H. (1983). Inversion of strong ground motion and teleseismic waveform data for the fault rupture history of the 1979 Imperial Valley, California, earthquake. *Bulletin of the Seismological Society of America*, 73(6A), 1553–1583.
<https://doi.org/10.1785/BSSA07306A1553>
- Hayes, G. P. (2011). Rapid source characterization of the 2011 M w 9.0 off the Pacific coast of Tohoku Earthquake. *LETTER Earth Planets Space*, 63, 529–534.
<https://doi.org/10.5047/eps.2011.05.012>
- Hayes, G. P., Moore, G. L., Portner, D. E., Hearne, M., Flamme, H., Furtney, M., & Smoczyk, G. M. (2018). Slab2, a comprehensive subduction zone geometry model. *Science*, 362(6410), 58–61. <https://doi.org/10.1126/science.aat4723>
- Hayes, G. P., Team, the U. E. R., Earle, P. S., Team, the U. E. R., Benz, H. M., Team, the U. E. R., Wald, D. J., Team, the U. E. R., Briggs, R. W., & Team, the U. E. R. (2011). 88 Hours: The U.S. Geological Survey National Earthquake Information Center Response to the 11 March 2011 Mw 9.0 Tohoku Earthquake. *Seismological Research Letters*, 82(4), 481–493.
<https://doi.org/10.1785/GSSRL.82.4.481>

Holland, J. H. (1992). *Adaptation in natural and artificial systems: an introductory analysis with applications to biology, control, and artificial intelligence*. MIT press.

Isacks, B., Oliver, J., & Sykes, L. R. (1968). *Seismology and the New Global Tectonics*. 75(18).

<https://doi.org/10.1029/JB073i018p05855>

Ishii, M. (2011). High-frequency rupture properties of the Mw 9.0 off the Pacific coast of Tohoku Earthquake. *Earth, Planets and Space*, 63(7), 609–614.

<https://doi.org/10.5047/eps.2011.07.009>

Ishii, M., Shearer, P. M., Houston, H., & Vidale, J. E. (2005). Extent, duration and speed of the 2004 Sumatra-Andaman earthquake imaged by the Hi-Net array. *Nature*, 435(7044), 933–936. <https://doi.org/10.1038/nature03675>

Ji, C., Wald, D. J., & Helmberger, D. v. (2002). Part I: Wavelet Domain Inversion Theory and Resolution Analysis. *Bulletin of the Seismological Society of America*, 92(4), 1192–1207.
<http://pubs.geoscienceworld.org/ssa/bssa/article-pdf/92/4/1192/2715647/1192.pdf>

Kiser, E., & Ishii, M. (2012). Combining seismic arrays to image the high-frequency characteristics of large earthquakes. *Geophys. J. Int.*, 188, 1117–1128.
<https://doi.org/10.1111/j.1365-246X.2011.05299.x>

Kiser, E., & Ishii, M. (2017). Back-Projection Imaging of Earthquakes. *Annual Review of Earth and Planetary Sciences*, 45(1), 271–299. <https://doi.org/10.1146/annurev-earth-063016-015801>

Kiser, E., Ishii, M., Langmuir, C. H., Shearer, P. M., & Hirose, H. (2011). Insights into the mechanism of intermediate-depth earthquakes from source properties as imaged by back projection of multiple seismic phases. *Journal of Geophysical Research: Solid Earth*, 116(6). <https://doi.org/10.1029/2010JB007831>

- Koch, P., Bravo, F., Riquelme, S., & Crempien, J. G. F. (2019). Near-Real-Time Finite-Fault Inversions for Large Earthquakes in Chile Using Strong-Motion Data. *Seismological Research Letters*, 90(5), 1971–1986. <https://doi.org/10.1785/0220180294>
- Krüger, F., & Ohrnberger, M. (2005). Tracking the rupture of the $M_w = 9.3$ Sumatra earthquake over 1,150 km at teleseismic distance. *Nature*, 435(7044), 937–939. <https://doi.org/10.1038/nature03696>
- Lay, T., Ye, L., Bai, Y., Cheung, K. F., Kanamori, H., Freymueller, J., Steblov, G. M., & Kogan, M. G. (2017). Rupture Along 400 km of the Bering Fracture Zone in the Komandorsky Islands Earthquake (MW 7.8) of 17 July 2017. *Geophysical Research Letters*, 44(24), 12,161–12,169. <https://doi.org/10.1002/2017GL076148>
- Mai, P. M., Schorlemmer, D., Page, M., Ampuero, J. P., Asano, K., Causse, M., Custodio, S., Fan, W., Festa, G., Galis, M., Gallovic, F., Imperatori, W., Käser, M., Malytskyy, D., Okuwaki, R., Pollitz, F., Passone, L., Razafindrakoto, H. N. T., Sekiguchi, H., ... Zielke, O. (2016). The Earthquake-Source Inversion Validation (SIV) Project. *Seismological Research Letters*, 87(3), 690–708. <https://doi.org/10.1785/0220150231>
- Meng, L., Ampuero, J. P., & Bürgmann, R. (2014). The 2013 Okhotsk deep-focus earthquake: Rupture beyond the metastable olivine wedge and thermally controlled rise time near the edge of a slab. *Geophysical Research Letters*, 41(11), 3779–3785. <https://doi.org/10.1002/2014GL059968>
- Olson, A. H., & Apsel, R. J. (1982). Finite faults and inverse theory with applications to the 1979 Imperial Valley earthquake. *Bulletin of the Seismological Society of America*, 72(6A), 1969–2001. <https://doi.org/10.1785/BSSA07206A1969>

- Owen, S. E., & Bürgmann, R. (2006). An increment of volcano collapse: Kinematics of the 1975 Kalapana, Hawaii, earthquake. *Journal of Volcanology and Geothermal Research*, 150(1–3), 163–185. <https://doi.org/10.1016/j.jvolgeores.2005.07.012>
- Ryan, K. J., & Oglesby, D. D. (2014). Dynamically modeling fault step overs using various friction laws. *Journal of Geophysical Research: Solid Earth*, 119(7), 5814–5829. <https://doi.org/10.1002/2014JB011151>
- Sykes, L. R. (1967). Mechanism of earthquakes and nature of faulting on the mid-oceanic ridges. *Journal of Geophysical Research*, 72(8), 2131–2153. <https://doi.org/10.1029/JZ072I008P02131>
- Wadati, K. (1928). Shallow and deep earthquakes. *Geophys. Mag.*, 1(1), 162–202.
- Wang, D., Takeuchi, N., Kawakatsu, H., & Mori, J. (2016). Estimating high frequency energy radiation of large earthquakes by image deconvolution back-projection. *Earth and Planetary Science Letters*, 449, 155–163. <https://doi.org/10.1016/J.EPSL.2016.05.051>
- Ye, L., Lay, T., Zhan, Z., Kanamori, H., & Hao, J. L. (2016). The isolated ~680 km deep 30 May 2015 MW 7.9 Ogasawara (Bonin) Islands earthquake. *Earth and Planetary Science Letters*, 433, 169–179. <https://doi.org/10.1016/J.EPSL.2015.10.049>

APPENDIX A: THE RUPTURE PROCESS OF THE 2018 M_w 6.9 HAWAII EARTHQUAKE AS IMAGED BY A GENETIC ALGORITHM-BASED BACK-PROJECTION TECHNIQUE

H. L. Kehoe¹, E. D. Kiser¹, P. G. Okubo²

¹Department of Geosciences, University of Arizona, Tucson, AZ, USA

²Hawaiian Volcano Observatory, U.S. Geological Survey, Hawaii National Park, HI, USA

The text, figures, and supporting information included in this appendix were previously published as:

Kehoe, H. L., E. D. Kiser, & P. G. Okubo (2019). The rupture process of the 2018 Mw 6.9 Hawai'i earthquake as imaged by a genetic algorithm-based back-projection technique. *Geophysical Research Letters*, 46, 2467–2474. <https://doi.org/10.1029/2018GL080397>

Abstract

An episode of unrest began at Kīlauea in April 2018 that produced both significant volcanic output and high rates of seismicity, including a Mw 6.9 earthquake on 4 May 2018. In this study, we image the rupture process of this earthquake using a genetic algorithm-based back-projection technique. The dominant feature of the earthquake is a slowly propagating western rupture, which shares similar characteristics with the region's largest recorded event in 1975 (Mw 7.7). The location of this western segment suggests that small asperities on this section of the décollement that frequently fail as slow slip events may achieve seismic slip rates when rupture is initiated on adjacent sections of the fault. Given the interaction between volcanic and seismic activity in this region, imaging the rupture properties of these events can improve our understanding of future geologic hazards in this region.

Key Points

- The complex rupture process of the 2018 Mw 6.9 Hawai‘i earthquake is imaged using a genetic algorithm-based back-projection technique
- The dominant high-frequency feature of this earthquake is a slow western propagating rupture that overlaps with previous slow slip events
- These rupture properties can be explained by slip on a décollement composed of soft sediments with small velocity-weakening asperities

Plain Language Summary

Voluminous lava flows and explosive eruptions at Kīlauea Volcano in Hawai‘i have captured the attention of the media and general public during the past year. In the early stages of

this volcanic activity, a magnitude 6.9 earthquake occurred beneath the south flank of Kīlauea, which was the second largest earthquake recorded by modern instrumentation in this region. The research presented in the manuscript uses a novel source imaging technique to study the fine-scale spatiotemporal evolution of the rupture that produced this event. The details of this rupture provide new insight into the relationship between fault properties, background seismicity, slow slip events, and major earthquakes in volcanic settings.

1. Introduction

Since 1983, nearly continuous volcanic activity within the East Rift Zone (ERZ), known as the Pu‘u ‘Ō‘ō eruption, has produced large quantities of lava that has remade the landscape of eastern Hawai‘i. On 3 May 2018, a new episode of lava output began in the lower ERZ located near the eastern corner of Hawai‘i. Twenty-four separate fissures formed during this activity, and as of 9 August 2018, 35.5 km² of land has been affected by the resulting lava flows (Neal et al., 2019). This activity is also associated with several minor explosive eruptions from the Kīlauea summit, which generated earthquakes with moment magnitudes as large as 5.4 (U.S. Geological Survey National Earthquake Information Center [NEIC]:

<https://earthquake.usgs.gov/earthquakes/eventpage/hv70219637/executive>). Several earthquakes also occurred along the ERZ associated with the movement of magma in the subsurface. Away from both the summit and ERZ, the largest earthquake during this episode (Mw 6.9) occurred on 4 May 2018 beneath the south flank of Kīlauea (22:32:54 UTC, 19.318°N 155.000°W, depth 5.8 km; NEIC: <https://earthquake.usgs.gov/earthquakes/eventpage/us1000dyad/executive>).

The hypocenter of this earthquake is similar to other large ($M_w > 6.0$) events that have occurred in this region, and it has been argued that slip during these events takes place on the décollement (7- to 13-km depth) that separates the overlying volcanic edifice of Kīlauea from the underlying oceanic crust (Crosson & Endo, 1982; Denlinger & Okubo, 1995). This low-angle décollement dips northwest toward the center of the Hawai‘i Island and likely extends southeast 30–50 km offshore to a topographic bench (Denlinger & Okubo, 1995). Several studies have concluded that motion on the décollement is driven by injection of magma into the East and Southwest Rift Zones (Denlinger & Okubo, 1995; Dvorak et al., 1986; Swanson et al., 1976), though gravitational forces may also be important (Denlinger & Morgan, 2014). The 1975 $M_w 7.7$ Kalapana earthquake was the largest earthquake on the décollement recorded by modern instruments (Nettles & Ekström, 2004). Events of this magnitude can significantly change the stress state of the Kīlauea magmatic system, and it is thought that increased extensional stresses in the ERZ associated with the 1975 earthquake resulted in a prolonged period of reduced volcanic output (Cayol et al., 2000; Denlinger & Morgan, 2014). In addition to abundant seismicity on sections of the décollement, this surface also hosts aseismic creep (Owen et al., 2000) and slow slip events (Brooks et al., 2006; Foster et al., 2013; Montgomery-Brown et al., 2009, 2013; Poland et al., 2010; Segall et al., 2006; Syracuse et al., 2010). These slow slip events have equivalent magnitudes between 5.3 and 6.0 (Montgomery-Brown et al., 2013) and occur off the southern coast of Kīlauea where little seismicity is typically observed.

The NEIC hypocenter and the global centroid-moment-tensor focal mechanism (Ekström et al., 2012) of the 2018 $M_w 6.9$ earthquake suggest that this earthquake occurred on the low-angle décollement (Figure A1). In this study, the rupture properties of this event are investigated using the back-projection method, which time shifts and stacks waveforms recorded at

teleseismic distances to a grid of potential source locations to determine where seismic sources are located as a function of time (Ishii et al., 2005; Krüger & Ohrnberger, 2005). From this information, rupture properties such as rupture area, direction, and speed can be estimated. This method was originally used with seismic arrays (Ishii et al., 2005, 2007; Krüger & Ohrnberger, 2005), though several studies have also applied the method to a larger (e.g., global) distribution of seismic stations (Walker et al., 2005). This global approach can significantly improve resolution but can also hinder the coherence of waveforms due to complexities in the source and structure of the Earth, leading to artifacts in the back-projection results. The current study uses a novel genetic algorithm selection scheme to determine the seismic stations that should be used to reduce artifacts that arise from using a large distribution of seismic stations (Text AS2 in the supporting information). The key idea behind this algorithm is that waveforms from seismic stations should be chosen such that they image small earthquakes as point sources. This method is applied to seismic stations around the northern circum-Pacific including stations in the Transportable Array in Alaska and the High Sensitivity Seismographic Network (Hi-net) in Japan (Figure A2). Seismic stations in the Southern Hemisphere are excluded from the analysis due to their sparse distribution at teleseismic distances and the limited theoretical resolution improvement that they would provide (Figure AS7).

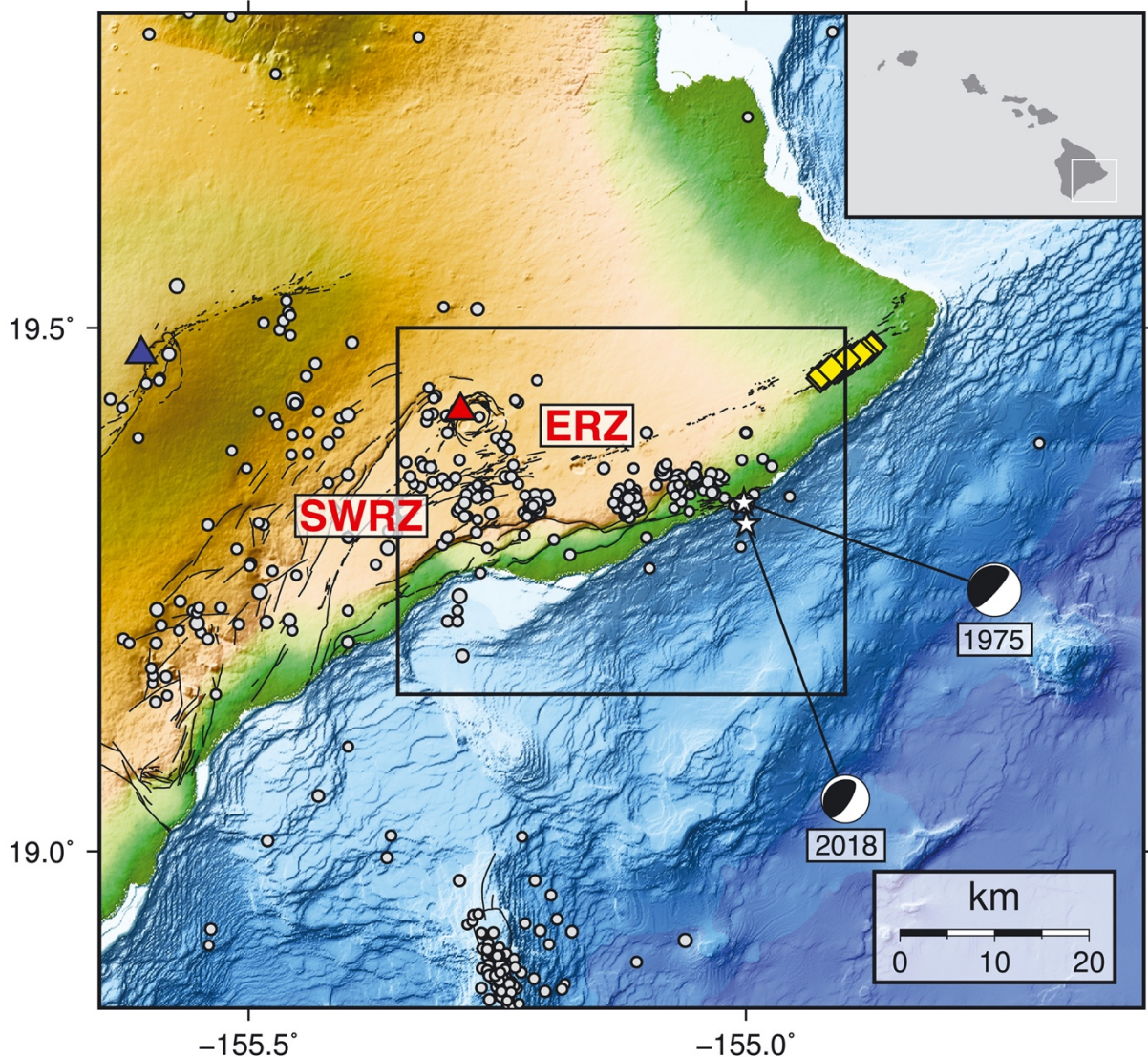


Figure A1. Geographic map of Hawai'i. The 2018 Mw 6.9 and 1975 Mw 7.7 National Earthquake Information Center epicenters are indicated by the 2018 and 1975 centroid-moment-tensor focal mechanisms, respectively. The red triangle is the location of the Kīlauea summit. The red ERZ and SWRZ labels show the locations of the East and Southwest Rift Zones, respectively. The blue triangle is the location of the Mauna Loa summit. The yellow diamonds are the locations of fissures. The black lines are faults. The magnitude-scaled gray dots show historical seismicity above magnitude 4.0 from 1955 to present (National

Earthquake Information Center). The black box outlines the study area in Figure A3. The inset shows the location of the map on the state of Hawaii.

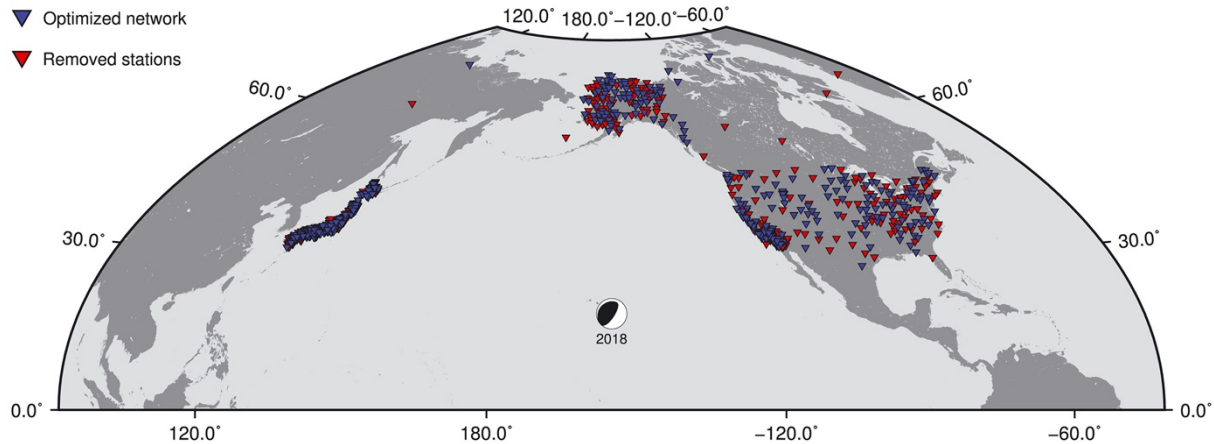


Figure A2. Distribution of stations. The inverted triangles are the locations of the 805 stations used in this study. The red inverted triangles are the 375 stations removed by the genetic algorithm and the blue inverted triangles are the 430 stations kept by the genetic algorithm (optimized network). The centroid-moment-tensor focal mechanism represents the 2018 Mw 6.9 mainshock. Figure AS5 shows detailed station distributions in Japan, Alaska, and the continental United States.

2. Methods

The back-projection method (Ishii et al., 2005) can be used with any network of seismic stations and any seismic phase, though P waves recorded at teleseismic distances are most often used because there is limited interference with other seismic phases for most earthquakes. The method is typically used with seismic arrays that have small station spacing and limited overall aperture. For these cases, the paths of waves from the source to the receivers are similar, which produces coherent recorded waveforms across the array. The coherence of the waveforms

enhances the stacking process and efficiently removes artifacts from the source image. Though the use of a single array typically produces robust results, the limited aperture also limits both spatial and temporal resolution. An increased distribution of seismic stations can be used to improve resolution, though care must be taken to avoid source image artifacts produced by incoherent data. This is typically done by either visual inspection of the data or using a measure of the similarity between portions of the waveforms (e.g., correlation value). Though selecting data based upon the characteristics of the waveforms can be useful, this approach does not directly address the source of artifacts in the back-projection results.

In this study, P waves from a broad distribution of northern circum-Pacific teleseismic stations are used to image the rupture properties of the 2018 Mw 6.9 Hawai‘i earthquake. These stations include the Transportable Array in Alaska, several networks in the contiguous United States, and Hi-net in Japan. The P waves from a small earthquake near the hypocenter of the mainshock are aligned using a cross-correlation procedure (Ishii et al., 2007). This step makes empirical travel time corrections to the data such that the arrival times of P waves are the same as those calculated using a one-dimensional Earth model, iasp91 (Kennett & Engdahl, 1991). This step also normalizes P wave amplitudes and corrects waveform polarities such that the initial waveforms have the same polarity. Several previous studies have developed methods for designing arrays that optimize resolution (e.g., Rost & Thomas, 2002) and reduce the effects of noisy data on array processing techniques (Goldstein & Archuleta, 1987; Meng et al., 2011; Schmidt, 1986). In this work, a genetic algorithm (e.g., Gallagher & Sambridge, 1994; Holland, 1992; Sambridge & Mosegaard, 2002) is used to determine a subset of the northern circum-Pacific stations that best image small earthquakes (magnitudes 4.6–5.4) in the mainshock area as point sources (Text AS2 and Figures AS3–AS6). This approach is designed to simultaneously

remove stations with misaligned or noisy data, select a distribution of stations that produces good theoretical array resolution, and select a distribution of stations that reduces the effects of unwanted seismic phases that can produce high-amplitude stacks at incorrect locations and times. Using this optimal array, mainshock waveforms are aligned separately and back projected using a coherence-based approach (Ishii, 2011) to determine the spatiotemporal source properties of the event. In order to estimate the relative source-time function of the mainshock, a separate linear stacking back-projection analysis is performed and the largest amplitude value for all grid points at each time step is plotted as a function of time.

3. Data

Seismic data was retrieved from the Incorporated Research Institutions for Seismology Consortium and the National Research Institute for Earth Science and Disaster Resilience in Japan. The alignment event used to determine empirical time corrections for the back-projection analysis occurred on 3 May 2018 and had a body wave magnitude of 5.1 (20:30:56 UTC, 19.344°N 155.070°W, 6.9-km depth; NEIC:

<https://earthquake.usgs.gov/earthquakes/eventpage/us1000dxhr/executive>). The hypocenter of this event is 8.4 km from the mainshock hypocenter. The point source events used for the genetic algorithm-based network optimization occurred on 4 May 2018 (21:32:44 UTC, 19.342°N 155.032°W, 6.9-km depth; NEIC:

<https://earthquake.usgs.gov/earthquakes/eventpage/us1000dy8n/executive>) and 5 May 2018 (03:30:15, 19.069°N 155.046°W, 8.7-km depth; NEIC:

<https://earthquake.usgs.gov/earthquakes/eventpage/hv70117676/executive>). The moment magnitude of the first event was 5.4, and the short-period body wave magnitude of the second

event was 4.6. The first event was 20.7 km from the mainshock hypocenter and the second event was 27.5 km from the mainshock hypocenter. Figure AS3 shows how the fitness value of the point source events increases as a function of generation number of the genetic algorithm, and Figure AS4 shows the source image improvement of the point source events from the full network to the optimal network. All data used are band-pass filtered to a frequency range of 0.8–2.0 Hz.

4. Results

The back-projection analysis images four distinct rupture directions associated with the 2018 Mw 6.9 earthquake (Figure A3a). The rupture initiates near the reported hypocenter and propagates north at ~1.5 km/s (Segment 1). At 4 s after the hypocentral time, the imaged rupture transitions to a northwest propagation direction with a speed of ~2.3 km/s (Segment 2). The next segment propagates south at an anomalously high rupture speed of ~4.3 km/s (Segment 3). The final imaged segment of the rupture occurs offshore and propagates west at ~0.7 km/s (Segment 4). The westward propagation associated with Segment 4 can be seen in the Incorporated Research Institutions for Seismology back-projection results (<https://doi.org/10.17611/DP/16504384>). The time evolution of energy release is determined by plotting the largest amplitude value for all grid points at each time step in the linear back-projection result (Figure A3b). The amplitude of high-frequency energy release is highest during Segment 4. The total duration of this earthquake is estimated to be 33 s. Following the west propagating rupture, there is an imaged episode of high-frequency energy release slightly south of the Kīlauea summit, though the spatial separation between this feature and the mainshock rupture indicates that it is either an early aftershock or an artifact (Movie AS1). The rupture area

of the mainshock, as estimated by summing the area within the 0.925 contour of the normalized source image at each time step of the event, is approximately 200 km², and the rupture lengths of Segments 1–4 are approximately 4.4, 4.6, 9.6, and 9.5 km, respectively. The 0.925 contour is used because the estimated rupture area significantly increases at normalized amplitude contours lower than this value, likely due to the background noise in the back-projection result. The slow overall rupture speed and long duration of this event are consistent with previous studies of this earthquake (Bai et al., 2018; Liu et al., 2018).

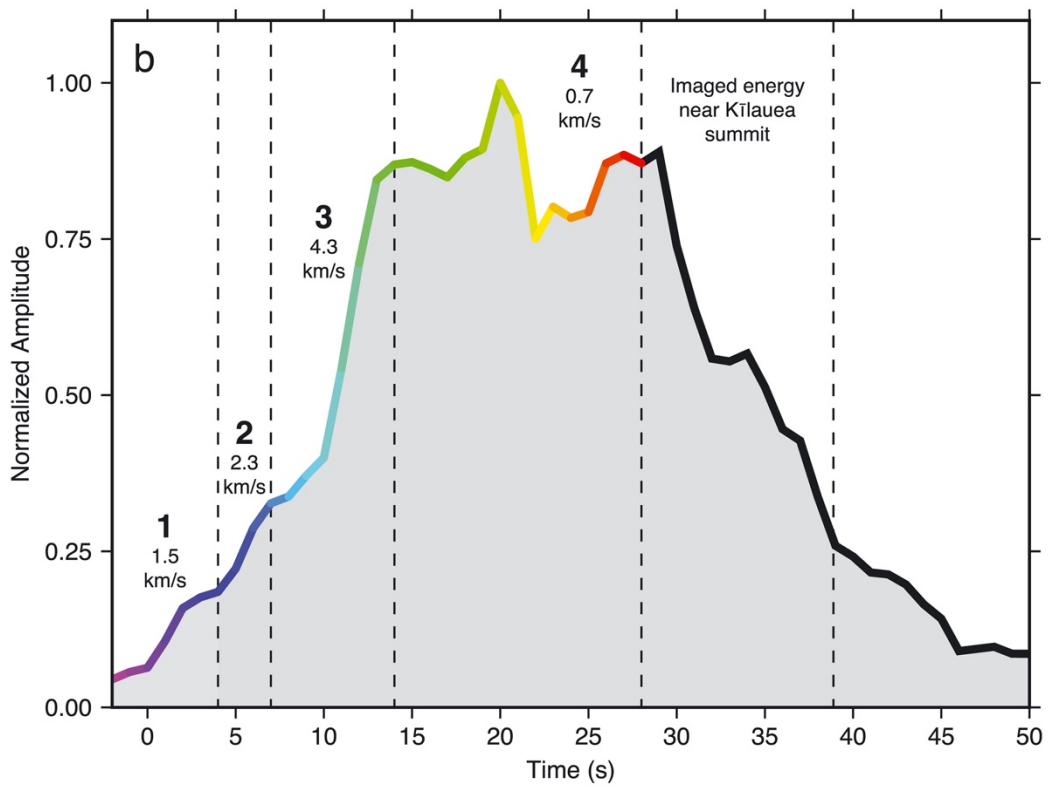
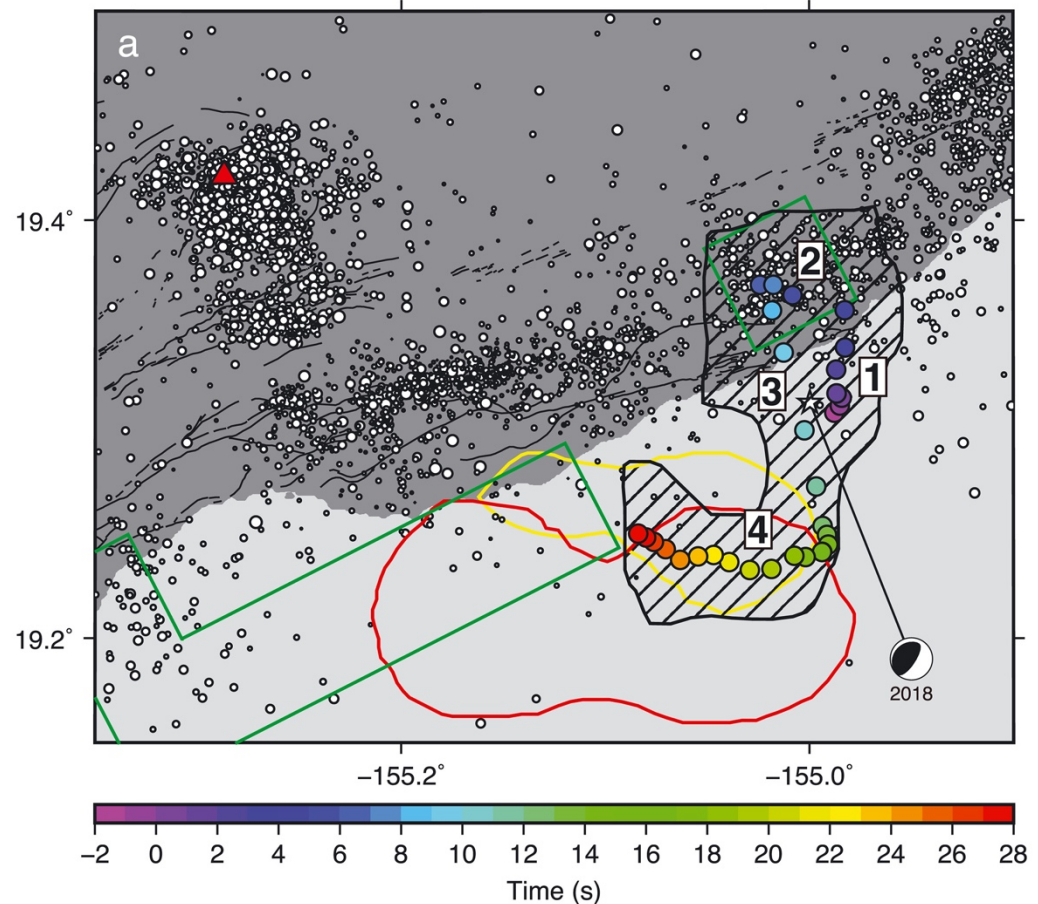


Figure A3. Summary of results. (a) The rainbow dots, determined from the coherence-based back-projection result, show the central source locations of the 2018 Mw 6.9 earthquake (Data Set AS1). The color of the dots indicates rupture time with respect to the hypocentral time (0 s). The individual segments of the overall rupture are labeled in white boxes. The white star is the National Earthquake Information Center epicenter, and black hatched area shows the estimated rupture area of the imaged earthquake. The red and yellow lines show the locations of periodic and aperiodic slow slip events, respectively (Foster et al., 2013). The green boxes show the distribution of largest slip (greater than 10 m) from the 1975 Mw 7.7 event (Owen & Bürgmann, 2006). The magnitude-scaled white dots show the post-mainshock seismicity located by Hawaiian Volcano Observatory (<https://doi.org/10.7914/SN/HV>). The black lines are faults. The dark and light gray background areas show onshore and offshore regions, respectively. (b) The normalized amplitude of high-frequency energy release as a function of time, determined from the linear back-projection result, is shown for the 2018 Mw 6.9 earthquake. The rainbow line of the source time function corresponds to the rainbow dots used in (a). The western rupture (Segment 4) shows the highest normalized amplitude.

5. Discussion and Conclusions

The back-projection analysis images significant complexity in both the directions and speeds of the individual segments that compose this rupture. Though the rupture direction changes between Segments 1 and 2, these features represent continuous propagation at speeds that are typical given local seismic wave velocities in this region (Lin et al., 2014; Syracuse et al., 2010). Assuming these segments involve slip on the décollement, they occur on a section of this fault where background seismicity is common (Figure A3a). In contrast to this typical

rupture behavior, a particularly anomalous feature is the high speed of Segment 3 that connects the onshore and offshore components of the rupture (Segments 2 and 4). The high rupture speed calculated for Segment 3 likely indicates a noncontinuous rupture that can be explained in one of the two following ways. First, synthetic results indicate that this feature may represent a spatial jump in the location of slip along the décollement between Segments 2 and 4 (Figure AS1). The spatiotemporal gap between these segments would suggest either static or dynamic stress triggering as the cause of this jump. The second possibility is that Segment 1 includes a southern rupture with amplitudes too low to be imaged in the back-projection results (Figure AS2). In this scenario, the hypothetical southern rupture connects the beginning of Segment 1 with Segment 4 without any spatial gaps in the overall rupture.

The fourth segment of the rupture is the dominant feature of this earthquake in terms of both the amplitude of energy release and the propagation length (Figure A3). This segment occurs 5–10 km offshore where both background seismicity and aftershocks are sparse (Figure A3a). In addition, this region of the décollement experiences slow slip events (Brooks et al., 2006; Foster et al., 2013; Montgomery-Brown et al., 2009, 2013; Poland et al., 2010; Segall et al., 2006; Syracuse et al., 2010). Modeling results have shown that the failure of velocity-weakening patches with dimensions close to the critical nucleation dimension can produce these slow slip events (Kato, 2004). Small velocity-weakening patches are also thought to produce high-frequency radiation during large earthquakes (e.g., Lay et al., 2012). Given that seismic slip rates initiated on an adjacent section of the décollement during the 2018 Mw 6.9 mainshock, the overlap between the area of slow slip events and the segment of rupture that produced the highest-amplitude high-frequency seismic waves (Segment 4) indicates that this section of the décollement may be composed of small velocity-weakening patches embedded within a larger

region of stable sliding. The location of Segment 4 would also suggest that stress accumulation on the décollement is not completely relieved by the slow slip events. The path of Segment 4 is near the boundary between patches of periodic and aperiodic slow slip behavior (Foster et al., 2013). If this boundary region represents a zone of reduced slow slip between the northern and southern slow slip patches (Figure A3a), then one would expect a high rate of stress accumulation in the absence of stable sliding, possibly explaining the propagation of this rupture into this region.

Several studies have concluded that the 1975 Mw 7.7 event had an anomalously long duration and ruptured west/southwest from its epicenter, which is ~4 km from the 2018 Mw 6.9 epicenter (Harvey & Wyss, 1986; Ma et al., 1999; Owen & Bürgmann, 2006). The detailed rupture properties of the 1975 event have been debated due to data limitations at the time, though recent studies of this event have argued that significant slip occurred offshore (Ma et al., 1999; Nettles & Ekström, 2004; Owen & Bürgmann, 2006). The 1975 and 2018 ruptures exhibit little overlap but fill the majority of the total décollement area (Figure A3a). There are also several similarities between the dynamic properties of these events. Both events had long durations given their magnitudes and low estimated rupture velocities (Harvey & Wyss, 1986), though this latter point only applies to Segment 4 for the 2018 mainshock. Both events also seem to have initiated near the coast where seismicity is abundant and then propagated offshore. In both cases, this offshore rupture is not associated with a spatially correlated aftershock sequence. These characteristics of the 1975 and 2018 earthquakes are similar to those observed for large events at near-trench locations of subduction zones. In the subduction zone setting, this seismic behavior is explained by soft sediments that compose the subduction interface in near-trench environments (Kanamori & Kikuchi, 1993). The low seismic velocities and anelasticity of this material lead to

slow rupture speeds and an inefficient transfer of stress that limits aftershock sequences. A similar argument may be applicable to the sediments that form the décollement between the volcanic edifice of Kīlauea and the underlying oceanic crust. Near-trench subduction zone earthquakes differ in frequency content from the 1975 Kalapana and 2018 Hawai‘i events, which generated significant high-frequency seismic radiation (Harvey & Wyss, 1986). This high-frequency radiation may be caused by the failure of small velocity-weakening patches embedded within an area of stable sliding (i.e., the soft sediments of the décollement). Given that the heterogeneous frictional properties of this interface provide the potential for both strong ground shaking and the generation of tsunami waves during large earthquakes, an improved understanding of the regions of the décollement that may experience significant slip during future large-magnitude events is critical for evaluating hazards in this region.

Acknowledgments

The authors acknowledge the Incorporated Research Institutions for Seismology (IRIS) Consortium and the National Research Institute for Earth Science and Disaster Resilience (NIED) in Japan for making digital seismic data open and readily available. The authors also acknowledge the Hawaiian Volcano Observatory (HVO) for access to their earthquake catalog. The Generic Mapping Tools (GMT) were used to create figures presented in this manuscript. Constructive comments and suggestions from Miaki Ishii, Gavin Hayes, Weston Thelen, and one anonymous reviewer have helped improve the results presented in this manuscript. The back-projection results are available in the supporting information.

References

- Bai, Y., Ye, L., Yamazaki, Y., Lay, T., & Cheung, K. F. (2018). The 4 May 2018 Mw 6.9 Hawaii Island earthquake and implications for tsunami hazards. *Geophysical Research Letters*, 45, 11,040–11,049. <https://doi.org/10.1029/2018GL079742>
- Brooks, B. A., Foster, J. H., Bevis, M., Frazer, L. N., Wolfe, C. J., & Behn, M. (2006). Periodic slow earthquakes on the flank of Kīlauea volcano, Hawai'i. *Earth and Planetary Science Letters*, 246, 207–216. <https://doi.org/10.1016/j.epsl.2006.03.035>
- Cayol, V., Dieterich, J. H., Okamura, A. T., & Miklius, A. (2000). High magma storage rates before the 1983 eruption of Kilauea, Hawaii. *Science*, 288(5475), 2343–2346. <https://doi.org/10.1126/science.288.5475.2343>
- Crosson, R. S., & Endo, E. T. (1982). Focal mechanisms and locations of earthquakes in the vicinity of the 1975 Kalapana earthquake aftershock zone 1970–1979: Implications for tectonics of the south flank of Kilauea Volcano, island of Hawaii. *Tectonics*, 1(6), 495–542. <https://doi.org/10.1029/TC001i006p00495>
- Denlinger, R. P., & Morgan, J. K. (2014). Instability of Hawaiian volcanoes. In *Characteristics of Hawaiian volcanoes* (Vol. 1801, Chap. 4, pp. 149–176). US Geological Survey Professional Paper. <https://doi.org/10.3133/pp1801>
- Denlinger, R. P., & Okubo, P. G. (1995). Structure of the mobile south flank of Kilauea Volcano, Hawaii. *Journal of Geophysical Research*, 100(B12), 24,499–24,507. <https://doi.org/10.1029/95JB01479>
- Dvorak, J. J., Okamura, A. T., English, T. T., Koyanagi, R. Y., Nakata, J. S., Sako, M. K., Tanigawa, W. T., & Yamashita, K. M. (1986). Mechanical response of the south flank of

- Kilauea Volcano, Hawaii, to intrusive events along the rift systems. *Tectonophysics*, 124(3–4), 193–209. [https://doi.org/10.1016/0040-1951\(86\)90200-3](https://doi.org/10.1016/0040-1951(86)90200-3)
- Ekström, G., Nettles, M., & Dziewoński, A. M. (2012). The global CMT project 2004–2010: Centroid-moment tensors for 13,017 earthquakes. *Physics of the Earth and Planetary Interiors*, 200–201, 1–9. <https://doi.org/10.1016/J.PEPI.2012.04.002>
- Foster, J. H., Lowry, A. R., & Brooks, B. A. (2013). Fault frictional parameters and material properties revealed by slow slip events at Kilauea volcano, Hawai‘i. *Geophysical Research Letters*, 40, 6059–6063. <https://doi.org/10.1002/2013GL058234>
- Gallagher, K., & Sambridge, M. (1994). Genetic algorithms: A powerful tool for large-scale nonlinear optimization problems. *Computers & Geosciences*, 20(7–8), 1229–1236. [https://doi.org/10.1016/0098-3004\(94\)90072-8](https://doi.org/10.1016/0098-3004(94)90072-8)
- Goldstein, P., & Archuleta, R. J. (1987). Array analysis of seismic signals. *Geophysical Research Letters*, 14(1), 13–16. <https://doi.org/10.1029/GL014i001p00013>
- Harvey, D., & Wyss, M. (1986). Comparison of a complex rupture model with the precursor asperities of the 1975 Hawaii Ms = 7.2 earthquake. *Pure and Applied Geophysics*, 124(4–5), 957–973. <https://doi.org/10.1007/BF00879621>
- Holland, J. H. (1992). Adaptation in natural and artificial systems: An introductory analysis with applications to biology, control, and artificial intelligence. MIT press. <https://doi.org/10.7551/mitpress/1090.001.0001>
- Ishii, M. (2011). High-frequency rupture properties of the Mw 9.0 off the Pacific coast of Tohoku earthquake. *Earth, Planets and Space*, 63, 609–614. <https://doi.org/10.5047/eps.2011.07.009>

Ishii, M., Shearer, P. M., Houston, H., & Vidale, J. E. (2005). Extent, duration and speed of the 2004 Sumatra-Andaman earthquake imaged by the Hi-Net array. *Nature*, 435, 933–936.
<https://doi.org/10.1038/nature03675>

Ishii, M., Shearer, P. M., Houston, H., & Vidale, J. E. (2007). Teleseismic P wave imaging of the 26 December 2004 Sumatra-Andaman and 28 March 2005 Sumatra earthquake ruptures using the Hi-net array. *Journal of Geophysical Research*, 112, B11307.
<https://doi.org/10.1029/2006JB004700>

Kanamori, H., & Kikuchi, M. (1993). The 1992 Nicaragua earthquake: A slow tsunami earthquake associated with subducted sediments. *Nature*, 361(6414), 714–716.
<https://doi.org/10.1038/361714a0>

Kato, N. (2004). Interaction of slip on asperities: Numerical simulation of seismic cycles on a two-dimensional planar fault with nonuniform frictional property. *Journal of Geophysical Research*, 109, 1–17. <https://doi.org/10.1029/2004JB003001>

Kennett, B. L. N., & Engdahl, E. R. (1991). traveltimes for global earthquake location and phase identification. *Geophysical Journal International*, 105(2), 429–465.
<https://doi.org/10.1111/j.1365-246X.1991.tb06724.x>

Krüger, F., & Ohrnberger, M. (2005). Tracking the rupture of the $M_w = 9.3$ Sumatra earthquake over 1,150 km at teleseismic distance. *Nature*, 435, 937–939.
<https://doi.org/10.1038/nature03696>

Lay, T., Kanamori, H., Ammon, C. J., Koper, K. D., Hutko, A. R., Ye, L., Yue, H., & Rushing, T. M. (2012). Depth-varying rupture properties of subduction zone megathrust faults. *Journal of Geophysical Research*, 117, B04311. <https://doi.org/10.1029/2011JB009133>

- Lin, G., Shearer, P. M., Matoza, R. S., Okubo, P. G., & Amelung, F. (2014). Three-dimensional seismic velocity structure of Mauna Loa and Kilauea volcanoes in Hawaii from local seismic tomography. *Journal of Geophysical Research: Solid Earth*, 119, 4377–4392.
<https://doi.org/10.1002/2013JB010820>.We
- Liu, C., Lay, T., & Xiong, X. (2018). Rupture in the 4 May 2018 Mw 6.9 earthquake seaward of the Kilauea East Rift Zone fissure eruption in Hawaii. *Geophysical Research Letters*, 45, 9508–9515. <https://doi.org/10.1029/2018GL079349>
- Ma, K.-F., Kanamori, H., & Satake, K. (1999). Mechanism of the 1975 Kalapana, Hawaii, earthquake inferred from tsunami data. *Journal of Geophysical Research*, 104(B6), 13,153–13,167. <https://doi.org/10.1029/1999JB900073>
- Meng, L., Inbal, A., & Ampuero, J.-P. (2011). A window into the complexity of the dynamic rupture of the 2011 Mw 9 Tohoku-Oki earthquake. *Geophysical Research Letters*, 38, L00G07. <https://doi.org/10.1029/2011GL048118>
- Montgomery-Brown, E. K., Segall, P., & Miklius, A. (2009). Kilauea slow slip events: Identification, source inversions, and relation to seismicity. *Journal of Geophysical Research*, 114, B00A03. <https://doi.org/10.1029/2008JB006074>
- Montgomery-Brown, E. K., Thurber, C. H., Wolfe, C. J., & Okubo, P. G. (2013). Slow slip and tremor search at Kilauea Volcano, Hawaii. *Geochemistry, Geophysics, Geosystems*, 14, 367–384. <https://doi.org/10.1002/ggge.20044>
- Neal, C. A., Brantley, S. R., Antolik, L., Babb, J. L., Burgess, M., Calles, K., Cappos, M., Chang, J. C., Conway, S., Desmither, L., Dotray, P., Elias, T., Fukunaga, P., Fuke, S., Johanson, I. A., Kamibayashi, K., Kauahikaua, J., Lee, R. L., Pekalib, S., Miklius, A., Million, W., Moniz, C. J., Nadeau, P. A., Okubo, P., Parcheta, C., Patrick, M. R., Shiro,

- B., Swanson, D. A., Tollett, W., Trusdell, F., Younger, E. F., Zoeller, M. H., Montgomery-Brown, E. K., Anderson, K. R., Poland, M. P., Ball, J. L., Bard, J., Coombs, M., Dietterich, H. R., Kern, C., Thelen, W. A., Cervelli, P. F., Orr, T., Houghton, B. F., Gansecki, C., Hazlett, R., Lundgren, P., Diefenbach, A. K., Lerner, A. H., Waite, G., Kelly, P., Clor, L., Werner, C., Mulliken, K., Fisher, G., & Damby, D. (2019). The 2018 rift eruption and summit collapse of Kīlauea Volcano. *Science* (New York, N.Y.), 363(6425), 367–374. <https://doi.org/10.1126/science.aav7046>
- Nettles, M., & Ekström, G. (2004). Long-period source characteristics of the 1975 Kalapana, Hawaii, earthquake. *Bulletin of the Seismological Society of America*, 94, 422–429. <https://doi.org/10.1785/0120030090>
- Owen, S. E., & Bürgmann, R. (2006). An increment of volcano collapse: Kinematics of the 1975 Kalapana, Hawaii, earthquake. *Journal of Volcanology and Geothermal Research*, 150, 163–185. <https://doi.org/10.1016/j.jvolgeores.2005.07.012>
- Owen, S. E., Segall, P., Lisowski, M., Miklius, A., Denlinger, R. P., & Sako, M. K. (2000). Rapid deformation of Kīlauea Volcano: Global Positioning System measurements between 1990 and 1996. *Journal of Geophysical Research*, 105(B8), 18,983–18,998. <https://doi.org/10.1029/2000JB900109>
- Poland, M. P., Miklius, A., Wilson, D., & Okubo, P. G. (2010). Slow slip event at Kīlauea Volcano. *Eos*, 34, 118–119. <https://doi.org/10.1029/2007GL031625>
- Rost, S., & Thomas, C. (2002). Array seismology: Methods and applications. *Reviews of Geophysics*, 40(3), 1008. <https://doi.org/10.1029/2000RG000100>
- Sambridge, M., & Mosegaard, K. (2002). Monte Carlo methods in geophysical inverse problems. *Reviews of Geophysics*, 40(3), 1009. <https://doi.org/10.1029/2000RG000089>

- Schmidt, R. (1986). Multiple emitter location and signal parameter estimation. *IEEE Transactions on Antennas and Propagation*, 34(3), 276–280.
<https://doi.org/10.1109/TAP.1986.1143830>
- Segall, P., Desmarais, E. K., Shelly, D., Miklius, A., & Cervelli, P. (2006). Earthquakes triggered by silent slip events on Kīlauea volcano, Hawaii. *Nature*, 442(7098), 71–74.
<https://doi.org/10.1038/nature04938>
- Swanson, D. A., Duffield, W. A., & Fiske, R. S. (1976). Displacement of the south flank of Kilauea volcano; The result of forceful intrusion of magma into the rift zones. Professional Paper. Retrieved from <http://pubs.er.usgs.gov/publication/pp963>
- Syracuse, E. M., Thurber, C. H., Wolfe, C. J., Okubo, P. G., Foster, J. H., & Brooks, B. A. (2010). High-resolution locations of triggered earthquakes and tomographic imaging of Kilauea Volcano's south flank. *Journal of Geophysical Research*, 115, B10310.
<https://doi.org/10.1029/2010JB007554>
- Walker, K. T., Ishii, M., & Shearer, P. M. (2005). Rupture details of the 28 March 2005 Sumatra Mw 8.6 earthquake imaged with teleseismic P waves. *Geophysical Research Letters*, 32, L24303. <https://doi.org/10.1029/2005GL024395>

Supporting Information

Introduction

The supporting information includes one supporting movie of the 2018 Mw 6.9 Hawai‘i earthquake rupture process (Movie AS1), one supporting dataset of the central source locations of the 2018 MW 6.9 earthquake (Dataset AS1), text describing the synthetic back-projection tests (Text AS1), text describing the genetic algorithm (Text AS2), four figures related to the synthetic back-projection tests (Figures AS1, AS2, AS6, and AS7), and three figures related to the genetic algorithm (Figures AS3, AS4, and AS5).

Data used to create Movie AS1 was collected from the Incorporated Research Institutions for Seismology (IRIS) and the National Research Institute for Earth Science and Disaster Resilience (NEID) in May 2018. The data was processed according to the steps described in the methods section of the main paper and the supporting text.

Text AS1

Synthetic sources are generated and back-projected with the optimized seismic network (Figure A2) to constrain the spatial and temporal resolution of the back-projection results. To determine if a spatial jump in the location of slip occurred between the end of Segment 2 and beginning Segment 4, synthetic seismograms consisting of 1 Hz central frequency Ricker wavelets are created at 27 source locations in one second increments (rainbow stars, Figure AS1). The synthetic source locations are identical to the locations of the main back-projection result, but omit Segment 3 (Figure A3). The recovered rupture of the synthetic back-projection result is similar to the rupture of the main back-projection result, suggesting that Segment 3 of the main back-projection result may be an artifact. The rupture speed of Segment 3 of the main

back-projection result is 4.3 km/s and the rupture speed of the recovered southern segment of the synthetic back-projection result is 5.3 km/s.

To determine if a bilateral rupture with an undetectable southern leg occurred between the beginning of Segment 1 and the beginning of Segment 4, synthetic seismograms consisting of 1 Hz central frequency Ricker wavelets are created at 40 source locations in one second increments (rainbow stars, Figure AS2). The synthetic source locations add a synthetic southern leg (9 points) to the source locations of the previous synthetic test (Figure AS1). A continuous rupture between the beginning of Segment 1 and the beginning of Segment 4 with a rupture speed of 0.4 km/s is assumed. The recovered rupture of the synthetic back-projection result using a small southern leg amplitude (9% of the amplitude of the northern and north-western segments) is similar to the rupture of the main back-projection result, suggesting that a bilateral rupture with a small southern leg amplitude may have occurred and been undetectable in the back-projection result. The rupture speed of Segment 3 of the main back-projection result is 4.3 km/s and the rupture speed of the recovered southern segment of the synthetic back-projection results is 4.1 km/s.

To analyze potential smearing from depth phases, two sets of synthetic seismograms consisting of 1 Hz central frequency Ricker wavelets are created from point sources at the reported NEIC mainshock hypocenter. The first synthetic data set includes only P-waves (Figure AS6a) and the second includes P-, pP-, and sP-waves (Figure AS6b). The back-projection results using P-wave travel times show little variation between the two sets of synthetic seismograms, suggesting that depth phases do not cause significant smearing in the results presented in the main text.

To analyze the potential effect of including southern hemisphere stations, synthetic seismograms consisting of 1 Hz central frequency Ricker wavelets are created from point sources at the reported NEIC mainshock hypocenter. Two synthetic tests are performed, the first using the optimal network obtained by the genetic algorithm, and the second using the same optimal network with every southern hemisphere station available from IRIS. After pre-processing steps on data from the alignment event that check for data quality, select stations with high correlation values, and find a common array between the mainshock and three aftershocks, 805 stations are available in the northern hemisphere and 71 stations are available in the southern hemisphere. The second synthetic test represents a best-case increase in station coverage where the genetic algorithm retains every additional southern hemisphere station. Even in this best-case scenario, the synthetic test results show that the addition of southern hemisphere stations does not significantly affect theoretical resolution (Figure AS7).

Text AS2

Here we outline the approach used for selecting an optimal seismic network for back-projection. The waveforms from a small earthquake (alignment event) are aligned using a cross-correlation procedure (Ishii et al., 2007). This step makes empirical travel time corrections to the data such that the arrival times of P-waves are the same as those calculated using a one-dimensional Earth model, iasp91 (Kennett & Engdahl, 1991). This step also normalizes P-wave amplitudes and corrects waveform polarities such that the initial waveforms have the same polarity. Using these empirical corrections, we find a group of stations that image other small earthquakes (point source events) in the region as point sources. A genetic algorithm is used to find this group of stations. Genetic algorithms find solutions to optimization problems and are

most effective for problems with large and complex fitness landscapes (Holland, 1992). Genetic algorithms have been applied to a variety of geophysical problems (e.g., Gallagher & Sambridge, 1994; Sambridge & Mosegaard, 2002), but the successful implementation of a genetic algorithm-based station selection scheme has not yet been demonstrated. The genetic algorithm starts with an initial population of 25 subsets of stations (individuals). Each individual is represented as a binary string of length M stations with a one indicating that a station is used and a zero indicating that a station is not used in the back-projection analysis. Twenty-one of these individuals have a randomly selected group of stations. One individual is the complete group of northern circum-Pacific stations. The three remaining individuals are selected based on their waveform correlation values with respect to a representative waveform for the complete group of stations. These correlation values come from waveforms of the alignment event and the three individuals are composed of the stations in the top, middle, and bottom halves of the correlation value distribution. Back-projection analyses are applied to each point source event using this initial population of individuals (i.e., 25 back-projection results for each point source event). Each of these back-projection analyses produce a stack at each grid point in the source area. These stacks are squared and integrated within a moving time window. The maximum value produced from these time windows is assigned to the respective grid point. A fitness value is calculated from these grid values based upon the following fitness function (ϕ):

$$\phi = (1 - \lambda) \frac{N_{low}}{N_{tot} - 1} + \lambda \frac{1}{N_{high}}$$

Here, N_{low} is the number of grid points with values below 20% of the maximum value of all grid points, N_{high} is the number of grid points with values above 80% of the maximum value of all grid points, N_{tot} is the total number of grid points, and λ is the weighting parameter (a value of $\frac{1}{2}$ is used to equally weight the contribution of N_{low} and N_{high}). The fitness function has a

value of one when the back-projection result is a perfect point source and approaches a value of zero as the imaged source broadens. The fitness function describes the fitness of an individual, which is used to determine the probability that the individual will be used in the crossover step via roulette wheel selection, also known as fitness proportionate selection (Holland, 1992). Once two individuals have been selected, a random point is chosen on their binary strings and the leading section of individual one is combined with the trailing section of individual two to produce a new individual. After creating a new individual, there is a small probability (1%) that each bit within the binary string will be flipped. This process mimics mutation and allows a broader search of the solution space. Twenty-four of the individuals within the population of the next generation are created using this approach. The 25th individual (elite individual) has the highest fitness value from the previous generation and is passed along to the next generation without modification. The same elite individual is only allowed to exist for five generations, at which point it is replaced with a random binary string. The optimal network that is obtained after 150 generations of the genetic algorithm is used to image the 2018 M_w 6.9 mainshock. Convergence towards an optimal solution may be constrained by plotting the fitness as a function of generation (Figure AS3). The fitness stabilizes around generation 100, indicating that a near-optimal solution is reached. Optimal solution convergence may also be constrained through the source image improvement of the point source events (Figure AS4). The back-projection results of the point source events with the full and optimized seismic networks show a distinct visual improvement. For clarity and completeness, the full and optimized networks for Japan, Alaska, and the continental United States are plotted individually (Figure AS5).

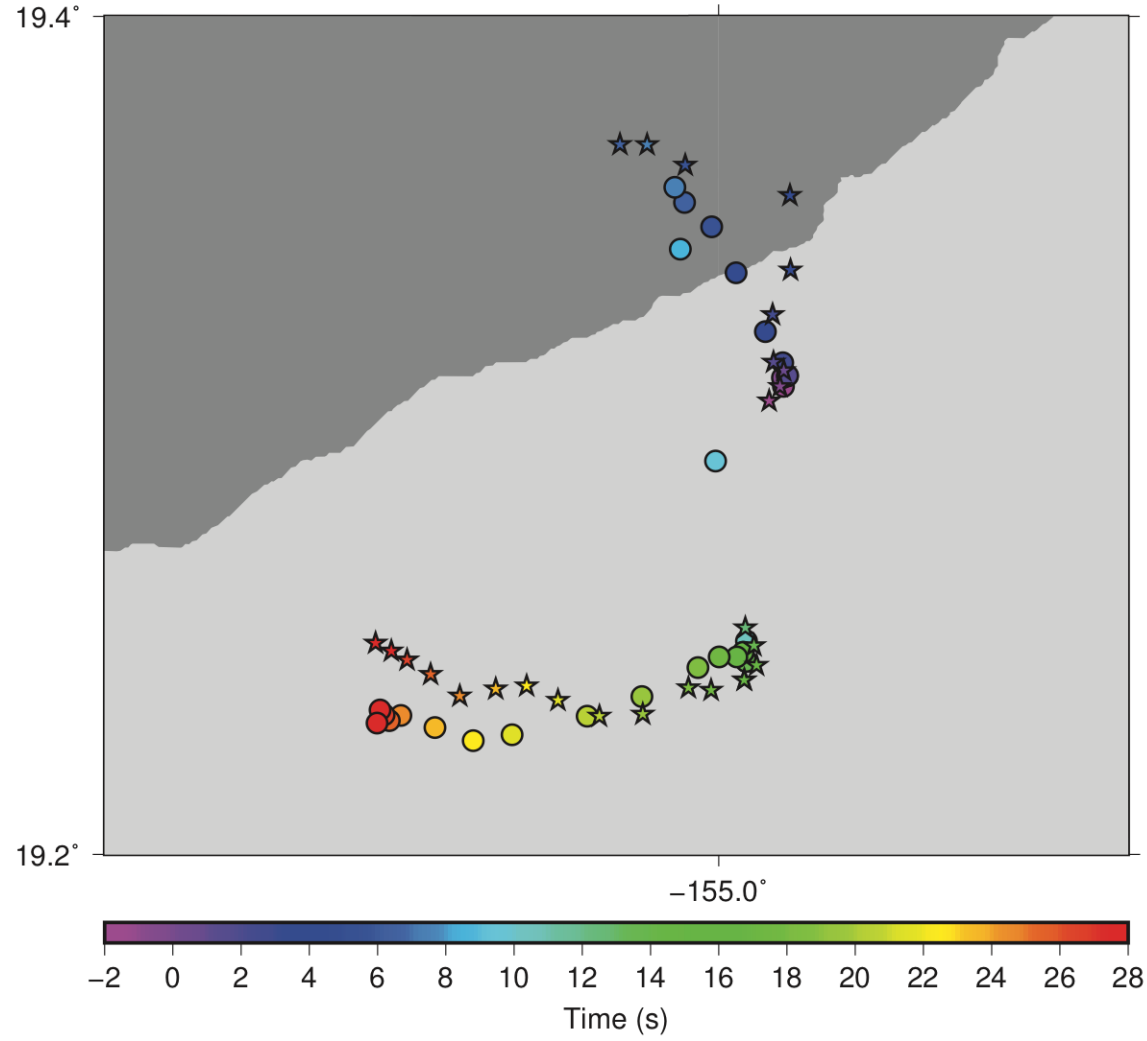


Figure AS1. Synthetic test of a spatial jump in the location of slip. The rainbow stars are the synthetic source locations and the rainbow circles show the recovered rupture of the synthetic back-projection result. Segment 3 of the main back-projection result is omitted in the synthetic source locations to simulate a jump between the end of Segment 2 and the beginning of Segment 4.

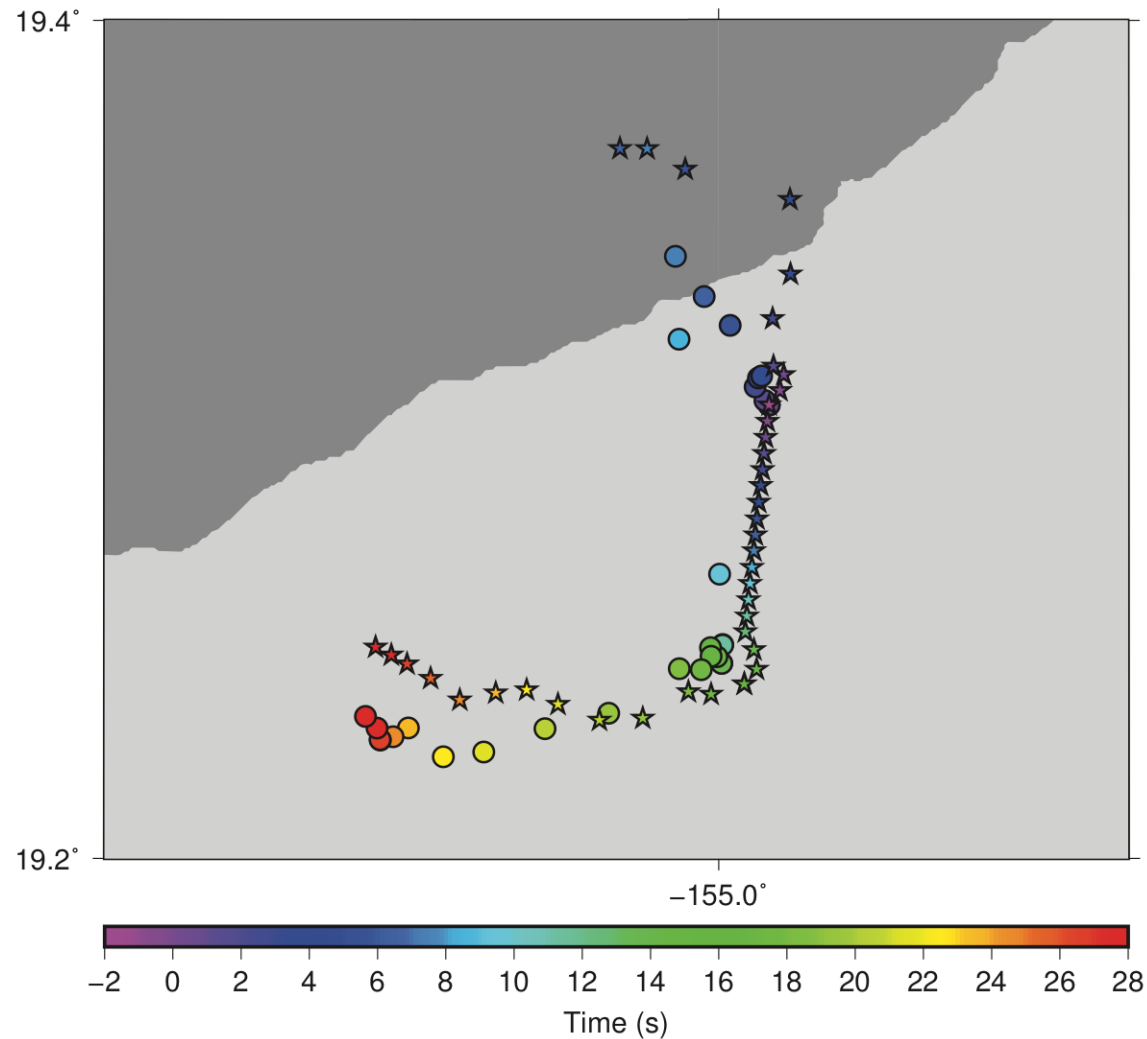


Figure AS2. Synthetic test of a bilateral rupture. The rainbow stars are the synthetic source locations and the rainbow circles show the recovered rupture of the synthetic back-projection result. The southern leg of the synthetic bilateral rupture is added to the synthetic source locations of Figure AS1 to simulate a bilateral rupture. The amplitude of the synthetic southern leg is 9% of the amplitude of the northern and north-western segments.

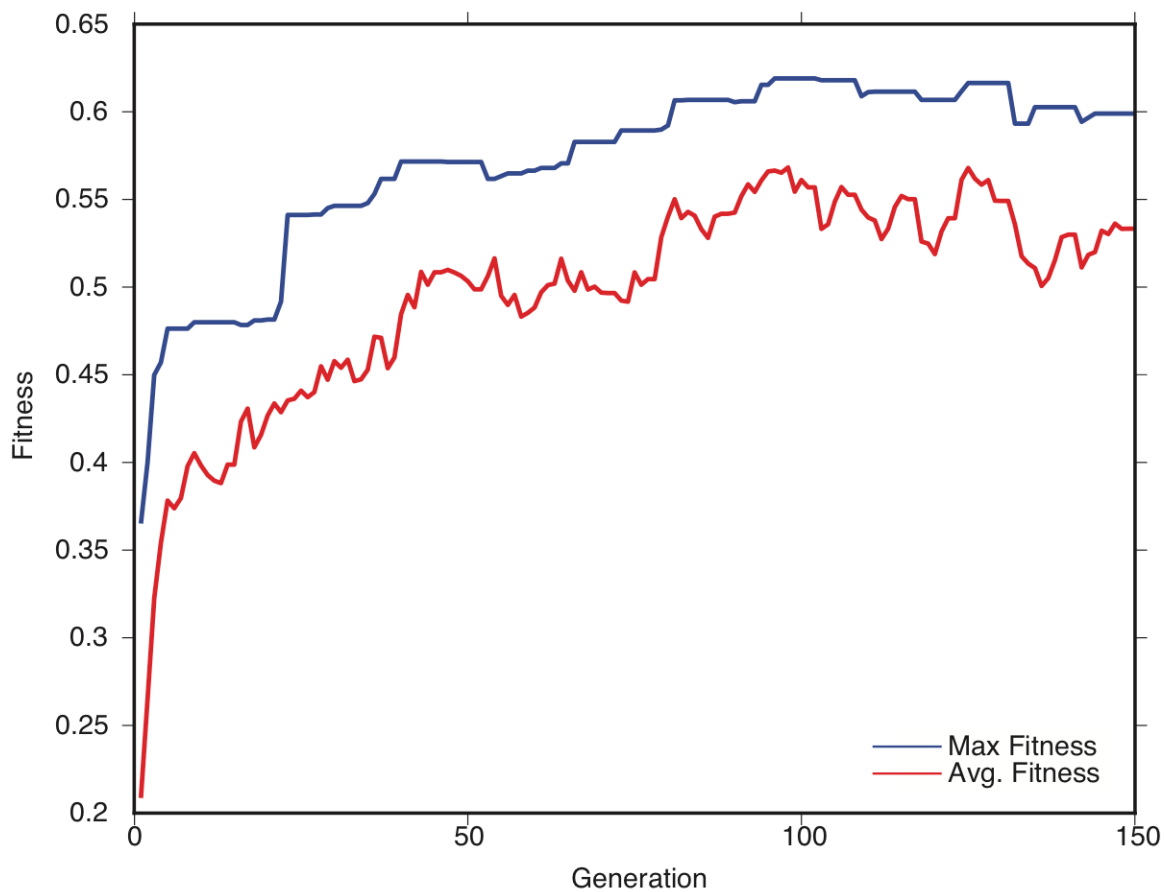


Figure AS3. Genetic algorithm population evolution. The maximum fitness of the population (elite individual) as a function of generation is shown in blue and the average fitness of all individuals as a function of generation is shown in red.

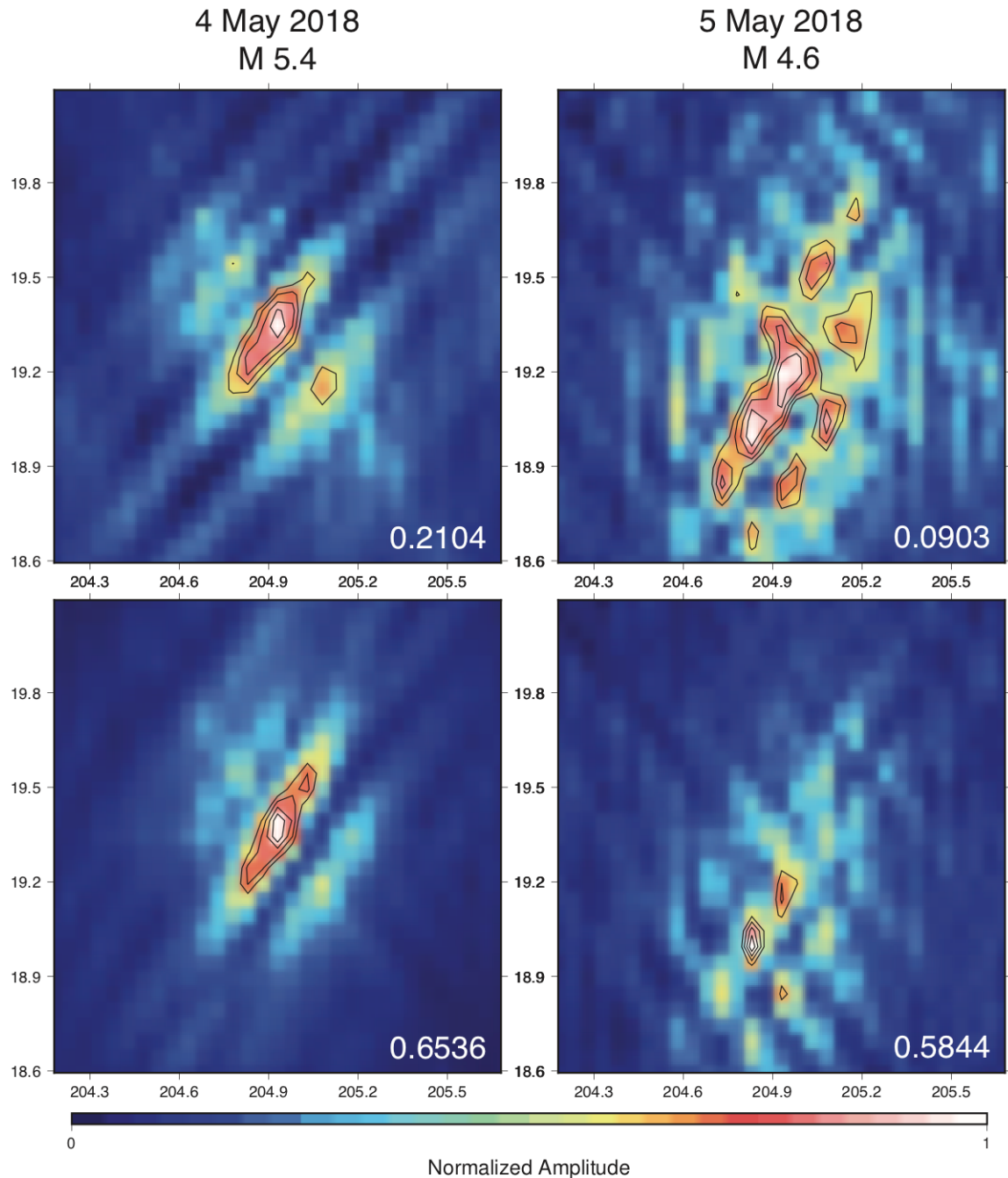


Figure AS4. Genetic algorithm source image improvement. The first row shows the back-projection results of the full seismic network and the second row shows the back-projection results of the optimized seismic network. The fitness (see Text AS2) of each result is displayed in the bottom right corner of each panel.

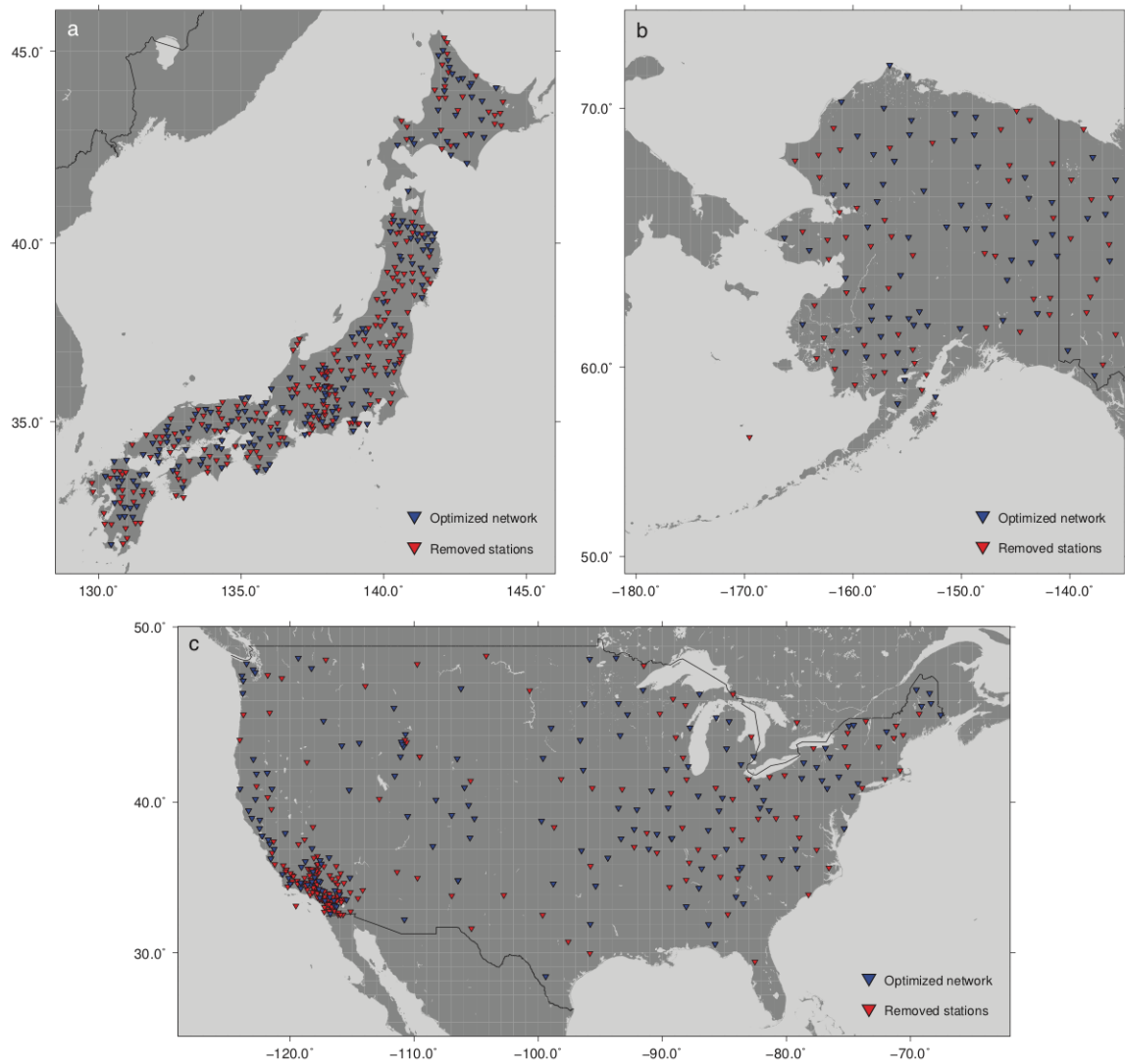


Figure AS5. Detailed distribution of stations in (a) Japan, (b) Alaska, and (c) the continental United States. The red inverted triangles are the stations removed by the genetic algorithm and the blue inverted triangles are the stations kept by the genetic algorithm (optimized network).

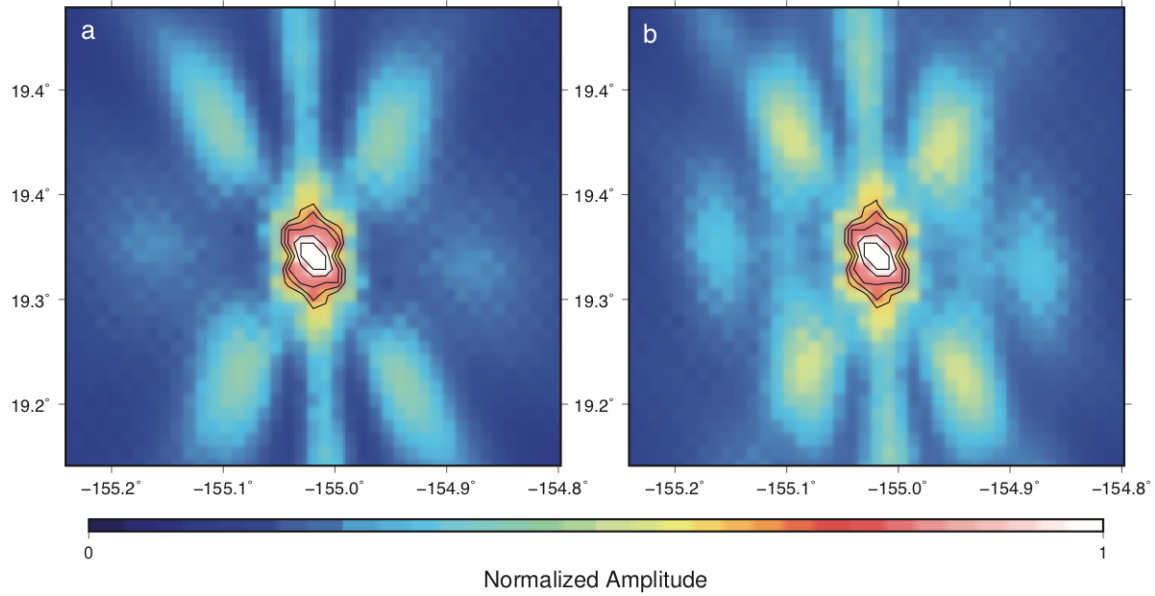


Figure AS6. Synthetic point source tests. (a) The coherence-based back-projection result for synthetically generated P-waves with the optimized network is shown. The approximate dimensions of the 0.925 amplitude contour are 1.9×2.5 km. (b) The coherence-based back-projection result for synthetically generated P-, pP-, and sP-waves with the optimized network is shown. The similarity between (a) and (b) indicate that depth phases are not a significant source of smearing.

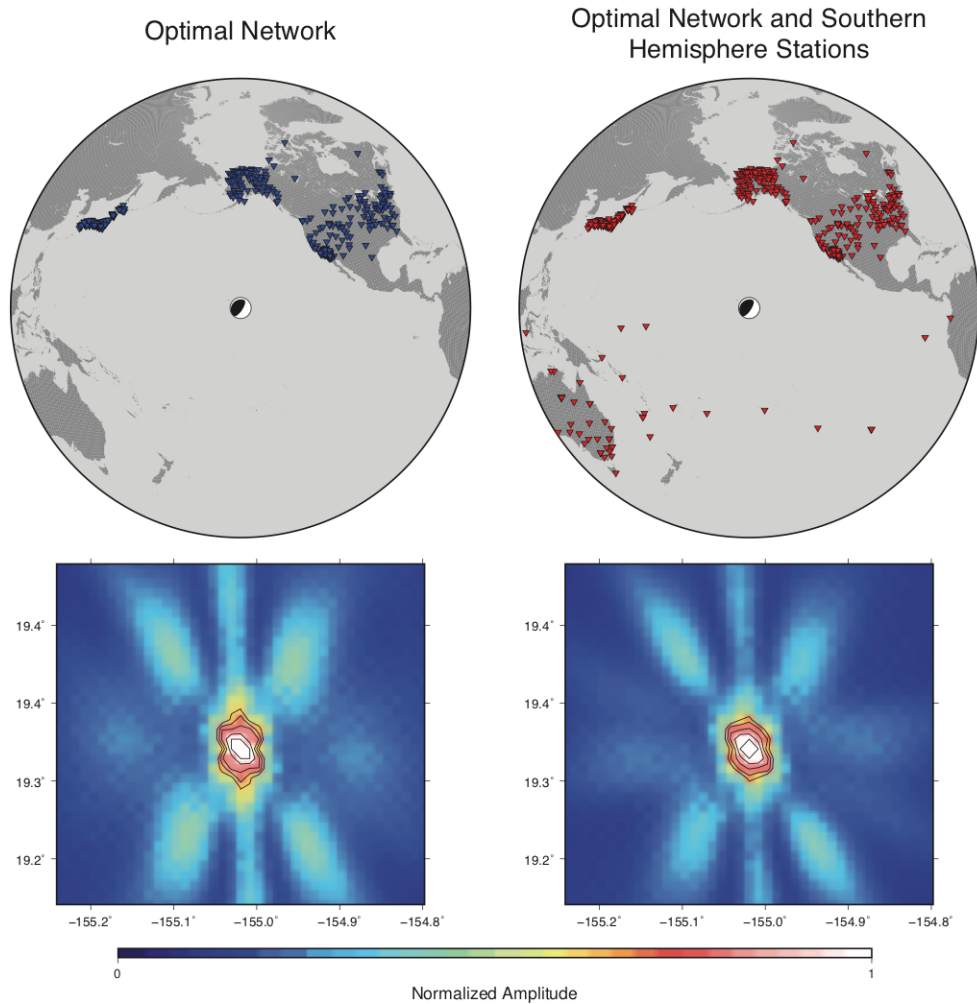


Figure AS7. Synthetic point source tests with and without southern hemisphere stations. The blue inverted triangles show the optimal network obtained by the genetic algorithm and the red inverted triangles show the optimal network with every teleseismic southern hemisphere station with usable data available from IRIS. The back-projection images below each network map show the coherence-based back-projection result for synthetically generated P-waves with each respective network.

The following supporting information (Movie AS1, Dataset AS1) are available for download at
<https://doi.org/10.1029/2018GL080397>.

Movie AS1. Normalized waveform coherence of the 2018 Mw 6.9 mainshock is plotted as a function of time (hypocentral time is 0 s). The white line is the coastline of Hawai‘i and the black lines are faults. The white dots indicate the maximum coherence value location for each 1 s time step.

Dataset AS1. Columns 1 and 2 represent the longitude and latitude of the central source locations of the 2018 MW 6.9 earthquake, respectively. Column 3 represents the rupture time with respect to the hypocentral time (0 s).

**APPENDIX B: EVIDENCE OF A SUPERSHEAR TRANSITION ACROSS A FAULT
STEPOVER**

H. L. Kehoe¹, E. D. Kiser¹

¹Department of Geosciences, University of Arizona, Tucson, AZ, USA

The text, figures, and supporting information included in this appendix were previously published as:

Kehoe, H. L. & E. D. Kiser (2020). Evidence of a Supershear Transition Across a Fault

Stepover. *Geophysical Research Letters*, 47, e2020GL087400.

<https://doi.org/10.1029/2020GL087400>

Abstract

Supershear earthquakes, propagating faster than the Earth's shear wave velocity, can generate strong ground motion at distances far from the ruptured fault. Despite the hazards associated with these earthquakes, the exact fault properties that govern their occurrence are not well constrained. Although early studies associated supershear ruptures with simple fault geometries, recent dynamic rupture models have revealed a supershear transition mechanism over complex fault geometries such as fault stepovers. Here we present the first observation of a supershear transition on a fault stepover system during the 2017 Mw 7.7 Komandorsky Islands earthquake. Using a high-resolution back-projection technique, we find that the earthquake's rupture velocity accelerates from 2.1 to 5.0 km/s between two offset faults, demonstrating the viability of a new supershear transition mechanism occurring in nature. Given the fault complexity of the Earth's transform plate boundaries, this result may improve our understanding of supershear rupture processes and their associated hazards.

Key Points

- A supershear transition across a fault stepover is observed in nature for the first time during the 2017 Komandorsky Islands earthquake
- These results have implications for the assessment of seismic hazard on fault stepover systems at all transform plate boundaries

Plain Language Summary

Earthquakes traveling faster than the shear wave velocity of the earth are occasionally observed in large strike-slip events. These so-called supershear earthquakes generate a

potentially destructive shock wave analogous to the sonic boom of a supersonic aircraft. Although many supershear earthquakes are coincident with straight, continuous fault sections, we find that the 2017 Komandorsky Islands earthquake reached supershear speeds following a jump in rupture across two fault segments. The results of this study confirm that supershear ruptures can occur on complex fault systems, allowing the seismic hazard on similar fault systems to be better evaluated.

1. Introduction

The tectonic environment surrounding the Kamchatka-Aleutian triple junction is complex, in large part due to the westward transition from normal subduction to trench-parallel shearing along the Aleutian Trench (Figure B1a). Upper plate deformation west of 172°E is controlled by back-arc strike-slip faulting resulting from the increase in slip partitioning as the relative motion between the Pacific and North American plates becomes more oblique (Avé Lallement, 1996; Newberry et al., 1986). Near the Komandorsky Islands (Figure B1c), back-arc strike-slip faults form the Bering Fracture Zone (BFZ), and the Komandorsky Sliver is bounded to the north and south by the BFZ and Aleutian Trench, respectively. The BFZ accommodates approximately two thirds (51 mm/yr) of the relative shearing motion between the Pacific and North American plates (78 mm/yr) and has a locking depth of 12 km, making the region a prime tectonic environment for large strike-slip events (Kogan et al., 2017).

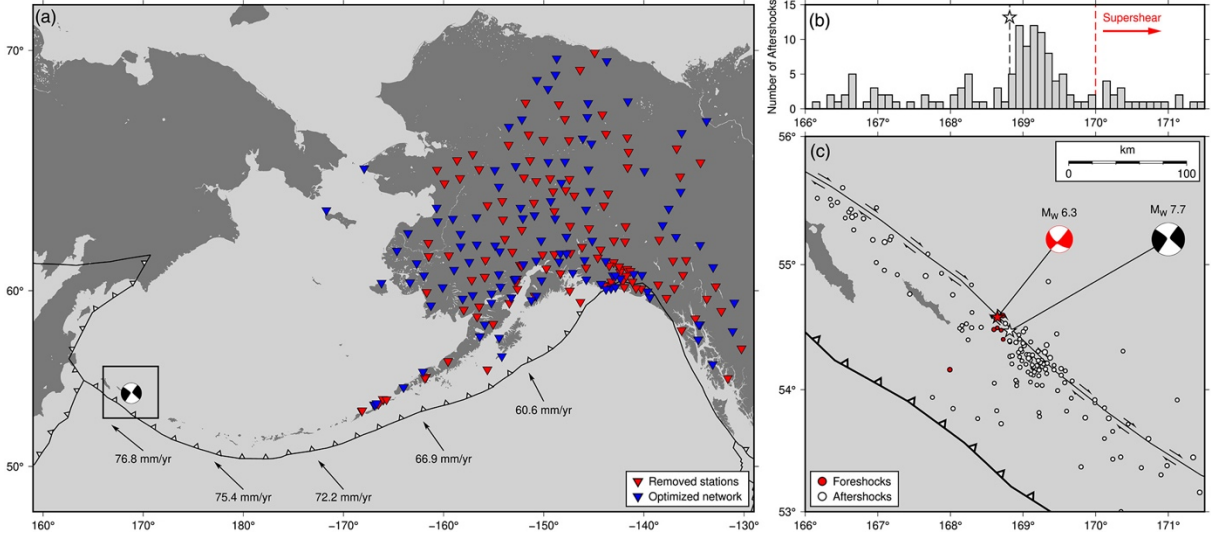


Figure B1. Geographic map of the study area and the back-projection station distribution. (a) Subduction zones are shown as a black line with white triangles on the overriding plate. Relative motion of the Pacific Plate with respect to the North American plate along the Aleutian Trench is shown with black arrows (DeMets et al., 2010). The centroid-moment tensor shows the epicenter of the 2017 MW 7.7 mainshock. The red inverted triangles show the 116 seismic stations removed by the genetic algorithm and the blue inverted triangles show the 107 stations kept by the genetic algorithm (optimized network). The black box outlines the location of the map area in (c). (b) The histogram shows the longitudinal distribution (bin widths of 0.1°) of 138 aftershocks above magnitude 4 for 3 weeks after the mainshock. The white star and black dashed line show the longitude of the mainshock epicenter with respect to the aftershock distribution. The red dashed line shows the beginning of the supershear rupture segment. (c) The Aleutian Trench is shown as a black line with white triangles on the overriding plate. The Bering Fracture Zone (BFZ) is shown as a black line with right-lateral strike-slip arrows. The area between the Aleutian Trench, and BFZ is the Komandorsky Sliver. The two dark gray islands are the Komandorsky Islands. The red and white stars show the

MW 6.3 foreshock and MW 7.7 mainshock epicenters, respectively. The centroid-moment tensor of each earthquake is shown by their respective colors. The magnitude-scaled red and white dots are earthquakes above magnitude 4 for the day before (foreshocks) and 3 weeks after (aftershocks) the mainshock, respectively.

On 17 July 2017, a Mw 7.7 earthquake occurred 335 km east-southeast of the Kamchatka-Aleutian triple junction, near the Komandorsky Islands (Figure B1c). The National Earthquake Information Center (NEIC) hypocenter and the Global Centroid-Moment Tensor (GCMT) solution (Dziewonski et al., 1981; Ekström et al., 2012) indicate that this earthquake occurred on the BFZ. This is the largest event recorded on this portion of the BFZ by modern instruments. Approximately 12 hours before the mainshock, a large Mw 6.3 foreshock occurred 20.4 km northwest of the mainshock epicenter, also on the BFZ (Figure B1c). A sequence of seven additional smaller events occurred near the BFZ between the foreshock and the mainshock, and a significant cluster of aftershocks occurred immediately southeast of the mainshock (Figures B1b and B1c). The BFZ is expected to be structurally complex, especially southeast of the mainshock epicenter. Geodetic measurements indicate a probable migration of strike-slip faults from the back-arc to the fore-arc (Cross & Freymueller, 2008; Kogan et al., 2017), and the distribution of focal mechanisms reveals an abrupt change in the stress field near 170°E (Lutikov et al., 2019).

In this study, we image the rupture process of the 2017 Komandorsky Islands earthquake using a network of seismic stations in Alaska and the back-projection method, which stacks time-shifted waveforms on a grid of potential source locations to determine the spatiotemporal evolution of energy release during an earthquake (Ishii et al., 2005). We show that the

earthquake rupture accelerated to supershear velocities across a fault stepover system with a transition mechanism that has previously only been observed in numerical models (Hu et al., 2016; Ryan & Oglesby, 2014).

2. Data and Methods

The back-projection method, benefiting from the emergence of dense seismic networks, has been used by several studies to image the rupture processes of earthquakes (e.g., Kiser & Ishii, 2017). The method does not require a priori information such as fault geometry and rupture velocity and is able to resolve complex features such as earthquake frequency dependence and rupture segmentation (e.g., Kiser & Ishii, 2011; Koper et al., 2011; Meng et al., 2011; Wang & Mori, 2011). Although any seismic phase and distribution of stations may be used, back-projection studies are typically limited to P waves recorded at teleseismic (30° – 90°) distance windows to minimize interference with other seismic phases. Back-projection studies at regional ($< 30^\circ$) distance windows may capture greater rupture complexity than those at teleseismic distance windows due to the increased relative aperture of the seismic network. However, these results are susceptible to artifacts caused by triplications from the mantle transition zone and other unwanted seismic phases (e.g., depth phases). Here we apply a genetic algorithm-based station selection method (Kehoe et al., 2019) to three networks of stations in Alaska within a distance of 35° (USArray Transportable Array: <https://doi.org/10.7914/SN/TA>; Alaska Regional Network: <https://doi.org/10.7914/SN/AK>; Alaska Volcano Observatory: <https://doi.org/10.7914/SN/AV>). This process removes stations producing artifacts in the source image, forming an optimized back-projection network (Figure B1a) and revealing the previously unobserved rupture complexity of the 2017 Komandorsky Islands earthquake.

Seismic data used in the back-projection analysis are obtained from the Incorporated Research Institutions for Seismology (IRIS) Consortium and are band-pass filtered to two frequency bands, 0.5 to 1 Hz (low-frequency) and 0.8 to 2 Hz (high-frequency). For all data, a cross-correlation procedure (Ishii et al., 2007) is used to align waveforms from a small event near the mainshock hypocenter. The alignment event used in this study had a similar GCMT solution to the mainshock, occurred 32.8 km from the mainshock hypocenter on 28 July 2017, and had a moment magnitude of 5.5 (02:39:15 UTC, 54.303°N 169.301°E; NEIC: <https://earthquake.usgs.gov/earthquakes/eventpage/us2000a21g/executive>). This process accounts for three-dimensional heterogeneity at grid points near the source by making empirical travel time corrections to P wave arrival times such that they agree with the arrival times calculated using a one-dimensional Earth model, iasp91 (Kennett & Engdahl, 1991). This cross-correlation procedure provides further adjustments such that P wave amplitudes are normalized, and waveform polarities are corrected with respect to a reference stack of waveforms.

Following the travel time corrections, a genetic algorithm-based station selection method (Text BS1) is used to remove stations that produce artifacts in the back-projection image. For this step, a second small event near the mainshock hypocenter is used to find a distribution of stations that image the event as a point source. The point source event used in this study had a similar GCMT solution to the mainshock, occurred 19.2 km from the mainshock hypocenter on 17 July 2017, and had a body wave magnitude of 5.1 (11:23:01 UTC, 54.596°N 168.721°E; NEIC: <https://earthquake.usgs.gov/earthquakes/eventpage/us20009wwq/executive>). This approach is established on the principle that small events should be imaged by the back-projection method as point sources, and any additional imaged energy is likely the result of artifacts in the back-projection result. Given a seismic network of M stations, an optimal subset

of stations that image a small event as a point source can be found in 2M attempts. A genetic algorithm (Holland, 1992), typically used to find solutions to optimization problems with large and complex fitness landscapes, is used to significantly reduce this number of attempts and find a near-optimal solution.

Once the optimized network is determined, the performance of the genetic algorithm-based station selection method is quantified. Figure BS1 shows how the fitness value of the point source event increases as a function of iteration, and Figure BS2 shows the source image improvement of the point source event between the full and optimized seismic networks. The final back-projection result is obtained by first aligning the mainshock waveforms recorded at the optimized network independently of the previous alignment event before using a coherence-based back-projection approach (Ishii, 2011) to image the mainshock rupture. This alignment procedure robustly corrects for three-dimensional heterogeneity along the length of the southeastern rupture (Figure BS6). The mainshock waveforms recorded at the complete distribution of stations are also aligned independently and back-projected using the same coherence-based approach to determine the improvement in spatiotemporal resolution between the optimized and full networks (Figure BS3).

3. Regional Back-Projection Result

Back-projection results using high-frequency (0.8 to 2 Hz) data recorded at the optimized network reveal a complex southeastern rupture containing three distinct segments while results using low-frequency (0.5 to 1 Hz) data image a simple northwestern rupture (Figure B2a, Movies BS1 and BS2, Data Sets BS1 and BS2). Portions of the southeastern rupture are also imaged using low-frequency data (Figure BS3, Movie BS3, Data Set BS3). The complete distribution of

regional stations resolves some portions of the southeastern rupture at low and high frequencies but does not resolve the northwestern rupture, which is dominated by an eastward moving artifact (Figure BS3, Movies BS4–BS6, Data Sets BS4–BS6). Consequently, we use the optimized network (Figure B1a) and present the high-frequency southeastern rupture and low-frequency northwestern rupture as our main back-projection result (Figure B2a).

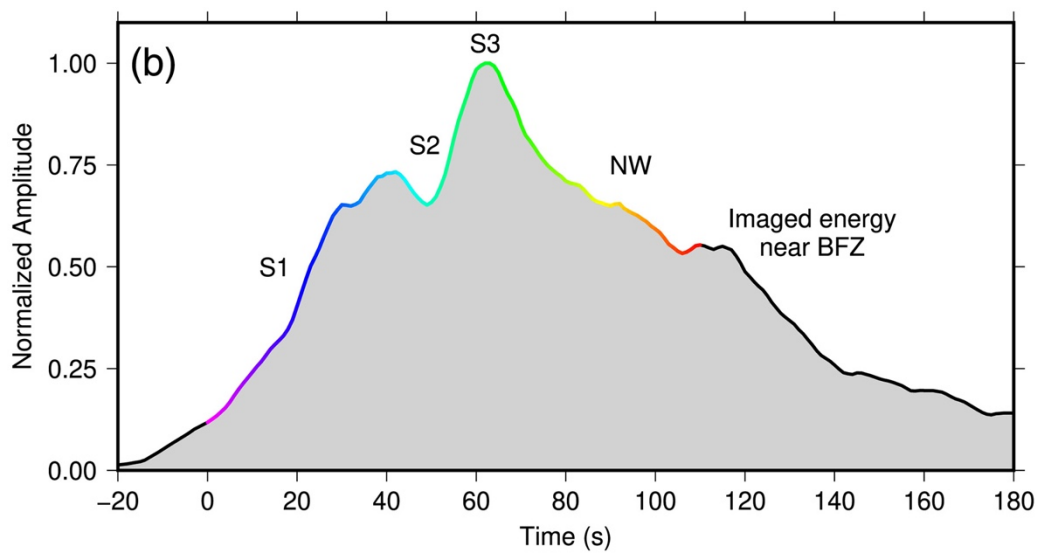
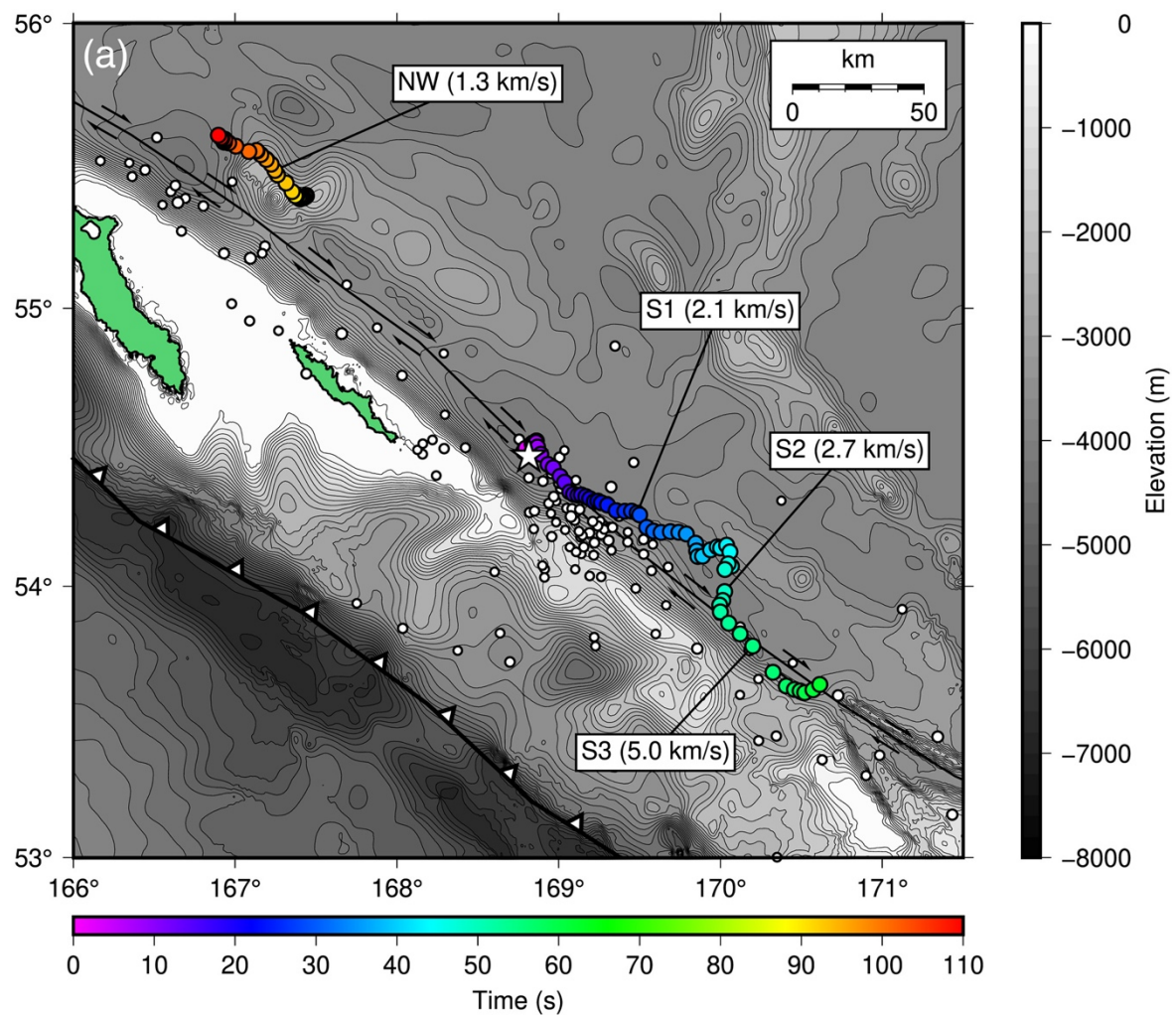


Figure B2. Summary of the 2017 Komandorsky Islands mainshock back-projection results. (a)

The white star shows the epicenter of the 2017 Komandorsky Islands earthquake. The rainbow dots are determined from the coherence-based back-projection result using the optimized network and show the central source locations of the mainshock rupture. The color of the dots indicate the time with respect to origin time (0 s). The labels S1, S2, and S3 show the locations of the first, second, and third segments of the southeastern rupture, respectively. The label NW shows the location of the imaged northwestern rupture. Bathymetry contours are plotted every 200 m. The Aleutian Trench is shown as a black line with white triangles on the overriding plate. The Bering Fracture Zone (BFZ) is shown as a black line with right-lateral strike-slip arrows. The area between the Aleutian Trench and BFZ is the Komandorsky Sliver. The two green islands are the Komandorsky Islands. The magnitude scaled white dots are aftershocks above magnitude 4 for 3 weeks after the mainshock. (b) The normalized amplitude of energy release as a function of time is determined from the linear back-projection result and shown for the 2017 Komandorsky Islands earthquake. The rainbow line of the source time function and the labels correspond to the rainbow dots and labels used in (a).

The locations of energy release northwest and southeast of the reported epicenter suggest that this earthquake ruptured bilaterally. The high-frequency southeastern rupture begins with Segment 1, which originates near the reported epicenter and propagates 94.3 km southeast for 45 s at 2.1 km/s. During Segment 2, the rupture appears to turn due south and travel 18.8 km for 7 s at 2.7 km/s. As the rupture resumes propagation towards the southeast during Segment 3, the rupture speed quickly accelerates to 5.0 km/s, traversing 50.2 km in just 10 s. The rupture speed of Segment 3 exceeds the shear wave velocity of the crust, estimated by Crust1.0 to be 3.4–3.9

km/s in this region (Laske et al., 2013). The imaged low-frequency northwestern rupture begins 135.8 km northwest of the reported epicenter and propagates 41.6 km northwest for 31 s at 1.3 km/s. The dominant southeastern rupture obscures the first 79 s of the northwestern rupture, preventing this portion of the rupture from being imaged. Assuming a continuous northwestern rupture between the epicenter and the first location of imaged energy at 79 s, a rupture velocity of 1.7 km/s over 135.8 km is required. Previous models incorporating GPS observations require slip northwest of the epicenter, but back-projection results prior to this study have not robustly imaged the northwestern propagation of this earthquake (Lay et al., 2017; IRIS: <https://doi.org/10.17611/DP/13610282>). A teleseismic back-projection analysis using North American data band-pass filtered between 0.5 and 2 Hz resolves the general southeastern and northwestern ruptures (Figure BS4, Movies BS7 and BS8, Data Sets BS7 and BS8), although the regional back-projection results offer superior spatiotemporal resolution. The complexity of the southeastern rupture can be seen in all back-projection results (Figures BS3–BS4), which is further illustrated by evaluating the epicentral distance of each source location as a function of time for the regional back-projection results (Figure BS5).

The normalized energy release as a function of time is determined by applying a linear back-projection analysis to data band-passed filtered between 0.5 and 2 Hz (Figure B2b). The largest amplitude of energy release occurs during Segment 3 of the southeastern rupture. The total duration of this earthquake is estimated to be 110 s. Following the earthquake, there is an imaged episode of energy release southeast of Segment 3 on the BFZ, which may be an early aftershock (Movie BS1).

4. Independent Supershear Validation

Supershear rupture velocities have been observed using a variety of different methods, with studies exploiting strong ground motion records (Archuleta, 1984; Bouchon et al., 2000, 2001; Dunham & Archuleta, 2004), finite fault model inversions (Konca et al., 2010; Yue et al., 2013), and far-field surface wave observations (Bao et al., 2019; Vallée & Dunham, 2012). Although the back-projection method is capable of resolving supershear ruptures (Bao et al., 2019; Walker & Shearer, 2009; Wang et al., 2012), here we use far-field Rayleigh wave observations to validate the supershear rupture segment imaged in the regional back-projection result.

Rayleigh waves generated by the 2017 Mw 7.7 Komandorsky Islands mainshock and a smaller Mw 6.3 foreshock are compared in this section. The two events share similar focal mechanisms (Figure B1c) and are 20.4 km apart. Seismic theory (Dunham & Bhat, 2008; Vallée & Dunham, 2012) predicts that within a far-field Mach cone, surface wave seismograms generated along the length of a supershear rupture will be identical to those created by smaller events with the same focal mechanism, and the surface wave amplitude ratio of the two events will be equal to their moment ratio. The opening angles of the Mach cones with respect to the supershear rupture segment are a function of the surface wave phase velocity and the rupture velocity. Due to the frequency-dependent and globally heterogenous nature of surface wave phase velocities, values are estimated for each Mach cone using GDM52, a global surface wave phase velocity model (Ekström, 2011). The northeastern and southeastern Mach cone locations are calculated using estimated Rayleigh wave phase velocities of 3.3 ± 0.4 km/s and 4.1 ± 0.3 km/s, respectively. Using constraints from the back-projection result, both Mach cone calculations use an estimated rupture velocity of 5.0 ± 0.5 km/s, and the supershear rupture segment is approximated as a straight line that is 50.2 km long, striking 126.0° (Figure BS3a).

Broadband vertical component seismic data recorded within a distance window of 60° of the mainshock hypocenter are retrieved from the IRIS Consortium, the Northern California Earthquake Data Center (NCEDC: <https://www.doi.org/10.7932/NCEDC>), and the Southern California Earthquake Data Center (SCEDC: <https://doi.org/10.7909/C3WD3xH1>) and are band-pass filtered to periods of 15–25 s to minimize the effects of dispersion. Rayleigh wave first arrivals are manually picked in the mainshock data, and the Rayleigh wave train is manually cut from the foreshock data. The foreshock Rayleigh wave train is cross-correlated against the mainshock seismogram (beginning at the Rayleigh wave first arrival), and the maximum cross-correlation value at each station is used to compare waveform similarity inside and outside the Mach cones. There is a distinct pattern of high correlation values (> 0.8) within the Mach cones (Figure B3). The amplitude ratios of the recorded Rayleigh waves from the Mw 7.7 mainshock and the Mw 6.3 foreshock also agree with theoretical predictions. The amplitude ratio of recorded Rayleigh waves within the Mach cones is a factor of approximately 25–40. Had the supershear segment composed the entire mainshock rupture, the expected moment ratio between the Mw 7.7 mainshock and the Mw 6.3 foreshock would be a factor of approximately 126. Rayleigh waves from the subshear segment (Segment 1) of the mainshock rupture may interfere destructively with Rayleigh waves from the supershear segment (Segment 3) but have little effect on the overall waveforms recorded by stations within the Mach cones (Vallée & Dunham, 2012). We estimate the supershear segment released 20–30% of the total moment by assuming the rupture length is proportional to moment release. This reduces the expected moment ratio between the two events to the observed amplitude ratios within the Mach cones. The high cross-correlation values and the observed amplitude ratios within the Mach cones indicate that this segment of the mainshock ruptured at supershear speeds. Due to poor station coverage in the

Pacific Ocean, the northeastern Mach cone is a more reliable indicator of the supershear rupture than the southeastern Mach cone. The nonzero time shifts associated with the maximum cross-correlation values of data recorded within the Mach cones are due to the initial subshear segment (Segment 1) of the mainshock rupture, which delays the arrival of the Rayleigh waves generated by the supershear segment (Segment 3).

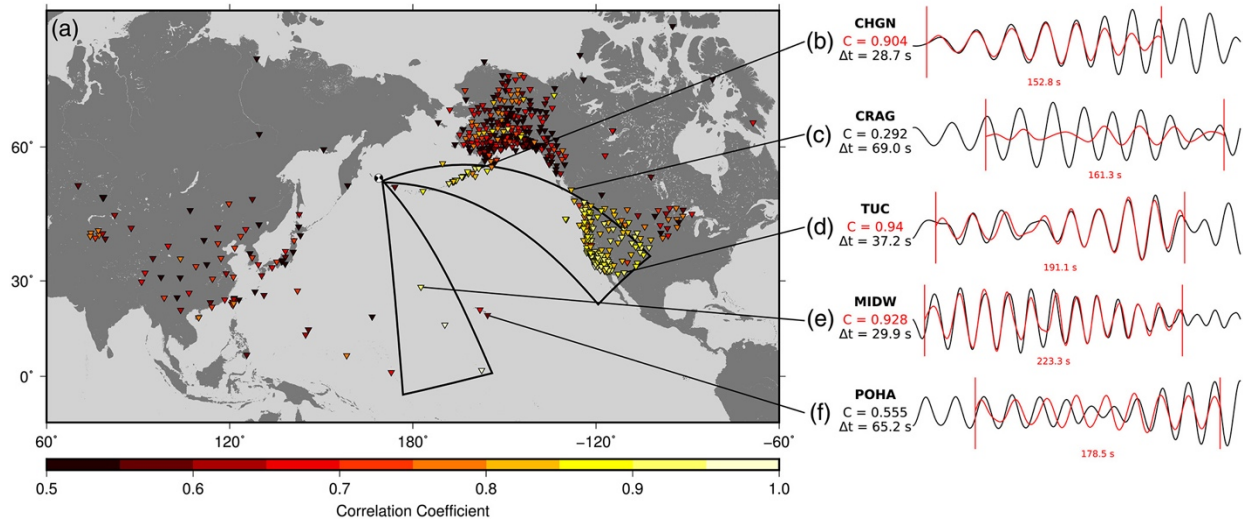


Figure B3. Far-field surface wave observations for supershear rupture validation. (a) The inverted triangles are seismic stations, colored according to the maximum cross-correlation value found during the validation process. The centroid-moment tensor shows the epicenter of the MW 7.7 mainshock. The black lines show the locations of the Mach cones. For supershear ruptures, large cross-correlation values are expected within the Mach cones. (b–f) Five examples are selected from a total of 634 cross-correlations and their locations are shown with a black line in (a). Black and red traces show filtered (15–25 s) Rayleigh waves from the MW 7.7 mainshock and the MW 6.3 foreshock, respectively. Foreshock amplitudes are scaled by the inferred moment ratio of the supershear segment and the foreshock. C is the maximum cross-correlation value, and Δt is the time shift associated with this value. Nonzero time shifts

are due to the initial subshear segment of the mainshock rupture. The cross-correlation time window is labeled in red and outlined by vertical red bars. (b), (d), and (e) are examples of Rayleigh waves recorded within the Mach cones. Note the high cross-correlation values and similar scaled amplitudes. (c) and (f) are examples of Rayleigh waves recorded outside the Mach cones. Note the low correlation values and variable scaled amplitudes.

5. Discussion and Conclusions

Earthquake ruptures that transition to supershear rupture velocities were initially explained by mechanisms on planar mode II (e.g., strike-slip) cracks (Andrews, 1976; Burridge, 1973), and many of the first observations of supershear ruptures were sustained on simple, continuous sections of strike-slip faults (Bouchon et al., 2010). Although supershear propagation may preferentially occur on simple fault geometries, numerical studies have shown that stress and frictional strength heterogeneities, likely related to fault complexity, may cause a rupture to transition to supershear speeds (e.g., Bruhat et al., 2016; Dunham, 2007; Liu & Lapusta, 2008). Dynamic rupture models have directly shown that supershear transitions on complex systems of faults such as fault stepovers may also occur (Hu et al., 2016; Ryan & Oglesby, 2014). Ryan and Oglesby (2014) explain that in this type of scenario, the sudden termination of an earthquake rupture at the end of the primary fault changes the stress field across the fault system, enabling the secondary fault to rupture at supershear speeds by increasing the shear stress and decreasing the normal stress at the beginning of the secondary fault. This type of supershear transition mechanism can occur on both compressional and extensional fault stepover systems, although high initial stresses are required. Consequently, high initial stresses also allow ruptures to jump across larger stepover widths.

The regional back-projection result and the independent Rayleigh wave validation show that the 2017 Komandorsky Islands earthquake accelerated from a sub-Rayleigh velocity of 2.1 km/s on Segment 1 to a supershear velocity of 5.0 km/s on Segment 3. The end of Segment 1 is associated with high amplitudes of high-frequency seismic radiation, consistent with stopping phases from the sudden termination of a rupture (Madariaga, 1976). Segment 2 is associated with a decrease in source amplitude (Figure B2b), indicative of a discontinuous rupture (Kiser & Ishii, 2013). Upon re nucleation at the start of Segment 3, the rupture immediately begins to propagate at supershear speeds. This feature differentiates the 2017 Komandorsky Islands supershear transition mechanism from the classical Burridge-Andrews mechanism, which requires some sub-Rayleigh propagation distance prior to the onset of a supershear rupture (Andrews, 1976). The southeastern portion of this earthquake likely achieved supershear speeds via the mechanism described by Ryan and Oglesby (2014), jumping between two offset faults of a fault stepover system (Segments 1 and 3) and accelerating to supershear speeds immediately following re nucleation on the secondary fault (Segment 3). Local bathymetric features (Tozer et al., 2019) illustrate the complexity of this fault system, revealing a basin between Segments 1 and 3 that is characteristic of an extensional basin in a right-stepping right-lateral fault system (Figures B2a and Figure B4).

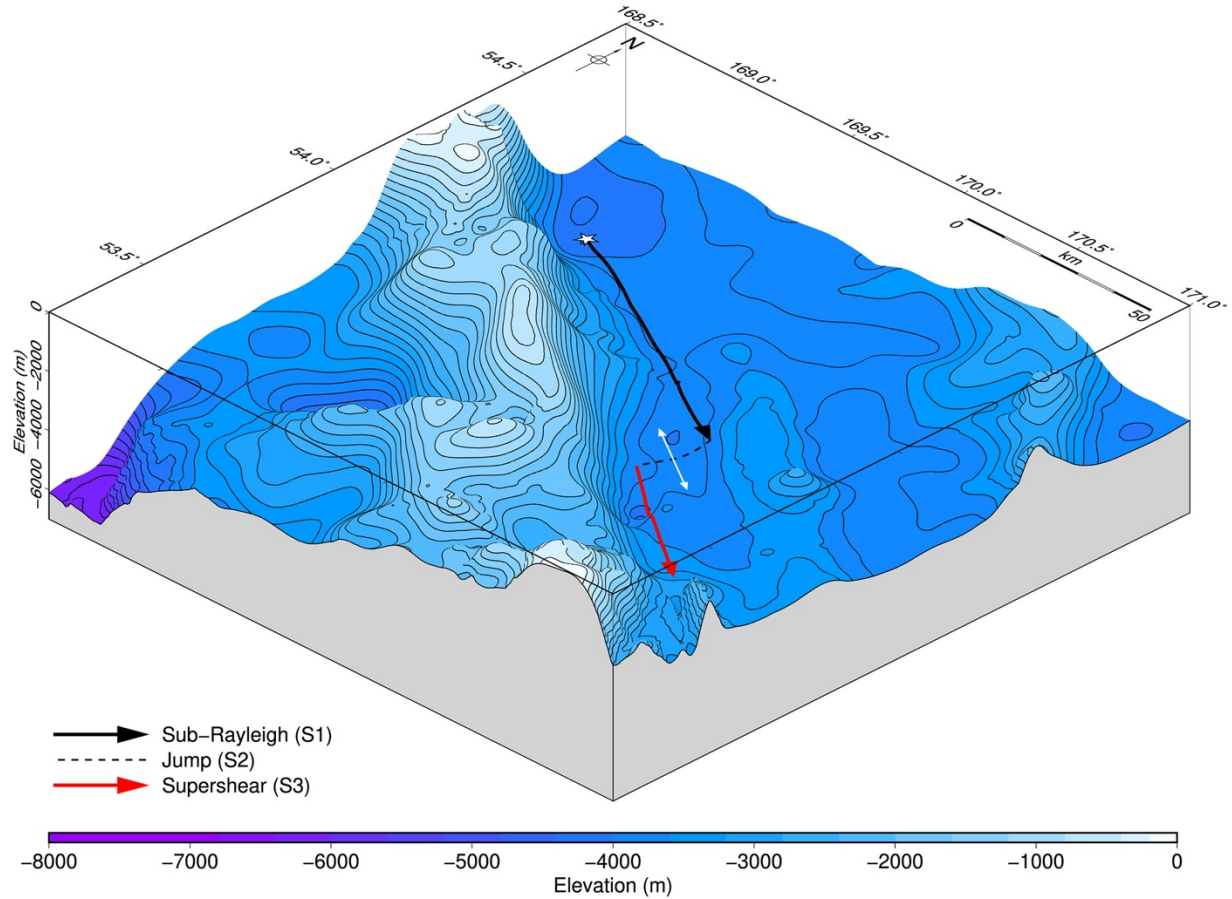


Figure B4. Schematic representation of the southeastern rupture of the 2017 Komandorsky Islands earthquake. The white star shows the epicenter of the 2017 Komandorsky Islands earthquake. The black and red arrows show the approximate location and direction of the sub-Rayleigh Segment 1 (S1) and the supershear Segment 3 (S3), respectively. The dashed black line shows the rupture jump across a basin, represented as Segment 2 (S2) in the main back-projection result. The white arrows show the relative motion across this segment, given the right-lateral right-stepping strike-slip fault system. The contours (plotted every 200 m) are the same as those in Figure B2.

The complexity of this fault system is further delineated by the distribution of aftershocks associated with the 2017 Komandorsky Islands earthquake. The majority of these aftershocks

occur immediately southeast of the mainshock epicenter and decrease near 170°E (Figure B1b). This observation may be explained by the supershear segment of the mainshock rupture, which began near 170°E and ruptured southeast. Faults that achieve supershear speeds are often associated with a distinct lack of aftershocks (Bouchon & Karabulut, 2008), which instead occur on faults adjacent to the main rupture plane. This phenomenon is thought to be caused by the complete release of stress on the main fault by the supershear rupture and the activation of fault splays by the expansive supershear shock wave.

Rupture speed plays a critical role in the damage caused by earthquakes (Das, 2007). In particular, supershear earthquakes have the potential to transfer large stresses and generate strong ground motion at far distances from the ruptured fault (Dunham & Bhat, 2008). The majority of supershear earthquakes have ruptured on smooth, continuous sections of strike-slip faults (Bouchon et al., 2010), but supershear transitions tend to coincide with increased fault complexity. The 2001 Mw 7.8 Kokoxili (Kunlun) earthquake reached supershear speeds in an area exhibiting a change in rupture azimuth and a large push-up structure (Vallée et al., 2008). The 2015 Mw 7.2 Murghab, Tajikistan earthquake temporarily slowed down through a restraining bend connecting two continuous sections of a fault rupturing at supershear speeds (Sangha et al., 2017). The 2018 Mw 7.5 Palu earthquake reached supershear speeds immediately following nucleation, likely due to fault roughness near the epicenter (Bao et al., 2019). Like these three earthquakes, the 2017 Mw 7.7 Komandorsky Islands earthquake achieved supershear speeds over a geometrically complex fault system. However, the observed transition mechanism across a fault stepover is expected to facilitate supershear rupture speeds within an initial stress field that precludes supershear transitions via the standard Burridge-Andrews mechanism (Hu et al., 2016; Ryan & Oglesby, 2014). The majority of strike-slip fault systems contain complexity

in the form of fault stepovers (Wesnousky, 2006), and many of these areas are situated near large population centers (e.g., the San Andreas Fault, the North Anatolian Fault). The ability for a rupture to not only jump large stepover widths but also transition to supershear speeds across a fault stepover system is of great importance to the evaluation of global seismic hazard.

Acknowledgments

The authors would like to thank two anonymous reviewers and the editor, Gavin Hayes, for their constructive comments and suggestions. Additional conversations with Han Bao and Colton Lynner have helped improve the results presented in this manuscript. Seismic data used in this study were downloaded from the IRIS Consortium (http://ds.iris.edu/wilber3/find_event), the NCECD (<https://www.doi.org/10.7932/NCEDC>), and the SCEDC (<https://doi.org/10.7909/C3WD3xH1>). The Generic Mapping Tools (GMT) were used to create figures presented in this manuscript. The Python software package ObsPy and a cross-correlation code written by Tom Eulenfeld were used in the Rayleigh wave cross-correlation analysis. This research was supported by National Science Foundation grant EAR-1802441. The back-projection results are available in the supporting information.

References

- Andrews, D. J. (1976). Rupture velocity of plane strain shear cracks. *Journal of Geophysical Research*, 81(32), 5679–5687. <https://doi.org/10.1029/JB081i032p05679>
- Archuleta, R. J. (1984). A faulting model for the 1979 Imperial Valley earthquake. *Journal of Geophysical Research*, 89(B6), 4559–4585. <https://doi.org/10.1029/JB089iB06p04559>
- Avé Lallement, H. G. (1996). Displacement partitioning and arc-parallel extension in the Aleutian volcanic island arc. *Tectonophysics*, 256(1–4), 279–293. [https://doi.org/10.1016/0040-1951\(95\)00171-9](https://doi.org/10.1016/0040-1951(95)00171-9)
- Bao, H., Ampuero, J.-P., Meng, L., Fielding, E. J., Liang, C., Milliner, C. W. D., Feng, T., & Huang, H. (2019). Early and persistent supershear rupture of the 2018 magnitude 7.5 Palu earthquake. *Nature Geoscience*, 12(3), 200–205. <https://doi.org/10.1038/s41561-018-0297-z>
- Bouchon, M., Bouin, M.-P., Karabulut, H., Toksöz, M. N., Dietrich, M., & Rosakis, A. J. (2001). How fast is rupture during an earthquake? New insights from the 1999 Turkey earthquakes. *Geophysical Research Letters*, 28(14), 2723–2726. <https://doi.org/10.1029/2001GL013112>
- Bouchon, M., & Karabulut, H. (2008). The aftershock signature of Supershear earthquakes. *Science*, 320(5881), 1323–1325. <https://doi.org/10.1126/science.1155030>
- Bouchon, M., Karabulut, H., Bouin, M. P., Schmittbuhl, J., Vallée, M., Archuleta, R., Das, S., Renard, F., & Marsan, D. (2010). Faulting characteristics of supershear earthquakes. *Tectonophysics*, 493(3–4), 244–253. <https://doi.org/10.1016/j.tecto.2010.06.011>
- Bouchon, M., Toksöz, N., Karabulut, H., Bouin, M.-P., Dietrich, M., Aktar, M., & Edie, M. (2000). Seismic imaging of the 1999 Izmit (Turkey) rupture inferred from the near-fault

recordings. *Geophysical Research Letters*, 27(18), 3013–3016.

<https://doi.org/10.1029/2000GL011761>

Bruhat, L., Fang, Z., & Dunham, E. M. (2016). Rupture complexity and the supershear transition on rough faults. *Journal of Geophysical Research: Solid Earth*, 121, 210–224.

<https://doi.org/10.1002/2015JB012512>

Burridge, R. (1973). Admissible speeds for plane-strain self-similar shear cracks with friction but lacking cohesion. *Geophysical Journal International*, 35(4), 439–455.

<https://doi.org/10.1111/j.1365-246X.1973.tb00608.x>

Cross, R. S., & Freymueller, J. T. (2008). Evidence for and implications of a Bering plate based on geodetic measurements from the Aleutians and western Alaska. *Journal of Geophysical Research*, 113, B07405. <https://doi.org/10.1029/2007JB005136>

Das, S. (2007). The need to study speed. *Science*, 317(5840), 905–906.

DeMets, C., Gordon, R. G., & Argus, D. F. (2010). Geologically current plate motions. *Geophysical Journal International*, 181(1), 1–80. <https://doi.org/10.1111/j.1365-246X.2009.04491.x>

Dunham, E. M. (2007). Conditions governing the occurrence of supershear ruptures under slip-weakening friction. *Journal of Geophysical Research*, 112, B07302.

<https://doi.org/10.1029/2006JB004717>

Dunham, E. M., & Archuleta, R. J. (2004). Evidence for a Supershear transient during the 2002 Denali Fault earthquake. *Bulletin of the Seismological Society of America*, 94(6B), S256–S268. <https://doi.org/10.1785/0120040616>

Dunham, E. M., & Bhat, H. S. (2008). Attenuation of radiated ground motion and stresses from three-dimensional supershear ruptures. *Journal of Geophysical Research*, 113, B08319.
<https://doi.org/10.1029/2007JB005182>

Dziewonski, A. M., Chou, T.-A., & Woodhouse, J. H. (1981). Determination of earthquake source parameters from waveform data for studies of global and regional seismicity. *Journal of Geophysical Research*, 86(B4), 2825–2852.
<https://doi.org/10.1029/JB086iB04p02825>

Ekström, G., Nettles, M., & Dziewoński, A. M. (2012). The global CMT project 2004–2010: Centroid-moment tensors for 13,017 earthquakes. *Physics of the Earth and Planetary Interiors*, 200–201, 1–9. <https://doi.org/10.1016/J.PEPI.2012.04.002>

Ekström, G. (2011). A global model of Love and Rayleigh surface wave dispersion and anisotropy, 25–250 s. *Geophysical Journal International*, 187(3), 1668–1686.
<https://doi.org/10.1111/j.1365-246X.2011.05225.x>

Holland, J. H. (1992). *Adaptation in Natural and Artificial Systems: An Introductory Analysis with Applications to Biology, Control, and Artificial Intelligence*. Cambridge, MA: MIT Press.

Hu, F., Xu, J., Zhang, Z., & Chen, X. (2016). Supershear transition mechanism induced by step over geometry. *Journal of Geophysical Research: Solid Earth*, 121, 8738–8749.
<https://doi.org/10.1002/2016JB013333>

Ishii, M. (2011). High-frequency rupture properties of the Mw 9.0 off the Pacific coast of Tohoku earthquake. *Earth, Planets and Space*, 63(7), 609–614.
<https://doi.org/10.5047/eps.2011.07.009>

Ishii, M., Shearer, P. M., Houston, H., & Vidale, J. E. (2005). Extent, duration and speed of the 2004 Sumatra-Andaman earthquake imaged by the Hi-Net array. *Nature*, 435(7044), 933–936. <https://doi.org/10.1038/nature03675>

Ishii, M., Shearer, P. M., Houston, H., & Vidale, J. E. (2007). Teleseismic P wave imaging of the 26 December 2004 Sumatra-Andaman and 28 March 2005 Sumatra earthquake ruptures using the Hi-net array. *Journal of Geophysical Research*, 112, B11307. <https://doi.org/10.1029/2006JB004700>

Kehoe, H. L., Kiser, E. D., & Okubo, P. G. (2019). The rupture process of the 2018 Mw 6.9 Hawai'i earthquake as imaged by a genetic algorithm-based back-projection technique. *Geophysical Research Letters*, 46, 2467–2474. <https://doi.org/10.1029/2018GL080397>

Kennett, B. L. N., & Engdahl, E. R. (1991). traveltimes for global earthquake location and phase identification. *Geophysical Journal International*, 105(2), 429–465. <https://doi.org/10.1111/j.1365-246X.1991.tb06724.x>

Kiser, E., & Ishii, M. (2011). The 2010 Mw 8.8 Chile earthquake: Triggering on multiple segments and frequency-dependent rupture behavior. *Geophysical Research Letters*, 38, L07301. <https://doi.org/10.1029/2011GL047140>

Kiser, E., & Ishii, M. (2013, April). The 2010 Maule, Chile, coseismic gap and its relationship to the 25 march 2012 MW 7.1 earthquake. *Bulletin of the Seismological Society of America*, 103(2A), 1148–1153. <https://doi.org/10.1785/0120120209>

Kiser, E., & Ishii, M. (2017). Back-projection imaging of earthquakes. *Annual Review of Earth and Planetary Sciences*, 45(1), 271–299. <https://doi.org/10.1146/annurev-earth-063016-015801>

Kogan, M. G., Frolov, D. I., Vasilenko, N. F., Freymueller, J. T., Steblov, G. M., Ekström, G.,

Titkov, N. N., & Prytkov, A. S. (2017). Plate coupling and strain in the far western Aleutian arc modeled from GPS data. *Geophysical Research Letters*, 44, 3176–3183.
<https://doi.org/10.1002/2017GL072735>

Konca, A. O., Leprince, S., Avouac, J.-P., & Helmberger, D. V. (2010). Rupture process of the 1999 Mw 7.1 Duzce earthquake from joint analysis of SPOT, GPS, InSAR, strong-motion, and Teleseismic data: A Supershear rupture with variable rupture velocity. *Bulletin of the Seismological Society of America*, 100(1), 267–288.

<https://doi.org/10.1785/0120090072>

Koper, K. D., Hutko, A. R., Lay, T., Ammon, C. J., & Kanamori, H. (2011). Frequency-dependent rupture process of the 2011 Mw 9.0 Tohoku earthquake: Comparison of short-period P wave backprojection images and broadband seismic rupture models. *Earth, Planets and Space*, 63(7), 599–602. <https://doi.org/10.5047/eps.2011.05.026>

Laske, G., Masters, G., Ma, Z., & Pasyanos, M. (2013). Update on CRUST1.0—A 1-degree global model of Earth's crust. *Geophysical Research Abstracts*, 15.

Lay, T., Ye, L., Bai, Y., Cheung, K. F., Kanamori, H., Freymueller, J., Steblov, G. M., & Kogan, M. G. (2017). Rupture along 400 km of the Bering Fracture Zone in the Komandorsky Islands earthquake (MW 7.8) of 17 July 2017. *Geophysical Research Letters*, 44, 12,161–12,169. <https://doi.org/10.1002/2017GL076148>

Liu, Y., & Lapusta, N. (2008). Transition of mode II cracks from sub-Rayleigh to intersonic speeds in the presence of favorable heterogeneity. *Journal of the Mechanics and Physics of Solids*, 56(1), 25–50. <https://doi.org/10.1016/j.jmps.2007.06.005>

- Lutikov, A. I., Rogozhin, E. A., Dontsova, G. Y., & Zhukovets, V. N. (2019). The MW 7.8 earthquake of July 17, 2017 off the Commander Islands and other large earthquakes at the Western segment of the Aleutian Island arc. *Journal of Volcanology and Seismology*, 13(2), 112–123. <https://doi.org/10.1134/S0742046319020052>
- Madariaga, R. (1976). Dynamics of an expanding circular fault. *Bulletin of the Seismological Society of America*, 66(3), 639–666. <https://doi.org/10.2307/1779766>
- Meng, L., Inbal, A., & Ampuero, J.-P. (2011). A window into the complexity of the dynamic rupture of the 2011 mw 9 Tohoku-Oki earthquake. *Geophysical Research Letters*, 38, L00G07. <https://doi.org/10.1029/2011GL048118>
- Newberry, J. T., Laclair, D. L., & Fujita, K. (1986). Seismicity and tectonics of the far Western Aleutian Islands. *Journal of Geodynamics*, 6(1–4), 13–32. [https://doi.org/10.1016/0264-3707\(86\)90030-X](https://doi.org/10.1016/0264-3707(86)90030-X)
- Ryan, K. J., & Oglesby, D. D. (2014). Dynamically modeling fault step overs using various friction laws. *Journal of Geophysical Research: Solid Earth*, 119, 5814–5829. <https://doi.org/10.1002/2014JB011151>
- Sangha, S., Peltzer, G., Zhang, A., Meng, L., Liang, C., Lundgren, P., & Fielding, E. (2017). Fault geometry of 2015, Mw7.2 Murghab, Tajikistan earthquake controls rupture propagation: Insights from InSAR and seismological data. *Earth and Planetary Science Letters*, 462, 132–141. <https://doi.org/10.1016/j.epsl.2017.01.018>
- Tozer, B., Sandwell, D. T., Smith, W. H. F., Olson, C., Beale, J. R., & Wessel, P. (2019). Global bathymetry and topography at 15 arc seconds: SRTM15+. *Earth and Space Science*, 6. <https://doi.org/10.1029/2019ea000658>

Vallée, M., & Dunham, E. M. (2012). Observation of far-field Mach waves generated by the 2001 Kokoxili supershear earthquake. *Geophysical Research Letters*, 39, L05311.
<https://doi.org/10.1029/2011GL050725>

Vallée, M., Landès, M., Shapiro, N. M., & Klinger, Y. (2008). The 14 November 2001 Kokoxili (Tibet) earthquake: High-frequency seismic radiation originating from the transitions between sub-Rayleigh and supershear rupture velocity regimes. *Journal of Geophysical Research*, 113, B07305. <https://doi.org/10.1029/2007JB005520>

Walker, K. T., & Shearer, P. M. (2009). Illuminating the near-sonic rupture velocities of the intracontinental Kokoxili Mw 7.8 and Denali fault Mw 7.9 strike-slip earthquakes with global P wave back projection imaging. *Journal of Geophysical Research*, 114, B02304.
<https://doi.org/10.1029/2008JB005738>

Wang, D., & Mori, J. (2011). Frequency-dependent energy radiation and fault coupling for the 2010 Mw8.8 Maule, Chile, and 2011 Mw9.0 Tohoku, Japan, earthquakes. *Geophysical Research Letters*, 38, L22308. <https://doi.org/10.1029/2011GL049652>

Wang, D., Mori, J., & Uchide, T. (2012). Supershear rupture on multiple faults for the Mw 8.6 off northern Sumatra, Indonesia earthquake of April 11, 2012. *Geophysical Research Letters*, 39, L21307. <https://doi.org/10.1029/2012GL053622>

Wesnousky, S. G. (2006). Predicting the endpoints of earthquake ruptures. *Nature*, 444(7117), 358–360. <https://doi.org/10.1038/nature05275>

Yue, H., Lay, T., Freymueller, J. T., Ding, K., Rivera, L., Ruppert, N. A., & Koper, K. D. (2013). Supershear rupture of the 5 January 2013 Craig, Alaska (Mw 7.5) earthquake. *Journal of Geophysical Research: Solid Earth*, 118, 5903–5919.
<https://doi.org/10.1002/2013JB010594>

Supporting Information

Introduction

The supporting information includes eight supporting movies of the 2017 Mw 7.7 Komandorsky Islands earthquake (Movies BS1–BS8), eight supporting data sets of the central source locations associated with Movies BS1–BS8 (Data Sets BS1–BS8), text describing the genetic algorithm-based station selection method (Text BS1), and six figures supporting the main text (Figures BS1–BS6).

Data used to create Movies BS1–BS8 and Data Sets BS1–BS8 were received from the Incorporated Research Institutions for Seismology (IRIS) Consortium in February 2019. The data was processed according to the steps described in the methods section of the main paper and the supporting text.

Text BS1

Here we outline the genetic algorithm-based station selection method used for selecting an optimal seismic network for back-projection. The genetic algorithm is an iterative process, initialized with 25 random subsets of stations, represented by a binary string of length M where a one indicates that a station is used in the back-projection analysis and a zero indicates that a station is not used in the back-projection analysis. For each subset of stations, a back-projection analysis of the point source event is performed, and a waveform stack is produced for each back-projection grid point. The stacks are squared and integrated over a moving time window before a maximum amplitude value is assigned to each respective grid point at each time step. In this case, a total of 61 time steps are used (20 before, 1 during, and 40 after the point source event

origin time). Maximum amplitude values at each grid point are multiplied at each time step by the following Gaussian function $g(t)$:

$$g(t) = e^{\frac{(t - \frac{t_{tot}+1}{2})^2}{2\sigma^2}}, \text{ for } t \in \{1, 2, \dots, 61\}$$

where t_{tot} is the total number of time steps and σ is the Gaussian RMS width (a value of 25 is used). This step increases the weight of amplitudes at time steps away from the origin time, encouraging the genetic algorithm to select a subset of stations that image the point source impulsively near the origin time and reduce temporal artifacts. The weighted amplitude value for each grid point is summed and normalized across all time steps and a fitness value for each back-projection analysis is calculated from the summed and normalized grid point values, according to the following fitness function (ϕ):

$$\phi = (1 - \lambda) \frac{N_{low}}{N_{tot} - 1} + \lambda \frac{1}{N_{high}}$$

where N_{low} is the number of grid point values below 40% of the maximum value of all grid point values, N_{high} is the number of grid point values above 80% of the maximum value of all grid point values, N_{tot} is the total number of grid point values, and λ is the weighting parameter (a value of $\frac{1}{2}$ is used to equally weight the contribution of N_{low} and N_{high}). A back-projection analysis will have a fitness value of one for a perfect spatiotemporal point source (i.e., a maximum amplitude at one grid point during one time step) and approach $\lambda \frac{1}{N_{tot}}$ as the imaged source broadens in space and time.

The fitness value describes the spatiotemporal point source nature of a back-projection analysis as a single value, which is then used to determine the probability that a given subset of stations will be used in the crossover step via roulette wheel selection, also known as fitness proportionate selection (Holland, 1992). This process finds a random point on two binary strings

(those with higher fitness values are more likely to be selected) and combines the leading section of one binary string with the trailing section of the second binary string, creating a new binary string. This combines the traits of two subsets of stations with high fitness values into a new subset of stations. There is a 70% probability that any given subset of stations will be replaced by a new subset of stations via this crossover step. Otherwise, the subset of stations from the previous iteration continues to the next iteration. This crossover probability is implemented to slow convergence towards a solution, thereby searching more of the solution space. After this process, there is a small probability (1%) that any random bit within any binary string will be flipped. This process mimics mutation, also slowing solution convergence and allowing more of the solution space to be searched. Of the 25 subsets of stations created for the next iteration, 24 are created using this approach. The last subset of stations is the previous iteration's subset of stations with the largest fitness value (elite subset of stations). The elite subset of stations may only exist for 5 iterations, at which point it is replaced with a random subset of stations. This is a third technique to search more of the solution space. After the maximum fitness per iteration stabilizes, the genetic algorithm is terminated (Figure BS1). The subset of stations with the highest value after 150 iterations of the genetic algorithm is the optimized network (Figure B1a) which is used in the back-projection analysis of the 2017 Komandorsky Islands earthquake.

Interestingly, the distribution of optimized and removed stations appears to be somewhat random and does not exhibit strong spatial patterns associated with the arrival of unwanted phases at certain distance and azimuth windows. However, an overall declustering of stations within the optimized network is observed in regions of particularly dense station coverage (Figure B1a). This may be linked to the genetic algorithm-based station selection method's inherent optimization of the array response function (ARF), which depends on the aperture,

shape, interstation spacing, and configuration of the array. The combination of the ARF optimization, the removal of noisy data, and the removal of data containing unwanted or misaligned phase arrivals may result in a seemingly random station distribution.

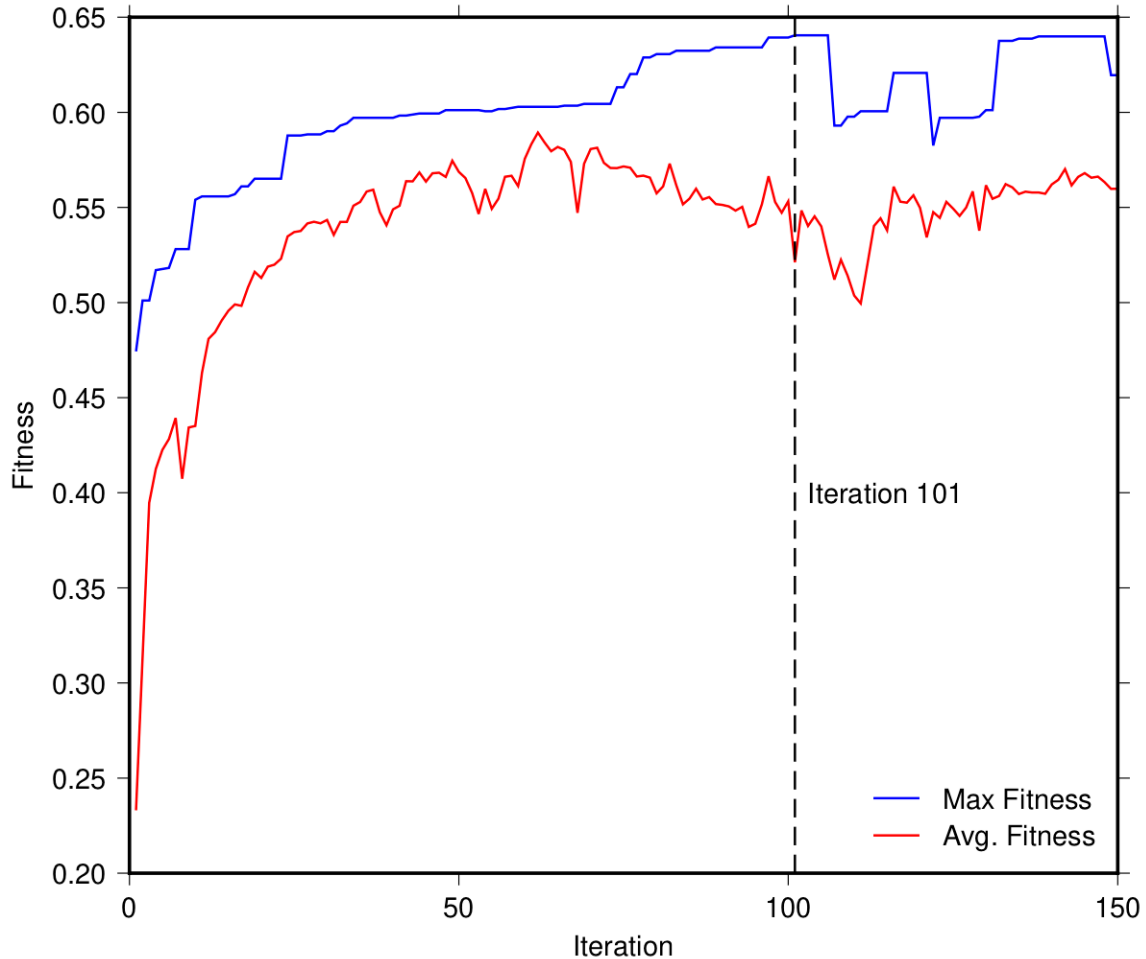


Figure BS1. Genetic algorithm optimization curve. The subset of stations with the highest fitness value (elite subset of stations) is plotted in blue as a function of iteration. The average fitness of all subsets of stations is plotted in red as a function of iteration. The largest maximum fitness value is achieved at iteration 101 (black dashed line) and the corresponding subset of stations is called the optimized network and is used in the mainshock back-projection analysis.

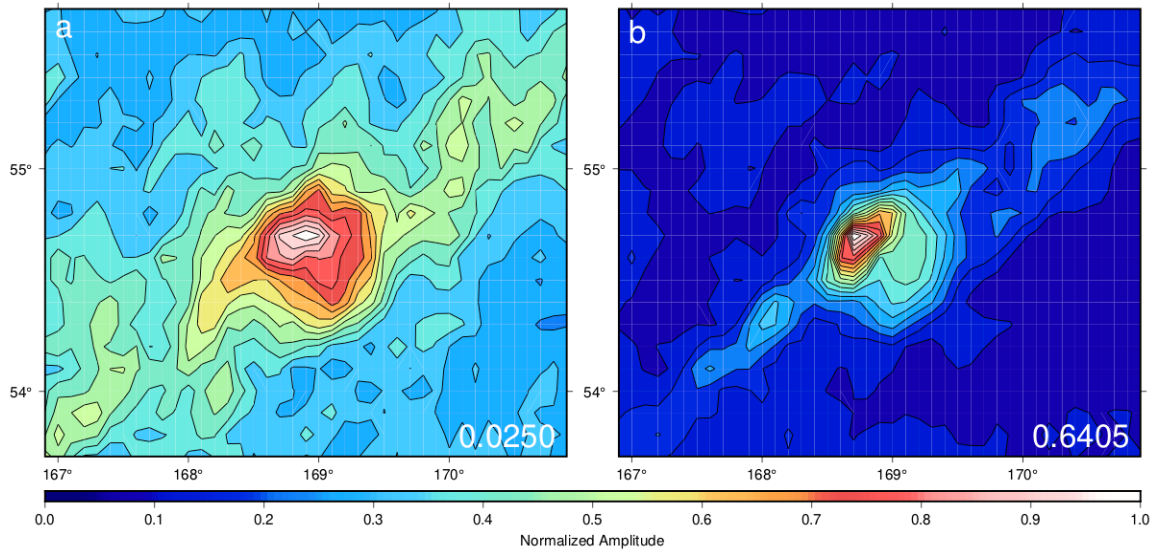


Figure BS2. Genetic algorithm source image improvement. (a) The linear back-projection result of the point source event with the full seismic network. (b) The linear back-projection result of the point source event with the optimized seismic network. The fitness (see Text BS1) of each result is displayed in the bottom right corner of each panel.

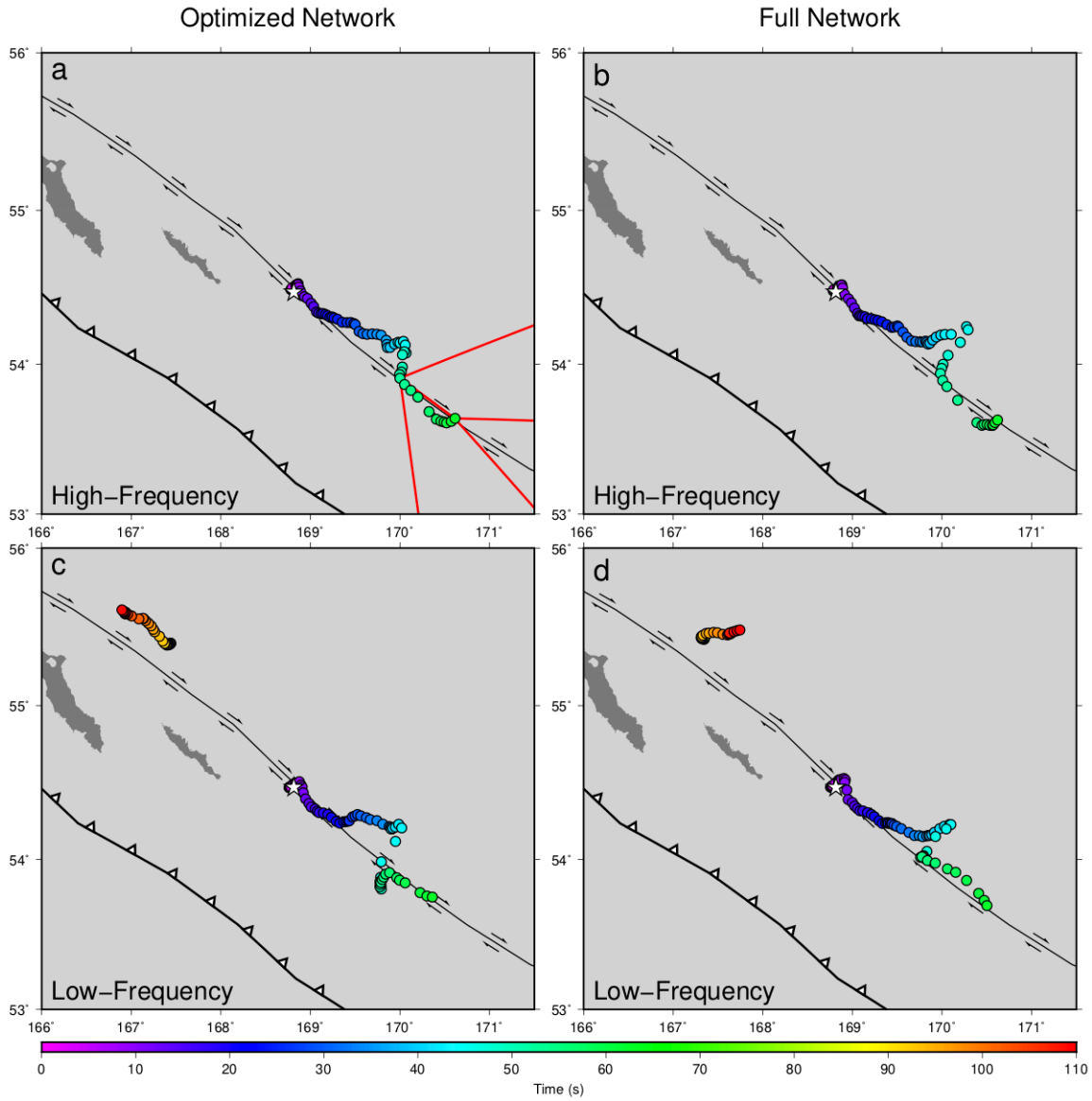


Figure BS3. Mainshock frequency dependence. (a–d) The rainbow dots are determined from the coherence-based back-projection result and show the central source locations of the 2017 Komandorsky Islands earthquake. The color of the dots indicates the time with respect to origin time (0 s). The Aleutian Trench is shown as a black line with white triangles on the overriding plate. The Bering Fracture Zone (BFZ) is shown as a black line with right-lateral strike-slip arrows. The area between the Aleutian Trench and BFZ is the Komandorsky Sliver. The two dark grey islands are the Komandorsky Islands. The white star shows the mainshock

epicenter. (a) and (c) are back-projected using the optimized seismic network and (b) and (d) are back-projected using the full seismic network. (a) and (b) are the high-frequency back-projection results. (c) and (d) are the low-frequency back-projection results. The red lines in (a) are the estimated Mach cone locations with respect to the supershear rupture segment. The northwestern rupture is only resolved using low-frequency data and the optimized network (c). The imaged northwestern rupture in (d) is dominated by an eastward moving artifact.

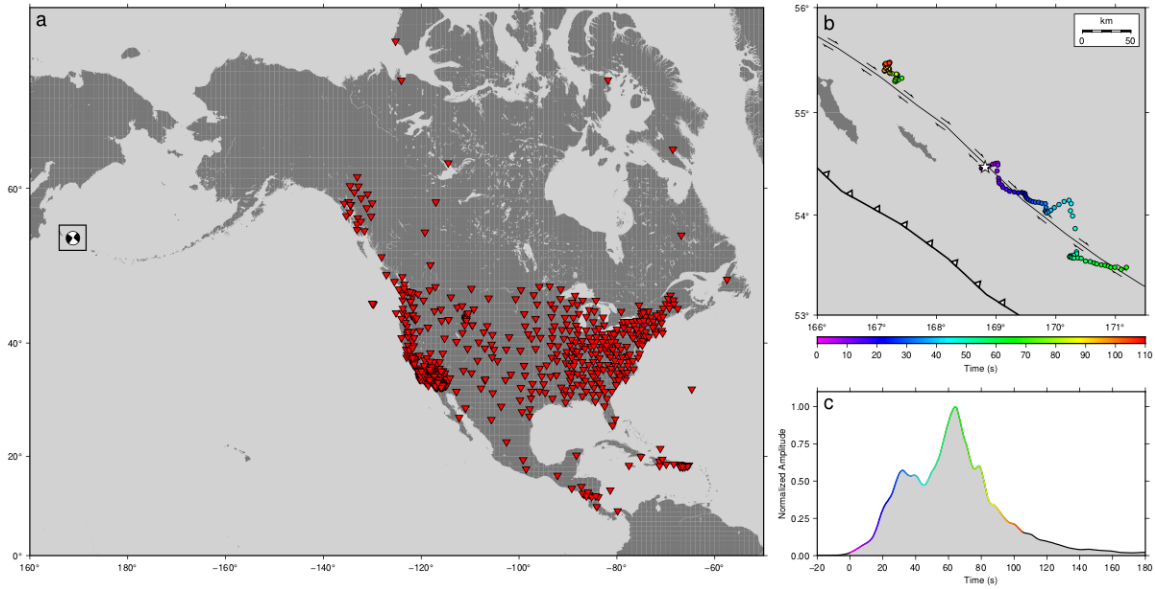


Figure BS4. Telescismic station distribution and back-projection result. (a) The centroid-moment tensor shows the location of the 2017 Komandorsky Islands earthquake. The red inverted triangles show the 678 seismic stations used in the telescismic back-projection analysis. The black box outlines the location of the map area in (b). (b) The white star shows the 2017 Komandorsky Islands epicenter. The rainbow dots are determined from the telescismic coherence-based back-projection result and show the central source locations of the mainshock rupture. The color of the dots indicates time with respect to origin time (0 s).

The Aleutian Trench is shown as a black line with white triangles on the overriding plate. The Bering Fracture Zone (BFZ) is shown as a black line with right-lateral strike-slip arrows. The area between the Aleutian Trench and BFZ is the Komandorsky Sliver. The two dark grey islands are the Komandorsky Islands. (c) The normalized amplitude of energy release as a function of time is determined from the linear teleseismic back-projection result and shown for the 2017 Komandorsky Islands earthquake. The rainbow line of the source time function corresponds to the rainbow dots used in (a).

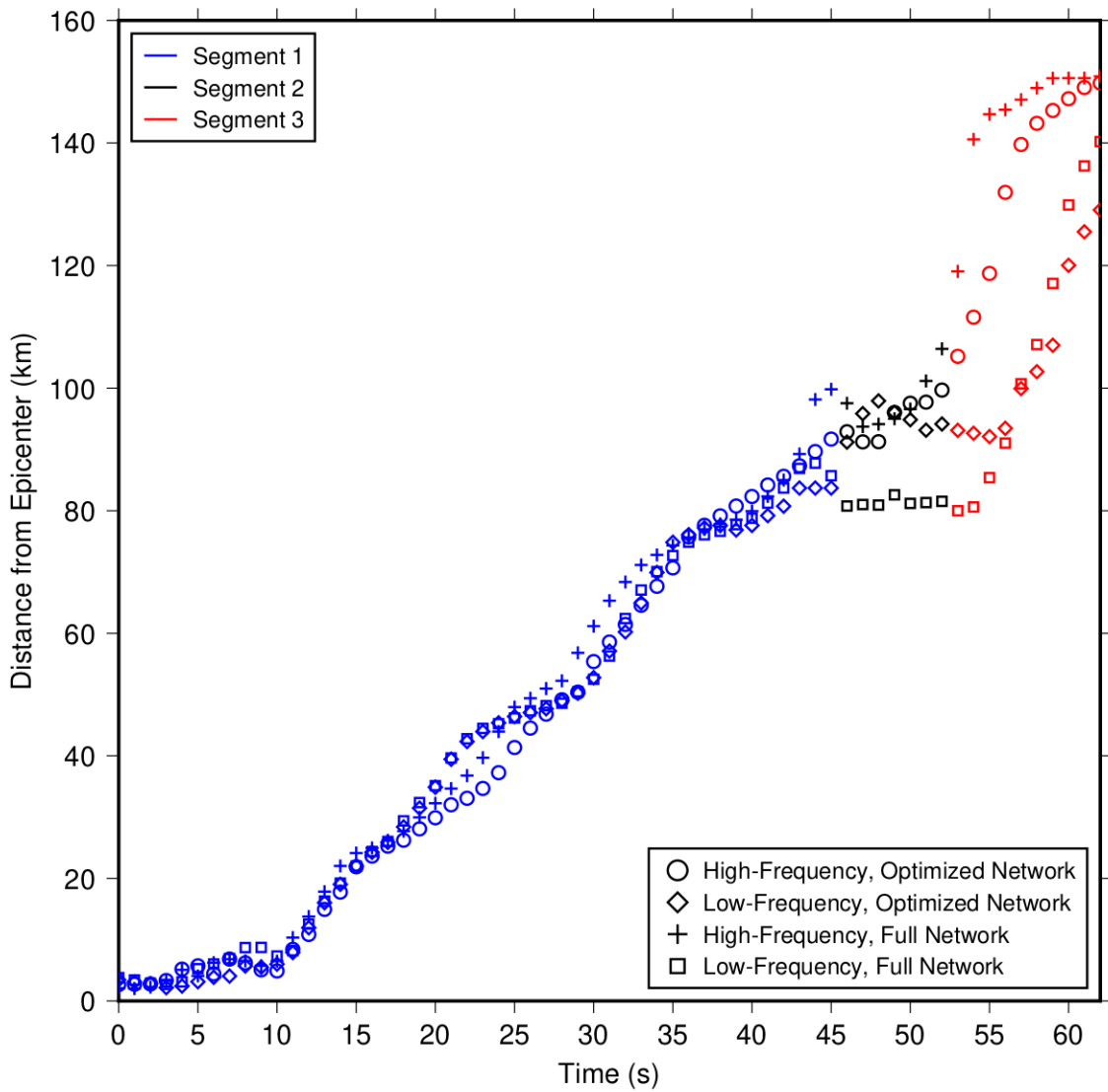


Figure BS5. Epicentral distances of back-projection source locations as a function of time.

The distance between each source location in the southeastern back-projection results (Figure BS3) and the epicenter are calculated at 1 s time steps. The plot shows a steady increase in calculated distances during Segments 1 and 3 (blue and red, respectively), but a flattening of these values during Segment 2 (black). This is indicative of the perpendicular direction of Segment 2 and the highly segmented nature of the entire southeastern rupture.

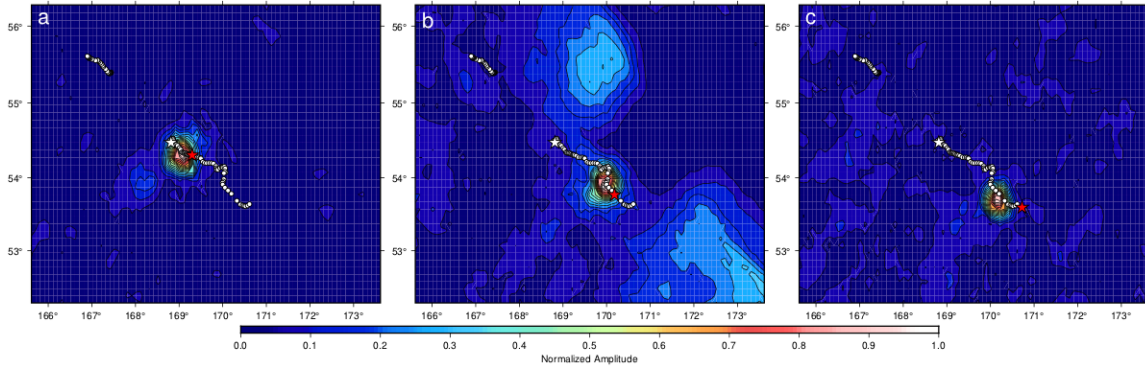


Figure BS6. Back-projection locations of aftershocks along the southeastern rupture. (a–c) The back-projection results of three aftershocks, each near a segment of the imaged southeastern rupture, are shown with respect to the reported NEIC epicenter (red star). The mainshock epicenter is shown with a white star and the resulting rupture is shown with white dots. This analysis shows a systematic southeastward shift between the estimated aftershock back-projection locations and the NEIC epicenters. This indicates that the spatial uncertainty due to three-dimensional heterogeneity in the main back-projection result is in the direction of rupture. Thus, the relative offset between Segments 1 and 3 is a robust feature of our back-projection result. The aftershock used in (a) occurred on 28 July 2017 and had a moment magnitude of 5.5 (02:39:15 UTC, 54.303°N 169.301°E; NEIC: <https://earthquake.usgs.gov/earthquakes/eventpage/us2000a21g/executive>). The aftershock used in (b) occurred on 18 July 2017 and had a body wave magnitude of 5.0 (01:06:35 UTC, 53.767°N 170.181°E; NEIC: <https://earthquake.usgs.gov/earthquakes/eventpage/us20009x6j/executive>). The side lobes in (b) are likely due to the occurrence of the aftershock within 2 hours of the mainshock. The aftershock used in (c) occurred on 23 July 2017 and had a moment magnitude of 5.1 (04:10:06

UTC, 53.600°N 170.727°E; NEIC:
<https://earthquake.usgs.gov/earthquakes/eventpage/us20009zxe/executive>).

The following supporting information (Movies BS1–BS8, Data Sets BS1–BS8) are available for download at <https://doi.org/10.1029/2020GL087400>.

Movie BS1. Regional back-projection result of the southeastern rupture using high-frequency (0.8 to 2 Hz) data and the optimized seismic network.

Movie BS2. Regional back-projection result of the northwestern rupture using low-frequency (0.5 to 1 Hz) data and the optimized seismic network.

Movie BS3. Regional back-projection result of the southeastern rupture using low-frequency (0.5 to 1 Hz) data and the optimized seismic network.

Movie BS4. Regional back-projection result of the southeastern rupture using high-frequency (0.8 to 2 Hz) data and the full seismic network.

Movie BS5. Regional back-projection result of the northwestern rupture using low-frequency (0.5 to 1 Hz) data and the full seismic network.

Movie BS6. Regional back-projection result of the southeastern rupture using low-frequency (0.5 to 1 Hz) data and the full seismic network.

Movie BS7. Teleseismic back-projection result of the southeastern rupture using 0.5 to 2 Hz band-pass filtered data.

Movie BS8. Teleseismic back-projection result of the northwestern rupture using 0.5 to 2 Hz band-pass filtered data.

Data Set BS1. Central source locations shown in Movie BS1.

Data Set BS2. Central source locations shown in Movie BS2.

Data Set BS3. Central source locations shown in Movie BS3.

Data Set BS4. Central source locations shown in Movie BS4.

Data Set BS5. Central source locations shown in Movie BS5.

Data Set BS6. Central source locations shown in Movie BS6.

Data Set BS7. Central source locations shown in Movie BS7.

Data Set BS8. Central source locations shown in Movie BS8.

**APPENDIX C: MOMENT-DEPENDENT RUPTURE PROPERTIES OF DEEP-FOCUS
EARTHQUAKES NEAR IZU-BONIN**

H. L. Kehoe¹ and E. D. Kiser¹

¹Department of Geosciences, University of Arizona, Tucson, AZ, USA

Abstract

The physical mechanisms controlling deep-focus earthquakes, or those observed at depths greater than 300 km, remain enigmatic. The leading processes by which deep-focus earthquakes are thought to occur include transformational faulting, thermal runaway, and dehydration embrittlement, but distinguishing observations in support of one or more prevailing mechanisms are needed. In this study, we use a modified back-projection method, data recorded by the Hi-net array in Japan, and a three-dimensional velocity model to produce source images of 19 deep-focus earthquakes within the Izu-Bonin subduction zone. We find that the rupture properties and fault plane orientations of imaged events separate according to reported moment magnitude, indicating the distinct operation of two moment-dependent causal mechanisms of deep-focus earthquakes in this region. We discuss these results in the context of previous observational, laboratory, and numerical studies and emphasize the importance of continued research to validate the dual-mechanism hypothesis both in and outside Izu-Bonin. Such work may not only improve our understanding of the nucleation and propagation of deep-focus earthquakes, but also help clarify slab structure and subduction zone dynamics.

1. Introduction

Despite nearly a century of scientific progress since the discovery of deep earthquakes by Wadati (1928), the physical mechanisms governing these earthquakes remain poorly understood (Frohlich, 2006; Zhan, 2019). Deep earthquakes are typically categorized into two distinct groups: intermediate-depth earthquakes occurring at depths between 70 and 300 km and deep-focus earthquakes occurring at depths below 300 km. Deep earthquakes exhibit similar source properties as their shallow counterparts, yet high pressures and temperatures at great depths

preclude brittle failure as a possible causal mechanism. Therefore, deep and shallow earthquakes are likely governed by distinct physical mechanisms. Three mechanisms are commonly invoked to explain the occurrence of deep earthquakes: 1) transformational faulting of metastable olivine (Green & Burnley, 1989; Kirby, 1987; Kirby et al., 1996), 2) thermal runaway (Kanamori et al., 1998; Karato et al., 2001; Ogawa, 1987; Prieto et al., 2013), and 3) dehydration embrittlement (Meade & Jeanloz, 1991; Raleigh & Paterson, 1965). A combination of two individual mechanisms, the dual-mechanism hypothesis, has also been invoked to explain the highly variable observations of deep earthquakes (e.g., Houston, 2015; McGuire et al., 1997; Wiens & McGuire, 1995; Zhan, 2019).

Earthquake rupture properties (e.g., rupture velocity, rupture duration, rupture length, fault plane orientation) offer critical insights into the physical mechanisms controlling deep earthquakes. Geologic structure and fault plane information (e.g., location, size, and orientation) are not well constrained at depth and deep earthquakes frequently exhibit low aftershock productivity that reveals little about the ruptured fault system (Frohlich, 2006). Source modeling methods that require such constraints are often limited in their ability to resolve the rupture processes of deep events. In contrast, the back-projection method requires no a priori knowledge of the ruptured fault geometry nor the earthquake rupture velocity, proving instrumental in imaging the spatiotemporal evolution of both shallow and deep earthquakes (e.g., Ishii et al., 2005; Kiser et al., 2011; Kiser & Ishii, 2017; Krüger & Ohrnberger, 2005; Meng et al., 2014).

In this study, we determine the rupture evolution of $19 \text{ Mw} > 6$ deep-focus earthquakes occurring within the Izu-Bonin subduction zone (Figure C1) using a modified back-projection method and regional seismic data recorded at the High Sensitivity Seismograph Network (Hi-net: Obara et al., 2005; Okada et al., 2004) in Japan. The events and stations are deliberately chosen

such that the final source models are well-resolved in three spatial dimensions and time. Conventional back-projection techniques that use teleseismic P waves to resolve lateral rupture propagation typically fail to image depth-dependent variations in the earthquake rupture process. The use of direct seismic phases recorded by regional seismic arrays improves theoretical resolution both by providing a larger relative array aperture with respect to the source and resolving the source process with respect to depth. Refinements to the travel time calculations required by the back-projection method that use local three-dimensional velocity models (e.g., EARA2014: Chen et al., 2015) instead of globally-averaged one-dimensional velocity models (e.g., IASP91: Kennett & Engdahl, 1991) further improve the spatiotemporal resolution of the final source model. Whereas conventional back-projection studies of deep-focus earthquakes image the detailed rupture processes of only the largest events ($M_w > 7$; e.g., Kiser et al., 2021; Meng et al., 2014), our modified back-projection approach consistently resolves the rupture process of smaller magnitude (M_w 6–7) events, thereby increasing the number of potential source observations across our study region. We further maximize the number of source observations by targeting deep-focus earthquakes near Izu-Bonin where the depth distribution of seismicity deviates from the global average with a marked increase in deep-focus seismicity between approximately 300–550 km depth (Figure C1b). Deep-focus earthquakes near Izu-Bonin are therefore 1) abundant, 2) near high-quality seismic stations (Hi-net), and 3) occur within an existing three-dimensional velocity model (EARA2014), providing an unparalleled view of the rupture processes of deep-focus earthquakes in this region and direct observational constraints on the physical mechanisms controlling earthquakes at great depths.

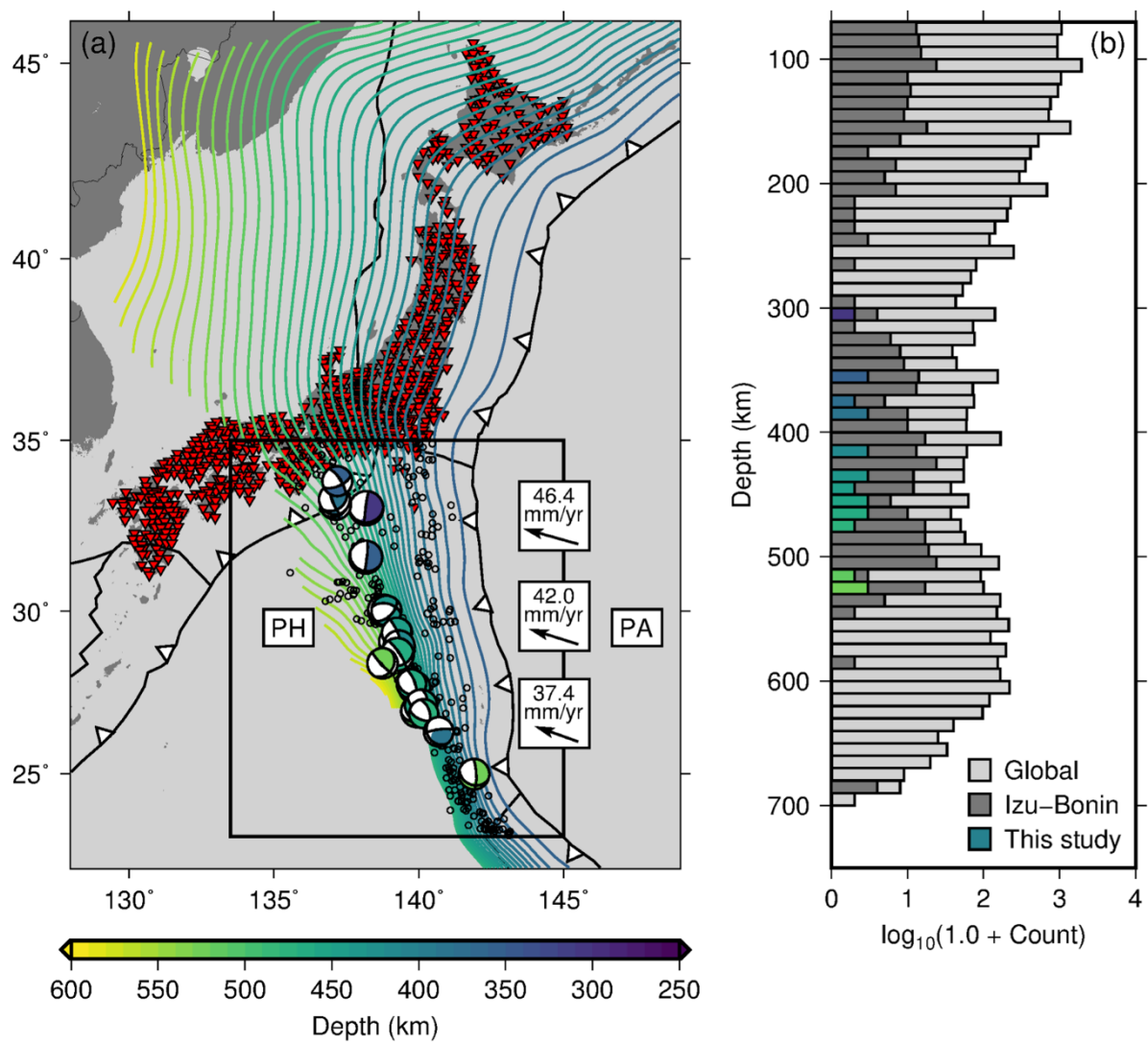


Figure C1. Overview of the study area. (a) Geographic map of the study region where the colored Global Centroid Moment Tensor (GCMT: Dziewonski et al., 1981; Ekström et al., 2012) solutions show the locations of the mainshock events imaged in this study. The red triangles show the locations of Hi-net stations. The colored contours show the subducting slabs near Japan (Slab2: Hayes et al., 2018). The magnitude-scaled black open circles show seismicity with magnitude greater than 5 and depth greater than 70 km between the years 2000–2020 as cataloged by the International Seismological Centre (ISC: Bondár & Storchak,

2011). The black arrows show the Pacific Plate motions relative to the Philippines Sea Plate (DeMets et al., 2010). The Pacific and Philippine Sea Plates are labeled PA and PH, respectively. (b) Histograms showing the depth dependence of global seismicity from the ISC (light gray), Izu-Bonin seismicity from the ISC (dark gray), and the mainshock events imaged in this study (colored according to depth), binned in 10 km increments.

2. Data

Regional seismic data for the back-projection analyses described in Sections 3.1.–3.5. are recorded at Hi-net stations and retrieved from the National Research Institute for Earth Science and Disaster Resilience in Japan (<https://doi.org/10.17598/NIED.0003>). All Hi-net data used in back-projection analyses are band-pass filtered between 0.5 and 2 Hz.

Teleseismic data for the earthquake rupture validation procedure described in Section 3.7. are combined under the GSN virtual network “_GSN” (http://ds.iris.edu/mda/_GSN/) and retrieved from the Incorporated Research Institutions for Seismology (IRIS) Data Management Center. All GSN data used in back-projection analyses are band-pass filtered between 0.8 and 2 Hz.

3. Methods

3.1. Conventional back-projection method

Regional seismic data recorded at Hi-net stations in Japan (0° – 21° hypocentral distance) are analyzed with the back-projection method (Ishii et al., 2005), which time shifts and stacks seismic array data to a grid of potential source locations to image the spatiotemporal evolution of

energy release during an earthquake. The large relative aperture of the regional station distribution offers adequate spatiotemporal resolution to a volume of grid points surrounding each earthquake, which allows the source process of each earthquake to be constrained in three spatial dimensions and time. The dimensions of the back-projection grid volumes for each earthquake are outlined in Table CS1. The grid dimensions are chosen such that the complete earthquake rupture processes are captured within the volumes and grid spacings are used that image spatiotemporal rupture complexities without exceeding computer hardware limits.

Travel times from each grid point to each Hi-net station are calculated using the three-dimensional velocity model EARA2014 (Chen et al., 2015) and the fast marching method (de Kool et al., 2006). A cross-correlation procedure (Ishii et al., 2007) aligns first-arriving P waves from a smaller magnitude reference event near each mainshock hypocenter (subsequently called alignment events) to correct for heterogeneous earth structure between the source and stations that is not accounted for in the three-dimensional velocity model. This step additionally normalizes P wave amplitudes and corrects waveform polarities with respect to a reference stack of waveforms. One alignment event can often be used for multiple nearby mainshock back-projection analyses on the condition that the events have similar hypocenters and moment-tensor solutions. The alignment events used for each mainshock back-projection analysis are shown in Table CS2.

Following the alignment procedure, the same empirical travel time corrections are applied to the appropriate nearby mainshock events and these time-shifted waveforms are stacked at each grid point. Grid points with high amplitudes indicate the source locations of radiated seismic energy and the spatiotemporal evolution of these sources allow one to measure

earthquake rupture properties (i.e., rupture speed and direction) and identify rupture complexity (i.e., fault segmentation) without a priori information of these parameters.

3.2. Genetic algorithm-based station selection method

Back-projection studies often use direct P waves to determine the spatiotemporal evolution of an earthquake rupture, and thus assume only direct P waves are present in the waveforms being used in each analysis. This assumption deteriorates at the regional distance windows presented in this study and the presence of any high amplitude phases other than the direct P wave results in incoherent data that causes severe artifacts in the back-projection results, ultimately obscuring the real earthquake rupture processes.

To mitigate this problem, we systematically remove incoherent data causing artifacts in the back-projection results using a genetic algorithm-based station selection method (Kehoe et al., 2019; Kehoe & Kiser, 2020). This method uses Hi-net data from a second smaller magnitude reference event near each mainshock hypocenter (subsequently called station selection events) to find a subset of stations that image the station selection event as a point source. This approach assumes that small events should be imaged by the back-projection method as point sources, and any additional imaged energy is likely the result of artifacts in the back-projection result. For each station selection event, we produce back-projection images using a suite of candidate station distributions and use a fitness function to evaluate how well each station distribution images the station selection event as a point source. This process is performed iteratively until a near-optimal station distribution is obtained for each station selection event. The same near-optimal station distribution is then applied to the appropriate mainshock events.

The optimized station distribution determined using the station selection event inherently depends on the empirical travel time corrections calculated using the alignment event. Thus, station selection and alignment events will always be paired and updated in tandem as we investigate mainshock events across the study region. Nonetheless, the same optimized station distributions and empirical travel time corrections can be applied to multiple nearby mainshock back-projection analyses on the condition that all events have similar hypocenters and moment-tensor solutions. The station selection events used for each mainshock back-projection analysis are shown in Table CS3.

3.3. Image deconvolution back-projection method

We adapt the Image Deconvolution Back-Projection (IDBP) method developed by Wang et al. (2016) to our back-projection results in three spatial dimensions and time. Conventional back-projection results can be thought of as the spatiotemporal convolution of the array response and the earthquake source distribution and in many cases, the convolution of these contributions is used to infer earthquake source properties instead of the true source distribution itself. The source processes of earthquakes in our study region, and indeed the source processes of deep-focus earthquakes in general, are often compact in both space and time necessitating the removal of any artifacts obscuring the source image. The IDBP approach again uses a smaller magnitude reference event near each mainshock hypocenter (subsequently called deconvolution events) to remove features of the back-projection result caused by the array response, leaving only the discrete distribution of earthquake sources comprising the overall rupture.

To reduce potential smearing artifacts in the mainshock and deconvolution events, we first apply a coherence-based back-projection approach (Ishii, 2011) to our results using data

recorded at an optimized distribution of Hi-net stations (see Section 3.2). Synthetic point sources are used for the deconvolution events by generating synthetic seismograms consisting of 1 Hz central frequency Ricker wavelets with theoretical time-shifts calculated using the IRIS reported hypocenter. Our use of synthetic data as the deconvolution event is a departure from Wang et al. (2016) who use real seismic data recorded during a smaller magnitude reference event. We find that our implementation of the IDBP method is sensitive to the depth of the deconvolution event (Figure CS1). This approach produces more consistent results across our study area by ensuring the deconvolution event contains both minimal source complexity and a hypocenter consistent with the mainshock event.

Both this study and Wang et al. (2016) utilize a back-projection amplitude contouring scheme that only inverts back-projection grid points with amplitudes above a minimum normalized amplitude value. This step is critical both to reduce the size of the matrix being inverted and as a means of regularization that stabilizes the inversion results. We find that the optimal amplitude contour varies significantly between events and each portion of the imaged rupture process itself. An amplitude contour that is too high will fail to capture lower amplitude features of the back-projection results while an amplitude contour that is too low will yield unstable results or an inversion matrix that is too large.

The IDBP results will additionally produce low-amplitude artifacts that do not follow the first-order rupture properties of the imaged earthquake. These low-amplitude artifacts may result from additional imaged energy in the mainshock back-projection result that is not represented in the synthetically generated deconvolution events. Low-amplitude artifacts may also appear near the edges of the amplitude contour and where applicable, the edges of the back-projection grid volume. Care must be taken to minimize these low-amplitude artifacts by ensuring that the back-

projection grid volume encompasses the total earthquake rupture, verifying that no high-amplitude features are imaged near the edges of the back-projection grid volume. The deconvolution event is imaged within a grid volume with the same back-projection grid spacing but twice the length in each spatiotemporal dimension as the mainshock back-projection grid volume to eliminate any potential IDBP artifacts resulting from image deconvolution at artificial amplitude discontinuities (e.g., from padding zero amplitudes around the deconvolution event). The dimensions of the back-projection grid volumes for each deconvolution event are outlined in Table CS1. An IDBP amplitude cutoff value is implemented to eliminate low-amplitude IDBP artifacts in the final results, aiding the interpretation of the first-order rupture properties of the earthquakes presented in this study. The optimal IDBP amplitude cutoff value varies with each IDBP result and the relative amplitudes of the resolved IDBP radiators.

We select an optimal amplitude contour and IDBP amplitude cutoff by applying the IDBP method at all back-projection amplitude contours γ and IDBP amplitude cutoffs κ between 5% and 95% normalized amplitude in 5% increments, and selecting the γ and κ values that minimize the following objective function:

$$f(\gamma, \kappa) = \frac{\sum_{i=1}^{N_{IDBP}(\gamma, \kappa)} \Delta_{IDBP}^i(\gamma, \kappa)}{\Delta_{max}}$$

subject to the constraints:

$$t_R(\gamma, \kappa) > t_{R,\min}$$

$$l_R(\gamma, \kappa) > l_{R,\min}$$

$$G(\gamma) > G_{\min}$$

where N_{IDBP} is the number of recovered IDBP radiators, Δ_{IDBP}^i is the distance from the i th IDBP radiator to the center of the back-projection volume, and Δ_{max} is the distance from the furthest back-projection grid point to the center of the back-projection grid volume. The calculated

rupture duration t_R must be larger than the minimum rupture duration $t_{R,\min}$ with a value equal to twice the back-projection time-step. The calculated rupture length l_R must be larger than the minimum rupture length $l_{R,\min}$ with a value equal to twice the distance between two orthogonally adjacent back-projection grid points (ignoring diagonally adjacent grid points). The number of back-projection grid points G above the amplitude contour γ must be larger than the minimum number of back-projection grid points G_{\min} with a value equal to 5,000. Amplitude contours and IDBP amplitude cutoffs that do not satisfy these constraints may incompletely characterize the entire earthquake source process and therefore inhibit the recovery of the true source distribution.

3.4. Average rupture velocity vector

Following the determination of the discrete earthquake source distribution with IDBP, a single average rupture velocity vector is reported for each earthquake that summarizes the first-order characteristics of each back-projection result, facilitates the comparison of earthquake rupture properties across the study region (Figures C3–C4), and in some cases, allows the fault plane to be determined (see Section 3.5.). All possible rupture paths that connect the individual IDBP radiators at positive rupture velocities less than the local P wave speed v_P are first measured and subsequently called the candidate rupture velocity vectors. These constraints remove nonphysical ruptures that occur at or in excess of the local P wave speed as well as ruptures proceeding in negative time. The average rupture velocity vector \vec{v}_R is the weighted average of the candidate rupture velocity vectors, calculated using the measured IDBP amplitudes as weights:

$$\vec{\bar{v}}_R = \frac{\sum_{j=1}^L A_{IDBP}^j \vec{v}_{CR}^j}{\sum_{j=1}^L A_{IDBP}^j}$$

subject to the constraints:

$$0 \text{ km/s} < \vec{v}_{CR}^j < v_P$$

where L is the number of candidate rupture velocity vectors, A_{IDBP}^j is the averaged IDBP amplitudes of the two IDBP radiators connected by the j th candidate rupture velocity vector \vec{v}_{CR}^j .

3.5. Nodal plane classification

Constraints on earthquake rupture processes in three spatial dimensions can reveal fault plane orientations (e.g., Warren et al., 2007). Our procedure first estimates the best- and worst-fitting GCMT nodal planes (NP_1 and NP_2 , respectively) by plotting the nodal planes at each discrete IDBP source location, summing the minimum distance between every source location and a given nodal plane (subsequently called the summed misfit), then finding the source location and nodal plane combination that minimizes the summed misfit of the candidate plane and each IDBP source location. The angle θ_1 is measured between the average rupture velocity vector and the best-fitting nodal plane NP_1 and the angle θ_2 is measured between the average rupture velocity vector and the worst-fitting nodal plane NP_2 . The nodal plane pairs are classified according to the criteria in Table.

| Classification | Criteria |
|---|--|
| Rupture on a single fault plane (NP_1) | 1. $\theta_2 - \theta_1 > 10^\circ$ 2. $\frac{\theta_1}{\theta_2} \leq 0.5$ |
| Rupture on both nodal planes (NP_1, NP_2) | 3. $\theta_2 - \theta_1 \leq 10^\circ$ 4. $\frac{\theta_1}{\theta_2} \leq 0.5$ |
| Rupture on neither nodal plane | 5. All remaining combinations of $\theta_2 - \theta_1$ and $\frac{\theta_1}{\theta_2}$ |

Table C1. Nodal plane classification criteria.

Large values of $\theta_2 - \theta_1$ and small values of $\frac{\theta_1}{\theta_2}$ (Criteria 1 and 2) ensure that the rupture vector uniquely lies on NP_1 but not on NP_2 . Small values of $\theta_2 - \theta_1$ and $\frac{\theta_1}{\theta_2}$ (Criteria 3 and 4) ensure that the rupture vector lies at the intersection of NP_1 and NP_2 . All remaining combinations of $\theta_2 - \theta_1$ and $\frac{\theta_1}{\theta_2}$ (i.e., those containing large values of $\frac{\theta_1}{\theta_2}$) describe a rupture vector that is oblique to NP_1 and NP_2 . Note that for values of $\frac{\theta_1}{\theta_2} > 1$ or $\theta_2 - \theta_1 < 0^\circ$, the rupture vector lies further away from the best-fitting nodal plane NP_1 than the worst-fitting nodal plane NP_2 , which we disallow and subsequently classify the rupture as occurring on neither nodal plane. The planes classified by this procedure are shown in Figures C3–C4.

3.6. Estimation of the back-projection smearing artifact

The smearing artifact, resulting from imperfect data coverage, manifests as a high-amplitude feature along the ray path and at the speed of the seismic phase used in the back-projection analysis (Kiser & Ishii, 2017). In this study, the smearing artifact appears as high back-projection amplitudes that move towards the Hi-net array along the P wave ray path at the local P wave speed. The absence of mitigating techniques such as the genetic algorithm-based station selection method or the IDBP method may result in smearing artifacts that obscure the true earthquake rupture process. The smearing direction and speed (subsequently called the average smearing vector) of each mainshock event are estimated using the deconvolution event generated with synthetic data. A discrete source distribution is generated by tracking the mean-amplitude location at each time step of the synthetically generated deconvolution event. The

average smearing vector is estimated using the same technique that estimates the average rupture vector of the IDBP source distribution (see Section 3.4.) with the noted exception that candidate rupture velocity vectors at and greater than the local P wave speed are allowed. The distribution of average smearing vectors is shown with the distribution of average rupture vectors in Figure CS2.

3.7. Earthquake rupture validation with teleseismic data

Our regional IDBP results are validated using a conventional teleseismic (30° – 95°) back-projection analysis of each earthquake presented in this study. The genetic algorithm-based station selection method is not used for this portion of the study and instead, all available Global Seismographic Network (GSN) data within the teleseismic distance window are used. Travel times from each grid point to each GSN station are calculated using the one-dimensional velocity model IASP91 (Kennett & Engdahl, 1991). The same cross-correlation procedure (Ishii et al., 2007) aligns first-arriving P waves from the mainshock event itself to correct for heterogeneous earth structure between the source and stations while simultaneously ensuring P wave amplitudes are normalized and waveform polarities are corrected with respect to a reference stack of waveforms. We use a coherence-based back-projection approach (Ishii, 2011) to image each earthquake rupture process. The rupture direction and speed of each mainshock event is determined using the same technique that estimates the average rupture vector of the IDBP source distribution (see Section 3.4) and the average smearing vector of the synthetically generated deconvolution event (see Section 3.6).

3.8. Summary of Methods

Our implementation of the back-projection method as described throughout Section 3 is summarized in Figure C2.

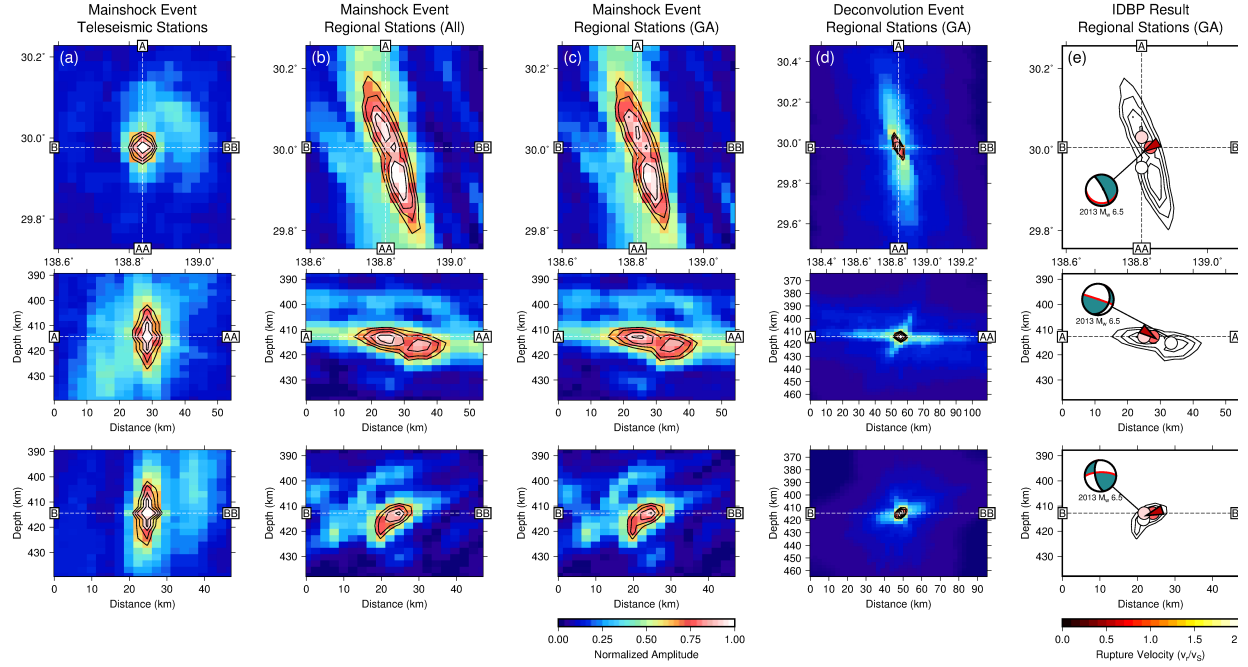


Figure C2. Summary of the back-projection method using the 2013 Mw 6.5 mainshock event as an example. (a) The conventional back-projection result of the mainshock event using a teleseismic distribution of 54 GSN stations (Section 3.7). (b) The conventional back-projection result of the mainshock event using a regional distribution of 639 Hi-net stations (Section 3.1). (c) The back-projection result using the genetic algorithm (GA) optimized station distribution consisting of 336 Hi-net stations (Section 3.2). (d) The synthetic back-projection result using the GA optimized station distribution which is subsequently used as the deconvolution event of the IDBP method (Section 3.3). Note the increased back-projection grid volume by the IDBP method. (e) The IDBP result where the colored circles are the discrete IDBP source distribution (Section 3.3), the colored arrows are the average rupture velocity vector (Section 3.4), and the red GCMT plane is the classified fault plane (Section 3.5).

4. Results

4.1. Regional back-projection results

The regional back-projection analysis is applied to 19 deep-focus earthquakes near Izu-Bonin and the event and rupture properties are summarized in Tables C2–C4 and Figures C3–C4. The imaged mainshock events occurred between October 2000 and November 2022, have moment magnitudes between 6.0 and 7.1, and hypocentral depths between 300 and 530 km. Origin times and hypocenters are obtained from the IRIS catalog. Nodal plane strikes, dips, and rakes are obtained from the GCMT catalog. Moment magnitudes are calculated using the GCMT reported moments and the scaling relationship of Hanks & Kanamori (1979).

Myhill & Warren (2012) use a rupture directivity analysis to determine the trend and plunge of deep earthquake ruptures near Izu-Bonin-Marianas while we use the back-projection method to constrain an average rupture velocity vector for deep-focus events near Izu-Bonin. While the methodologies, seismic arrays, and data periods between the two studies vary significantly, some similarity in 5 overlapping events is observed. All but one overlapping event, the anomalously shallow 302.2-km deep Mw 7.1 event, rupture at relatively shallow angles from horizontal ($\pm \sim 40^\circ$). Rupture trends reported by the two studies differ more drastically, and no dependence of rupture trend on moment is observed in the overlapping events cataloged by Myhill & Warren (2012).

| Event ID | Origin Time | Mw (GCMT) | Latitude (°N) | Longitude (°E) | Depth (km) |
|----------|---------------------|-----------|---------------|----------------|------------|
| 1 | 2000-10-27 04:21:53 | 6.1 | 26.26 | 140.56 | 412.3 |
| 2 | 2002-08-02 23:11:38 | 6.2 | 29.19 | 139.12 | 425.4 |
| 3 | 2003-11-12 08:26:43 | 6.4 | 33.24 | 137.05 | 381.8 |
| 4 | 2009-08-09 10:55:56 | 7.1 | 33.15 | 138.06 | 302.2 |

| | | | | | |
|----|---------------------|-----|-------|--------|-------|
| 5 | 2010-11-30 03:24:41 | 6.8 | 28.39 | 139.24 | 485.0 |
| 6 | 2011-01-12 21:32:54 | 6.5 | 26.97 | 140.02 | 524.5 |
| 7 | 2012-01-01 05:27:55 | 6.8 | 31.47 | 138.18 | 359.7 |
| 8 | 2012-05-26 21:48:09 | 6.0 | 26.90 | 140.17 | 481.6 |
| 9 | 2013-04-21 03:22:16 | 6.1 | 29.96 | 138.97 | 431.3 |
| 10 | 2013-09-04 00:18:24 | 6.5 | 29.98 | 138.84 | 414.4 |
| 11 | 2014-06-30 19:55:33 | 6.3 | 28.39 | 138.87 | 527.4 |
| 12 | 2015-06-23 12:18:30 | 6.5 | 27.69 | 139.79 | 472.3 |
| 13 | 2016-08-04 16:24:33 | 6.3 | 24.94 | 142.01 | 510.0 |
| 14 | 2017-09-07 17:26:49 | 6.1 | 27.78 | 139.80 | 451.0 |
| 15 | 2019-06-04 04:39:17 | 6.4 | 29.06 | 139.29 | 430.3 |
| 16 | 2019-07-27 18:31:07 | 6.4 | 33.15 | 137.33 | 367.0 |
| 17 | 2020-04-18 08:25:37 | 6.6 | 27.13 | 140.13 | 453.0 |
| 18 | 2022-11-14 08:08:26 | 6.2 | 33.80 | 137.25 | 357.4 |
| 19 | 2023-01-16 04:49:52 | 6.4 | 28.99 | 139.36 | 405.0 |

Table C2. Reported mainshock event properties.

| Event ID | Origin Time | Vr (km/s) | Vr/Vs | Rupture Trend (°) | Rupture Plunge (°) | Rupture Duration (s) | Rupture Length (km) |
|----------|---------------------|-----------|-------|-------------------|--------------------|----------------------|---------------------|
| 1 | 2000-10-27 04:21:53 | 7.0 | 1.44 | 347 | -25 | 3.4 | 23.7 |
| 2 | 2002-08-02 23:11:38 | 2.4 | 0.47 | 292 | 38 | 4.0 | 10.6 |
| 3 | 2003-11-12 08:26:43 | 4.4 | 0.91 | 342 | 20 | 3.4 | 14.9 |
| 4 | 2009-08-09 10:55:56 | 2.7 | 0.58 | 122 | 64 | 5.4 | 14.6 |
| 5 | 2010-11-30 03:24:41 | 9.2 | 1.77 | 311 | 26 | 6.2 | 57.3 |
| 6 | 2011-01-12 21:32:54 | 2.9 | 0.55 | 105 | -13 | 4.6 | 11.7 |
| 7 | 2012-01-01 05:27:55 | 5.3 | 1.10 | 0 | 26 | 2.2 | 11.6 |
| 8 | 2012-05-26 21:48:09 | 2.7 | 0.51 | 336 | -70 | 2.8 | 13.8 |
| 9 | 2013-04-21 03:22:16 | 5.8 | 1.13 | 131 | -21 | 2.4 | 13.9 |
| 10 | 2013-09-04 00:18:24 | 2.8 | 0.58 | 239 | -23 | 2.2 | 8.2 |
| 11 | 2014-06-30 19:55:33 | 1.1 | 0.21 | 180 | -63 | 5.0 | 5.6 |
| 12 | 2015-06-23 12:18:30 | 1.9 | 0.37 | 20 | 20 | 9.2 | 17.7 |
| 13 | 2016-08-04 16:24:33 | 2.4 | 0.45 | 318 | -19 | 6.4 | 15.3 |
| 14 | 2017-09-07 17:26:49 | 5.2 | 1.00 | 318 | 54 | 1.2 | 6.2 |
| 15 | 2019-06-04 04:39:17 | 2.2 | 0.43 | 180 | 71 | 3.6 | 7.9 |
| 16 | 2019-07-27 18:31:07 | 1.6 | 0.34 | 337 | 52 | 6.0 | 9.5 |
| 17 | 2020-04-18 08:25:37 | 3.4 | 0.66 | 74 | 35 | 3.8 | 13.0 |
| 18 | 2022-11-14 08:08:26 | 2.9 | 0.61 | 157 | -23 | 2.2 | 6.4 |
| 19 | 2023-01-16 04:49:52 | 2.88 | 0.57 | 163 | 4 | 5.0 | 14.2 |

Table C3. Mainshock rupture properties determined by the regional back-projection analysis.

| Event ID | Origin Time | Classification | Shallower Plane | Steeper Plane |
|----------|---------------------|----------------|-----------------|---------------|
| 1 | 2000-10-27 04:21:53 | Neither | 142/24/148 | 262/78/70 |
| 2 | 2002-08-02 23:11:38 | Neither | 73/25/-168 | 332/85/-65 |

| | | | | |
|----|---------------------|---------------|--------------------|-------------------|
| 3 | 2003-11-12 08:26:43 | <i>Both</i> | <i>50/34/156</i> | <i>160/77/59</i> |
| 4 | 2009-08-09 10:55:56 | Single | 86/17/168 | 187/86/73 |
| 5 | 2010-11-30 03:24:41 | Single | 76/31/-157 | 326/78/-61 |
| 6 | 2011-01-12 21:32:54 | Single | 84/31/-147 | 325/74/-63 |
| 7 | 2012-01-01 05:27:55 | <i>Both</i> | <i>114/18/-161</i> | <i>6/84/-73</i> |
| 8 | 2012-05-26 21:48:09 | Neither | 107/53/-134 | 346/55/-47 |
| 9 | 2013-04-21 03:22:16 | Neither | 282/51/-46 | 45/56/-130 |
| 10 | 2013-09-04 00:18:24 | Single | 95/19/-146 | 333/80/-74 |
| 11 | 2014-06-30 19:55:33 | Single | 31/27/163 | 137/82/64 |
| 12 | 2015-06-23 12:18:30 | Single | 107/38/-141 | 345/67/-59 |
| 13 | 2016-08-04 16:24:33 | Neither | 110/30/-155 | 357/78/-63 |
| 14 | 2017-09-07 17:26:49 | Single | 111/29/-136 | 341/70/-68 |
| 15 | 2019-06-04 04:39:17 | Single | 87/13/-171 | 349/88/-77 |
| 16 | 2019-07-27 18:31:07 | Neither | 48/27/153 | 162/78/65 |
| 17 | 2020-04-18 08:25:37 | Single | 125/53/-133 | 3/55/-48 |
| 18 | 2022-11-14 08:08:26 | Single | 66/63/-159 | 326/72/-29 |
| 19 | 2023-01-16 04:49:52 | Neither | 123/19/-137 | 351/77/-76 |

Table C4. Nodal plane classifications. Bold values indicate rupture on a single fault plane, italic values indicate rupture on both fault planes (i.e., rupture near the intersection of both nodal planes), plain values indicate rupture on neither fault plane.

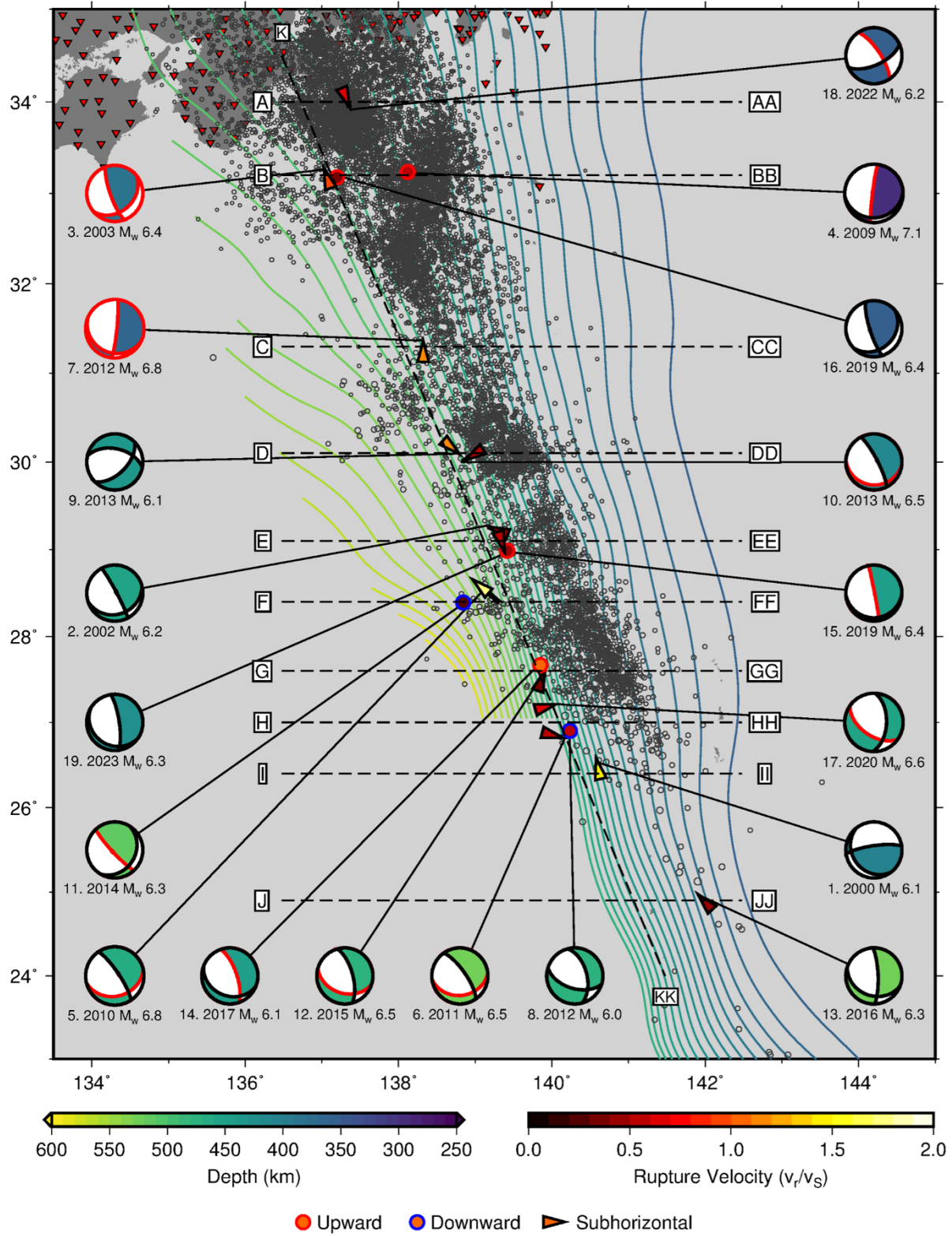


Figure C3. Map summarizing the regional back-projection results. The red triangles show the locations of Hi-net stations. The depth-colored contours show the subducting slabs (Slab2: Hayes et al., 2018). The magnitude-scaled black open circles show all Japan Meteorological Agency (JMA: https://www.data.jma.go.jp/svd/eqev/data/bulletin/hypo_e.html) catalogued seismicity with depths greater than 250 km between the years 2000–2020. The colored arrows and circles show the rupture speed and direction as determined by the regional back-projection analysis. Arrows are used for subhorizontal ruptures ($\leq 45^\circ$) while circles are used for subvertical ruptures ($> 45^\circ$). The arrows and circles are colored by their rupture velocity, normalized to the local shear wave speed at the observed rupture depth. Upward propagating ruptures are outlined in red, downward propagating ruptures are outlined in blue, and subhorizontally propagating ruptures are outlined in black. The depth-colored GCMT solutions associated with each event are plotted at the edges of the figure for clarity. Nodal planes of the GCMT solutions are colored according to the nodal plane classification scheme. A single red nodal plane indicates rupture on that single fault plane, two red nodal planes indicate rupture on both nodal planes, and two black nodal planes indicate rupture on neither nodal plane. The labeled dashed lines show the locations of the 11 cross-sections shown in Figure C4.

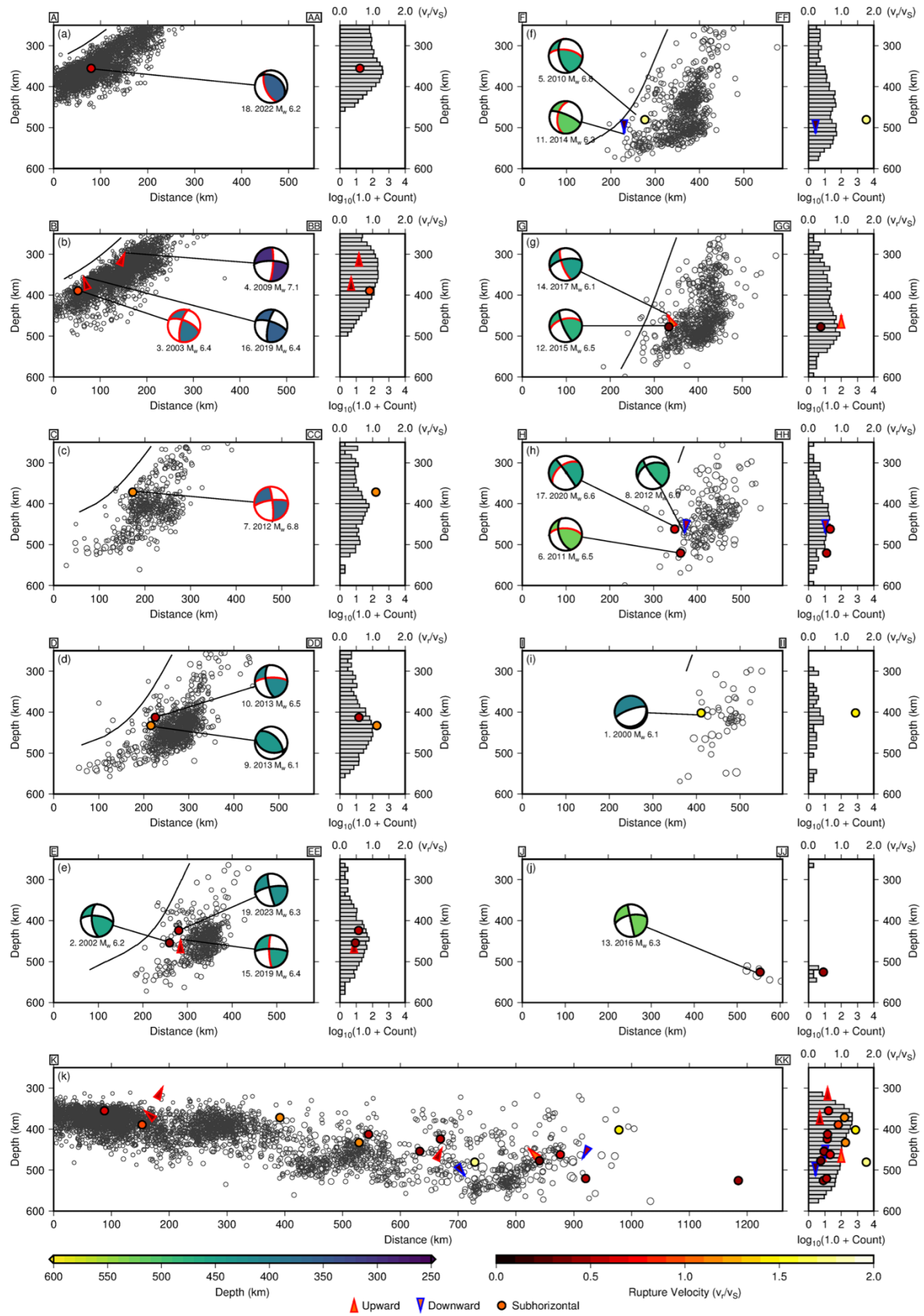


Figure C4. Cross-sections associated with the dashed lines in Figure C3. (a–k) Within each geographic cross-section plot (left of each subpanel), a black line showing the slab, magnitude-scaled black open circles showing JMA seismicity, colored GCMT solutions, and colored rupture vectors are projected onto the vertical plane of each cross-section. Nodal planes of the GCMT solutions are colored according to the nodal plane classification scheme. A single red nodal plane indicates rupture on that single fault plane, two red nodal planes indicate rupture on both nodal planes, and two black nodal planes indicate rupture on neither nodal plane. A histogram (right of each subpanel) shows the depth dependence of JMA seismicity within 50 km of the cross-section. Rupture velocities associated with the mainshock events of each cross-section are plotted on top of the JMA background seismicity histogram. Upward propagating ruptures are shown as arrows outlined in red, downward propagating ruptures are shown as arrows outlined in blue, and subhorizontally propagating ruptures are shown as circles outlined in black.

4.2. Teleseismic back-projection results

A conventional teleseismic back-projection analysis is performed for all mainshock events presented in this study to validate the rupture processes determined by the regional back-projection analysis. Teleseismic back-projection analyses do not resolve depth-dependent rupture properties and we instead focus on the lateral rupture extent of events imaged with the teleseismic back-projection method. Rupture speeds and directions are determined for 5 of the 19 events within our study region and are summarized in Figure CS3 and Table CS4. While the teleseismic back-projection method cannot constrain the vertical component of rupture velocity and therefore underestimates rupture speeds, rupture trends of the 5 imaged events are observed

within 60° of the values determined by the regional back-projection method. The remaining events are imaged as spatiotemporal point sources, possibly due to steeply plunging or short ruptures that inhibit the identification of finite rupture processes on the horizontal back-projection grid surrounding each earthquake. While data recorded at teleseismic distance windows are routinely used to image large ruptures, the determination of moderate moment source properties in three spatial dimensions requires data recorded at regional distances. The teleseismic back-projection results presented in this study are therefore used only to verify the regional back-projection results presented in Section 4.1.

5. Discussion

5.1. Moment-length scaling, b values, and fractal dimension

The scaling of the seismic moment M_0 with the characteristic fault length has been studied extensively for both shallow (Pacheco et al., 1992; Romanowicz & Rundle, 1993; Scholz, 1982, 1997) and deep (e.g., Okal & Kirby, 1995; Todes et al., 2021; Zhan, 2017) earthquakes. These studies focus on whether the average slip S scales with fault width W , fault length L , or both. Following the definition of seismic moment M_0 :

$$M_0 = \mu SWL$$

where μ is the shear modulus, these three scenarios can be summarized as:

$$M_0 \propto L^n; n = 1, 2, 3$$

where the parameter n describes the scaling relationship. For earthquakes occurring in finite seismogenic zones, the fault dimensions may physically saturate as the earthquake grows, with the smaller dimension W saturating before the larger dimension L . If average slip S scales only

with width W (thus, independent of L) and after width saturation S remains independent of fault length L , we expect $M_0 \propto L$ (W-model). If instead average slip S scales with fault length L and after width saturation S still scales with L , we expect $M_0 \propto L^2$ (L-model). If average slip S scales with both L and W and width never saturates, either because the earthquake is sufficiently small or because the seismogenic zone is sufficiently large, we expect $M_0 \propto L^3$.

The moment-length scaling relationship is intrinsically related to the statistical distribution of earthquakes in a region. The Gutenberg-Richter (G-R) law identifies the number of earthquakes N above a given magnitude (Gutenberg & Richter, 1944)

$$N(M_w) = 10^{a-bM_w}$$

where M_w is the moment magnitude and a and b are constants. The G-R b value is the slope of the frequency-magnitude distribution which describes the relative number of small and large earthquakes in a given dataset. Measured b values of deep earthquakes vary across subduction zones and previous studies have investigated the influence of slab thermal state and earthquake magnitude on observed b values to understand the underlying physical mechanisms of deep earthquakes (Mao et al., 2022; Okal & Kirby, 1995; Todes et al., 2021; Wiens & Gilbert, 1996; Zhan, 2017). From the definition of moment magnitude (Hanks & Kanamori, 1979; Kanamori, 1977):

$$M_w = \frac{2}{3}(\log_{10} M_0 - 9.1)$$

where M_0 is measured in units of Nm, the G-R law may be rewritten to find the number of earthquakes above a given moment $N(M_0)$:

$$N(M_0) \propto M_0^{-\frac{2}{3}b}$$

From the moment-length scaling relationship, the G-R law may be rewritten to find the number of earthquakes above a given characteristic fault length $N(L)$:

$$N(L) \propto L^{-\frac{2}{3}nb}$$

This is the exact mathematical form of the definition of a fractal distribution (Mandelbrot, 1977, 1983):

$$N(r) \propto r^{-D}$$

where r is a characteristic linear dimension, $N(r)$ is the number of objects with a characteristic linear dimension greater than r , and D is the fractal dimension which describes the distribution of small and large objects in a set, or the roughness of a set.

While Gutenberg & Richter (1944) lacked the framework of fractal geometry pioneered by Mandelbrot (1977) whilst formulating their empirical relationship between earthquake magnitude and frequency, (Aki, 1981) tied the power-law scaling of the G-R law to the fractal-like behavior of seismicity on natural faults, formulating the fractal dimension D in terms of the G-R law b value:

$$D = \frac{2}{3}nb$$

The fractal dimension D differs explicitly from the familiar Euclidean dimension (where points, lines, planes, and volumes are zero-, one-, two-, and three-dimensional, respectively) and in fact, a fractal set is defined by Mandelbrot (1977) as having a fractal dimension strictly larger than the Euclidean dimension. The fractal dimension, which is not necessarily a whole number, is a useful index for characterizing the roughness or space-filling capacity of a set as a single value. The famous example arising from the empirical measurement of coastlines with increasingly shorter measuring sticks yields a fractal dimension of the western coast of Britain to be ~ 1.25 (Mandelbrot, 1967). Natural coastlines are topologically one-dimensional, but have measured

fractal dimensions between one and two. A perfectly straight coastline would have a fractal dimension of one while a space-filling coastline would have a fractal dimension of two. Likewise, the surface of a perfectly flat sea would have a fractal dimension of two, a stormy sea would have a fractal dimension between two and three, and a space-filling sea would have a fractal dimension of three.

While shallow earthquakes are understood to fill two-dimensional fault planes, the fault dimensions of deep earthquakes are not well understood, and linear, planar, and volumetric faulting regions have been used to explain various observations of b values (e.g., Okal & Kirby, 1995; Todes et al., 2021; Zhan, 2017). The fractal dimension D and moment-length scaling parameter n may reveal the geometry of deep faults, thus clarifying the physical mechanism governing deep-focus earthquakes. However, the two parameters are poorly constrained at great depths and various combinations of D and n can explain the same observed b value. Discontinuities in b value with moment indicate a departure from self-similarity, possibly due to changes in fault geometry, causal mechanism, or both. We will first discuss existing models established on the relationships between these three parameters before introducing new observations from our regional back-projection analyses that build upon these concepts.

Due to the small number of large deep-focus earthquakes, Zhan (2017) combines data of the deepest earthquakes (500–700 km depth) occurring in warm (i.e., low thermal parameter) subduction zones (including Izu-Bonin) and observes b values of 0.5 below Mw 6.5 and b values of 1.0 above Mw 6.5. This break in self-similarity is attributed to the presence of two distinct physical mechanisms operating above and below a critical moment in deep portions of warm slabs. Zhan (2017) argues that at intermediate moments (Mw ~5.3–6.5), deep earthquakes within warm slabs are largely limited to rupture along thin, discontinuous segments of the metastable

olivine wedge (MOW) via transformational faulting which may be complemented by passive rupture outside the MOW by a thermally controlled mechanism to accommodate the measured moment release. In this case, the faulting region is strictly controlled by the thin, discontinuous MOW segment ($D = 1$) with no width saturation ($n = 3$), explaining the observed b values of 0.5. Zhan (2017) further proposes that at large moments ($Mw > 6.5$), earthquake rupture is actively driven outside of the MOW via thermal runaway and the characteristic rupture length is no longer controlled by a thin, discontinuous MOW segment but along a plane of rupture outside of the MOW ($D = 2$) with no width saturation ($n = 3$), explaining the observed b values of 1.0. Within the coldest slabs with the thickest MOW (i.e., the Tonga subduction zone), earthquakes nucleate and rupture within the MOW via transformational faulting and can only passively propagate outside of the MOW during exceptionally large earthquakes where the rupture length exceeds the MOW thickness. Hence, the faulting region is rarely restricted by the MOW thickness and rupture primarily occurs along planar faults within the MOW ($D = 2$) with no width saturation ($n = 3$), explaining the observed b values of 1.0 across all observable moments.

Mao et al. (2022) find a similar discontinuity in observed b values of deep-focus earthquakes (300–700 km depth) in warm subduction zones (including Izu-Bonin) using the GCMT and IRIS catalogs, which are summarized along with the results of Zhan (2017) in Table C5. While Mao et al. (2022) combine data from the same distribution of warm subduction zones as Zhan (2017), they additionally incorporate data from shallower depths (300–500 km) and attribute the larger moment at which the b value discontinuity is observed to a thicker MOW at colder and shallower depths. Similarly, Zhan (2017) observes a statistically significant depth dependence of b values in the Izu-Bonin-Marianas and Japan-Kuril subduction zones, where higher b values are observed in shallower depth bins (300–700 km) than deeper depth bins (500–

700 km), likely due to the warming of the subducting slab by conduction and the resulting thinning of the MOW with increasing depth (Devaux et al., 1997; Kirby et al., 1996). While these observations emphasize the depth and temperature dependence of observed b values, they also highlight how regional variations in thermal parameter across individual subduction zones may cause deviations in observed b values. Indeed, the major findings of Mao et al. (2022) use the JMA catalog to measure b values at small to intermediate moments (Mw 3.3–5.5) of four clusters of seismicity near Japan (including Izu and Bonin, individually). While measurements at larger moments are limited due to the small number of cataloged large deep-focus earthquakes in these regions, b values near Izu ($b = 1.0$) and Bonin ($b = 0.9$) appear larger than those estimated using data combined from warm subduction zones around the world ($b = 0.5$ –0.7). Previous studies have found that deep-focus seismicity and source properties exhibit a strong dependence on the thermal state of the subducting slab (e.g., Wiens, 2001; Wiens & Gilbert, 1996) and the regional elevation of b values near Izu-Bonin implies the existence of a thicker, more prominent MOW. While the dual-mechanism hypothesis is presented by Zhan (2017) with two endmember examples (warm and cold slabs), we will discuss our back-projection results in the context of observations specific to Izu-Bonin when available, which exhibits a moderate thermal parameter (~5000–8000 km) relative to those measured globally (~500–12000 km) (Frohlich, 2006).

| Study | Catalog | Depth range | Intermediate Mw range | Intermediate b value | Large Mw range | Large b value |
|-------------------|---------|-------------|-----------------------|------------------------|----------------|-----------------|
| Zhan (2017) | GCMT | 500–700 km | Mw 5.3–6.5 | 0.5 | Mw 6.6–7.3 | 1.0 |
| Mao et al. (2022) | GCMT | 300–700 km | Mw 5.2–6.7 | 0.6 | Mw 6.7–7.8 | 1.1 |
| Mao et al. (2022) | IRIS | 300–700 km | Mw 4.0–6.9 | 0.7 | Mw 6.9–7.6 | 1.3 |

Table C5. Summary of observed b values and moment magnitude ranges from previous studies (Mao et al., 2022; Zhan, 2017) using global compilations of earthquake catalogs near warm subduction zones (including South America, the Philippines, Japan-Kuril, and Izu-Bonin-Mariana).

Okal & Kirby (1995) and Todes et al. (2021) attribute moment-dependent changes in b value to a two-stage fault saturation model with two critical moments M_{low} and M_{high} . At small moments below M_{low} where earthquakes are unlikely to saturate any fault dimension ($n = 3$), they observe b values approaching 1.5 implying faulting within a volumetric seismogenic zone ($D = 3$). At intermediate moments between M_{low} and M_{high} , they observe b values near 0.75 which is consistent with saturation in the transverse (i.e., all but length) dimensions. This is the L-model where slip grows with length ($n = 2$) along a one-dimensional seismogenic zone ($D = 1$). At large moments above M_{high} , they observe a return to b values near 1.5 but presume the carryover of a one-dimensional faulting region ($D = 1$), requiring the saturation of the fault in the transverse directions as well as the saturation of slip. This is equivalent to the W-model where length grows independently of slip ($n = 1$).

We use the back-projection method to image the spatiotemporal evolution of 19 deep-focus earthquakes within the Izu-Bonin subduction zone, thus independently constraining source properties such as rupture length and duration with no *a priori* assumptions of fault geometry and orientation. Using rupture length as a proxy for fault length L , we find that $M_0 \propto L^3$ provides the best fit for the deep-focus earthquakes imaged in this study (Figure C5). These rupture lengths are restricted to events with moment magnitudes between Mw 6.0 and 7.1, largely owing to limitations in imaging the finite rupture processes of small earthquakes and the relative

scarcity of larger ($M_w > 7$) events. We find that this range of moment magnitudes primarily operates within the intermediate range of moment magnitudes as defined in Table C5 ($M_w < 6.5\text{--}6.9$) with some overlap into large moment magnitudes ($M_w > 6.5\text{--}6.9$). This observation restricts the moment-length scaling parameter of intermediate moment earthquakes to $n = 3$, implying that fractal dimension D alone controls the observed b values of events in this moment range. Noting the estimates of moderate thermal parameter and the observations of higher b values near Izu-Bonin, the hypothesis that earthquakes rupture solely along thin, one-dimensional segments of the MOW with fractal dimension $D = 1$ likely deteriorates. Instead, we expect the MOW to have some finite thickness that accommodates rupture along both linear ($D = 1$) and planar ($D = 2$) faulting regions with no width saturation ($n = 3$), resulting in b values between 0.5 and 1.0. In other words, the seismogenic zones accommodating intermediate moment earthquakes in this region are not uniformly one- nor two-dimensional, especially given the structural complexity of the Izu-Bonin slab below $\sim 300\text{--}400$ km depth (Zhang et al., 2019) where the MOW is thought to exist within a narrow region $\sim 15\text{--}25$ km wide (Iidaka & Furukawa, 1994; Iidaka & Obara, 1997; Wiens et al., 1993) and taper substantially with depth (Devaux et al., 1997; Kirby et al., 1996). The coarse spatial binning necessary to estimate earthquake frequency at large magnitudes ultimately obscures the b value and fractal dimension D at any given point in a geographic region, necessitating average values to be estimated over large area or depth ranges. Should a study area encapsulate both linear ($D = 1$) and planar ($D = 2$) faulting regions into one b value observable, Aki (1981) predicts this b value to fall between 0.5 and 1.0.

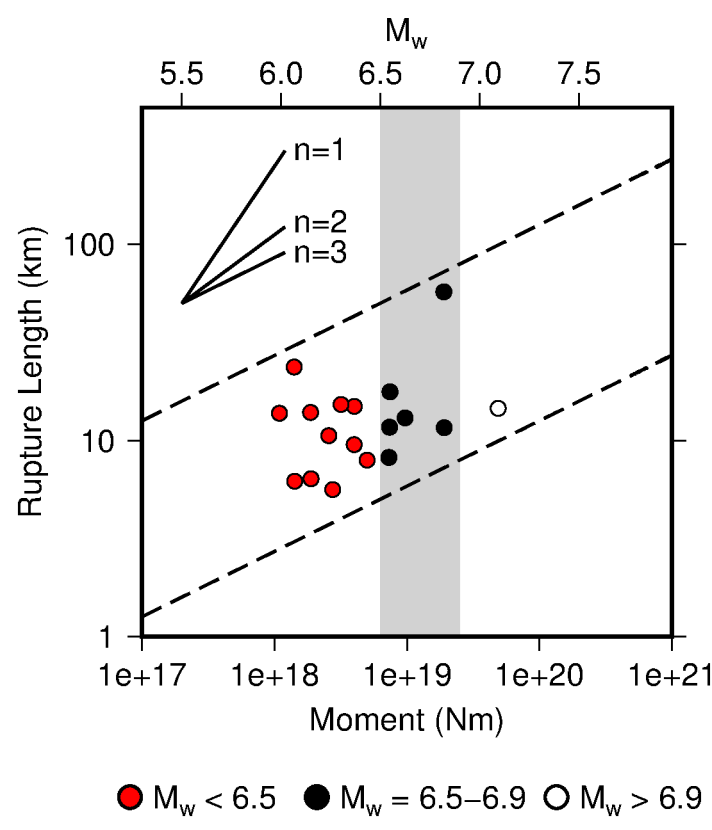


Figure C5. Moment-length plot for the rupture lengths constrained by the regional back-projection method. Dashed lines correspond to moment-length scaling parameter $n = 3$ and are scaled to bracket the data. The slopes corresponding to the scaling parameters $n = 1, 2, 3$ are shown with solid black lines. The gray areas outline M_w 6.5–6.9, the lower and upper bounds of the b value discontinuity observed by previous studies.

5.2. Rupture properties

Within the warmest slabs, the dual-mechanism hypothesis predicts that intermediate moment earthquakes rupture along a one-dimensional segment of the MOW via transformational faulting and large moment earthquakes rupture on a two-dimensional plane outside of the thin MOW segment via thermal runaway (Zhan, 2017). The MOW is located within the interior of the subducting slab and thus strikes and dips in approximately the same direction as the slab

itself. We obtain a value for slab strike at the nearest Slab2 (Hayes et al., 2018) point to each mainshock hypocenter and calculate an average slab strike of $155^\circ/335^\circ$ and an average slab dip of 56° in our study region.

Our regional back-projection results indicate that intermediate moment earthquakes ($M_w < 6.5$) rupture near the average slab strike (and inferred MOW strike) while large moment earthquakes ($M_w > 6.5$) rupture with no azimuthal dependence (Figure C6a). Our preferred explanation for this observation is the operation of two distinct mechanisms at intermediate and large moments. Within a thin MOW, intermediate moment earthquakes preferentially rupture along the slab strike direction and are likely accommodated entirely on the MOW via transformational faulting. As earthquakes increase in moment and faulting area, a critical threshold is reached at which ruptures can no longer be entirely accommodated on the thin MOW. Thus, large moment earthquakes must rupture into the surrounding slab via thermal runaway and are no longer restricted to rupture trends in the slab strike direction. Izu-Bonin is characterized by a moderate thermal parameter and we note this dependence is likely more apparent in warmer slabs (e.g., South America) where intermediate moment earthquakes are likely restricted to thinner MOW segments.

Our results constrain the mainshock rupture process in three spatial dimensions and allow the angle of the earthquake rupture from horizontal (0°) to be measured, which we subsequently call the rupture plunge. Our results indicate that the intermediate moment earthquakes transit a broad range of rupture plunge values while most large moment earthquakes occupy a relatively narrow range of rupture plunge values, most of which rupture at angles less than the smallest estimated value of slab dip (Figure C6b). Intermediate moment earthquake ruptures must therefore occur on a plane approximately parallel with the surface of the inferred MOW while

large moment ruptures largely occur on a shallowly dipping plane dissimilar to the orientation of the inferred MOW. These observations may again be attributed to the prevalence of transformational faulting of metastable olivine at intermediate moments and the transition to thermal runaway at larger moments. Indeed, the thermal runaway mechanism requires the positive feedback behavior between deformation-induced heating and temperature-dependent weakening—once initiated, slip causes localized heating that softens the surrounding material, resulting in further slip, heating, and weakening that drive catastrophic failure. Localized heating during thermal runaway may be favored towards warmer environments where higher ambient temperatures bring material closer to failure. Globally, large deep-focus earthquake ruptures extending beyond the MOW (e.g., Beck et al., 1995; Meng et al., 2014; Silver et al., 1995) and rupture propagation into material \sim 100–300°C warmer than temperatures typical of deep-focus seismicity have been observed (e.g., Fan et al., 2019; Jia et al., 2020; McGuire et al., 1997). Near Izu-Bonin, large moment and shallowly plunging ruptures (Figure C6b) likely extend beyond the MOW and transit a broad range of ambient temperatures, implicating failure via thermal runaway.

Thermal runaway is thought to initiate in the high stress regions surrounding the weak, fine-grained spinel that forms in cold slab cores (Karato et al., 2001). Failure via thermal runaway remains possible in warmer environments—or in the absence of a weak, fine-grained spinel core—given the bending moment of the slab as it impinges upon the lower mantle (660-km discontinuity) is large. Together with tomographic images showing the subhorizontal deflection of the Izu-Bonin slab as it approaches the lower mantle, the prominent slab tear and change in subduction geometry near 27°N (e.g., Zhang et al., 2019) may locally elevate the internal stresses within the subducting slab, promoting failure via thermal runaway. Further heating and

weakening may concentrate on the same high strength regions loaded by local heterogeneities in slab rheology and geometry, resulting in sustained earthquake rupture. Thermal runaway is necessary to explain the nucleation of aftershocks outside of the MOW (e.g., Kiser et al., 2021; Wiens et al., 1994), but the possibility of triggering thermal runaway following transformational faulting of the MOW remains a distinct possibility (e.g., Officer & Secco, 2020; Zhan, 2019). In both scenarios, a seismogenic zone that lies outside or exceeds the expected dimensions of the MOW precludes transformational faulting as the sole causal mechanism of deep-focus earthquakes. Near Izu-Bonin, the propagation of large moment ruptures away from the MOW indicates that thermal runaway likely prevails above a critical seismic moment. Thermal runaway requires rapid deformation over short time scales relative to the diffusion of heat (Karato et al., 2001). Small-scale thermal shear instabilities will diffuse heat more efficiently than large-scale instabilities, effectively inhibiting rupture growth at smaller moments. While thermal runaway may explain some isolated seismicity in highly stressed regions far away from a MOW, near Izu-Bonin we find that the restriction of intermediate moment ruptures to the inferred location of the MOW is more readily explained by transformational faulting.

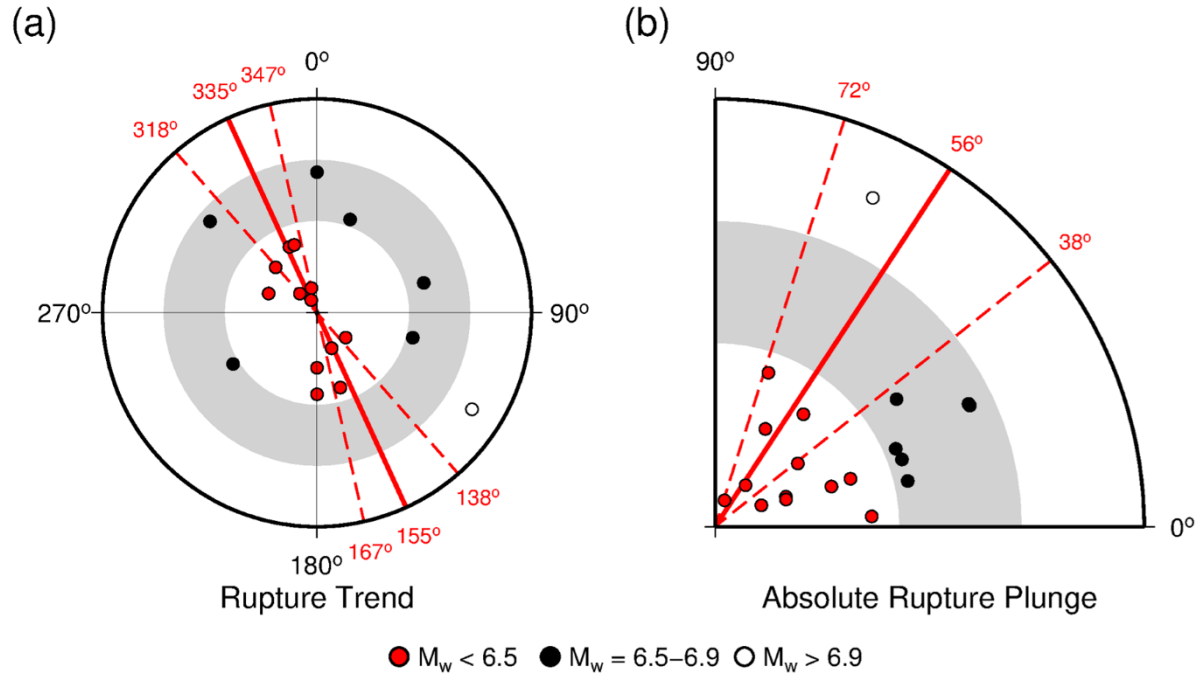


Figure C6. The relationship between (a) moment magnitude and rupture trend and (b) moment magnitude and the absolute value of rupture plunge. Rupture trend and plunge for each mainshock event are constrained by the regional back-projection method and are colored according to their GCMT-reported moment magnitude. The solid red lines indicate the average slab strike and dip in the vicinity of the mainshock hypocenters while the dashed red lines indicate the range of slab strikes and dips in the vicinity of the mainshock hypocenters. Slab strikes and dips are measured at the nearest Slab2 point to each mainshock hypocenter. The gray areas outline M_w 6.5–6.9, the lower and upper bounds of the b value discontinuity observed by previous studies (Table C5). The radius of each plot corresponds to moment magnitude, which increases outward from M_w 5.9 to 7.3.

5.3. Fault plane orientations

Centroid moment tensor (e.g., GCMT) solutions do not specify which of two nodal planes experience slip and additional information is required to determine the orientation of the

fault and auxiliary planes. This intrinsic ambiguity obscures otherwise revealing information such as fault geometry, slab composition, and the mechanics of faulting at depth. Mapped faults and aftershock distributions may reveal the fault planes of shallow earthquakes, but deep earthquakes occur on largely unknown fault structures and deep aftershocks are often scarce. The orientation of earthquake rupture properties in three-dimensional space observed in this study with respect to independently determined GCMT solutions can be used to determine the fault plane orientation of deep earthquakes. Of the 19 events imaged by this study, we find that 10 ruptures uniquely fit on a single fault plane, 2 ruptures fit on both nodal planes equally well, and 6 ruptures fit on neither nodal plane (Table C4). Discrepancies between GCMT solutions using intermediate- to long-period globally recorded seismic data (Ekström et al., 2012) and our back-projection results using high-frequency regionally recorded data are possible. Non-double couple solutions may additionally represent complex earthquake ruptures with multiple subevents (i.e., those spanning multiple fault segments) and such ruptures are difficult to fit to a single GCMT nodal plane. Among the events imaged in this study, disagreements arising from rupture complexity are likely secondary to methodological differences since most GCMT and U.S. Geological Survey (USGS: <https://earthquake.usgs.gov/>) moment tensor solutions are well approximated as double-couple sources (Figure CS4 and Table CS5). In this section, we will focus on the 10 GCMT solutions where slip on a single fault plane is well characterized (Figure C7).

The fault planes of all intermediate moment earthquakes ($M_w < 6.5$) follow the slab and inferred MOW strike and dip subvertically. Fault plane rakes indicate a wide range of left-lateral normal and reverse senses of motion (Figure C7). GCMT solutions and previous studies (e.g., Isacks & Molnar, 1971) indicate that downdip compression of the slab dominates within our

study region (2–3). The maximum compressive stress σ_1 is aligned with the subducting slab, possibly due to the resistance and subhorizontal deflection of the slab as it approaches the lower mantle. In the context of transformational faulting within the MOW, small lenticular packets of dense, transformed spinel, subsequently called anticracks, orient themselves perpendicularly to σ_1 and connect as a macroscopic shear zone that forms at an oblique angle to σ_1 (e.g., Green & Burnley, 1989; Houston, 2015). The formation of conjugate faults at angles $\sim 30^\circ$ – 45° from σ_1 are expected at great depths as shown by observational studies (e.g., Warren et al., 2007) and high pressure and temperature laboratory experiments (e.g., Burnley et al., 1991; Green & Burnley, 1989; Officer & Secco, 2020; Ohuchi et al., 2022). For a steeply dipping slab of ~ 45 – 60° along which σ_1 aligns (e.g., Izu-Bonin), one conjugate fault plane will dip at an angle of $\sim 90^\circ$, or subvertically as shown for intermediate moment earthquakes near Izu-Bonin (Figure C7b).

The fault planes of large moment earthquakes ($M_w > 6.5$) largely occur on the shallower of two nodal planes, striking east and raking at angles characteristic of right-lateral normal senses of motion (Figure C7). Should transformational faulting be the sole mechanism of deep-focus earthquakes, the relatively steep dip of the Izu-Bonin slab as well as the scaling of seismic moment with fault area would require a thicker MOW accommodating large moment earthquakes on shallowly dipping fault planes than the MOW hosting intermediate moment earthquakes on steeply dipping fault planes. However, estimated b values between 0.5 and 1.0 in our study region indicate that the MOW thickness saturates even for intermediate moment earthquakes. An adequately thick MOW accommodating the shallowly dipping fault planes of large moment events should readily host intermediate moment events, resulting in b values near 1.0 across all observable moments. While this may be the case near the coldest subducting slabs

(i.e., Tonga), we find such a scenario near Izu-Bonin improbable. Large moment events in our study region instead occur on shallowly dipping fault planes that extend beyond the boundaries of the MOW and produce ruptures that transit larger temperature gradients, necessitating propagation via thermal runaway and permitting growth to larger moment magnitudes.

Of the large moment events, we note the 302.2-km deep Mw 7.1 exception which ruptured with a plunge of approximately 64° and occurred on a fault plane dipping at approximately 86° . Should the MOW exist at these relatively shallow depths, it may be thicker on average than the MOW at deeper, warmer regions of the Izu-Bonin slab. In such a case, the thick MOW may entirely accommodate the large moment earthquake via transformational faulting, explaining the relatively steep rupture plunge. If instead the MOW does not exist at ~ 300 km depth, we would expect this event to exhibit a source process and causal mechanism more typical of shallower intermediate-depth earthquakes.

Myhill & Warren (2012) use a rupture directivity analysis to find shallowly dipping fault planes for 7 of the 9 Mw 5.8–7.1 deep-focus earthquakes near Izu-Bonin for which they identify or prefer a single fault plane, observing no relationship with moment. We use the back-projection method to find evidence of moment-dependent fault plane orientations for 9 of the 10 imaged deep-focus earthquakes. This disagreement, as well as the limited number of constrained fault planes found by both studies, warrants further investigation to determine the prevailing fault plane orientations of deep-focus earthquakes near Izu-Bonin. Preferentially subhorizontal fault plane orientations at deep-focus depths have been observed in regions with relatively planar subduction zone geometries (e.g., Warren et al., 2015). Observations of predominately subhorizontal fault planes near Izu-Bonin would represent a stark departure from observations of fault plane orientations in other complex subduction zones (e.g., Warren et al., 2007).

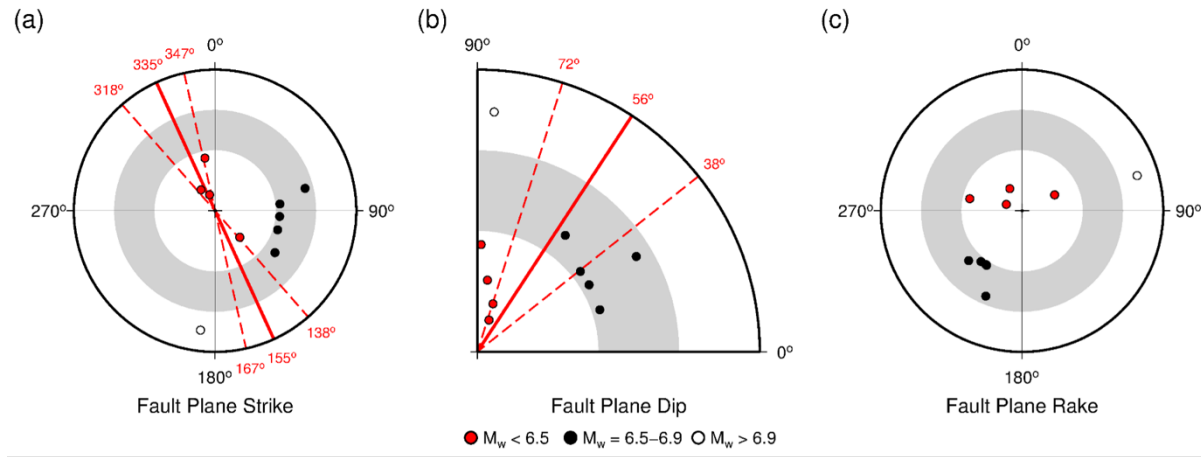


Figure C7. Moment relationships with fault plane (a) strike, (b) dip, and (c) rake. Events meeting the classification criteria for rupture occurring on a single fault plane (see Section 3.5) are shown and colored according to their GCMT-reported moment magnitude. The solid red lines indicate the average slab strike and dip in the vicinity of the mainshock hypocenters while the dashed red lines indicate the range of slab strikes and dips in the vicinity of the mainshock hypocenters. Slab strikes and dips are measured at the nearest Slab2 point to each mainshock hypocenter. The gray areas outline M_w 6.5–6.9, the lower and upper bounds of the b value discontinuity observed by previous studies (Table C5). The radius of each plot corresponds to moment magnitude, which increases outward from M_w 5.9 to 7.3.

6. Conclusions

We use the back-projection method and the Hi-net array to image the rupture properties of 19 $M_w > 6$ deep-focus earthquakes near Izu-Bonin. We find that rupture and fault plane properties of the imaged events depend on seismic moment. We use these observations in combination with the results of previous studies to infer properties of the metastable olivine wedge (MOW) within the interior of the Izu-Bonin slab, constraining possible causal mechanisms governing the occurrence of deep-focus earthquakes in this region. Izu-Bonin is a

strategic study region for its proximity to a nearby dense seismic network and a regional three-dimensional velocity model. An abundance of deep-focus earthquakes and the transitional thermal properties relative to global subduction zones in this region further allow the assessment of endmember hypotheses of deep-focus earthquake mechanisms.

In one such case where the MOW is an infinitesimally thin sheet on which transformational faulting is restricted, ruptures will coalesce on thin, linear features associated with the connection (i.e., failure) of spinel-filled anticracks embedded within the MOW sheet ($b = 0.5$ and $D = 1$). Passive rupture outside of these linked anticracks, and even outside of the MOW sheet itself (e.g., Zhan, 2017), may accommodate some fraction of the total moment release and allow slip to scale with both fault length and width on a one-dimensional fault. While rupture trend is limited in this case to the slab strike direction, the rupture plunge may vary extensively on the MOW sheet due to local variations in the properties controlling the creation and orientation of linked anticracks (e.g., ambient stress, pressure, temperature). In regions where the MOW is substantially thicker (i.e., Tonga), these anticracks can organize and fail along an additional spatial dimension, thus ruptures will instead occur on planar faults embedded within a three-dimensional MOW volume ($b = 1.0$ and $D = 2$). Here, neither rupture trend nor plunge may correlate with the slab and inferred MOW orientation since the MOW can accommodate rupture along its width, or perpendicular to slab strike. In regions such as Izu-Bonin, observed b values and estimates of thermal parameter are consistent with a MOW between these two endmember cases ($0.5 < b < 1.0$ and $1 < D < 2$). When averaged over the entire study region, the fractal dimension likely takes a fractional value that describes linked anticracks that only occasionally extend along the width direction of a MOW with finite thickness.

Knowing the moment-length scaling $M_0 \propto L^n$ where $n = 3$ (i.e., no width saturation) for intermediate moment events, and assuming this observation holds at large moments, changes in b value observations must originate from changes in the fractal dimension D . Large moment earthquakes occur on a shallowly dipping plane and exhibit b values near 1.0. When moment and rupture length exceed a critical size that can be accommodated by the MOW, thermal runaway extends rupture outside of the MOW. Unlike intermediate moment earthquake ruptures confined to preexisting weak zones (i.e., linked anticracks on the MOW), rupture via thermal runaway can proceed in any azimuthal direction and thus will try to fill the shallowly dipping plane on which they are observed ($b = 1.0$ and $D = 2$). While local variations in temperature and slab structure may change the preferred orientation of the thermal runaway rupture, these variations will be relatively minor compared to the bulk warming of material away from the cold slab core. Should thermal runaway preferentially occur along a plane defined by the local temperature gradient, events will propagate perpendicularly to the local isotherm contours, which themselves follow the slab and MOW orientation. High stress regions within the interior of the slab resulting from variations in slab rheology and geometry may be more likely to fail via thermal runaway and near Izu-Bonin, such ruptures occur along a shallowly dipping plane. While it remains unclear if thermal runaway initiates spontaneously or is triggered by transformational faulting within the MOW, large moment earthquakes rupturing away from the MOW on shallowly dipping fault planes necessitate the existence of rupture via thermal runaway.

Our results show that intermediate moment ($Mw < 6.5$) and large moment ($Mw > 6.5$) deep-focus earthquakes near Izu-Bonin exhibit rupture and fault plane properties indicative of two separate causative mechanisms above and below a critical moment. This critical moment is itself fundamentally controlled by the thickness of the MOW within the interior of the

subducting slab. Transformational faulting of metastable olivine likely dominates at intermediate moments while thermal runaway prevails at large moments where transformational faulting can no longer be accommodated on a MOW of finite thickness. Improvements in source imaging methods and instrumentation will extend this effort to a global distribution of subduction zones and robust investigations of the mechanisms controlling deep-focus earthquakes will undoubtedly improve our understanding of deep-focus rupture processes, slab structure, and subduction zone dynamics.

References

- Aki, K. (1981). A probabilistic synthesis of precursory phenomena. *Earthquake Prediction: An International Review*, 566–574. <https://doi.org/10.1029/ME004P0566>
- Anderson, E. M. (1905). The dynamics of faulting. *Transactions of the Edinburgh Geological Society*, 8(3), 387–402. <https://doi.org/10.1144/TRANSED.8.3.387>
- Beck, S. L., Silver, P., Wallace, T. C., & James, D. (1995). Directivity analysis of the Deep Bolivian Earthquake of June 9, 1994. *Geophysical Research Letters*, 22(16), 2257–2260. <https://doi.org/10.1029/95GL01089>
- Bondár, I., & Storchak, D. (2011). Improved location procedures at the International Seismological Centre. *Geophysical Journal International*, 186(3), 1220–1244. <https://doi.org/10.1111/J.1365-246X.2011.05107.X>
- Burnley, P. C., Green, H. W., & Prior, D. J. (1991). Faulting associated with the olivine to spinel transformation in Mg₂GeO₄ and its implications for deep-focus earthquakes. *Journal of Geophysical Research*, 96(B1), 425–443. <https://doi.org/10.1029/90JB01937>
- Chen, M., Niu, F., Liu, Q., Tromp, J., & Zheng, X. (2015). Multiparameter adjoint tomography of the crust and upper mantle beneath East Asia: 1. Model construction and comparisons. *Journal of Geophysical Research: Solid Earth*, 120(3), 1762–1786. <https://doi.org/10.1002/2014JB011638>
- de Kool, M., Rawlinson, N., & Sambridge, M. (2006). A practical grid-based method for tracking multiple refraction and reflection phases in three-dimensional heterogeneous media. *Geophysical Journal International*, 167(1), 253–270. <https://doi.org/10.1111/J.1365-246X.2006.03078.X/3/167-1-253-FIG012.GIF>

- DeMets, C., Gordon, R. G., & Argus, D. F. (2010). Geologically current plate motions. *Geophysical Journal International*, 181(1), 1–80. <https://doi.org/10.1111/j.1365-246X.2009.04491.x>
- Devaux, J. P., Schubert, G., & Anderson, C. (1997). Formation of a metastable olivine wedge in a descending slab. *Journal of Geophysical Research: Solid Earth*, 102(11), 24627–24637. <https://doi.org/10.1029/97JB02334>
- Dziewonski, A. M., Chou, T.-A., & Woodhouse, J. H. (1981). Determination of earthquake source parameters from waveform data for studies of global and regional seismicity. *Journal of Geophysical Research: Solid Earth*, 86(B4), 2825–2852. <https://doi.org/10.1029/JB086iB04p02825>
- Ekström, G., Nettles, M., & Dziewoński, A. M. (2012). The global CMT project 2004–2010: Centroid-moment tensors for 13,017 earthquakes. *Physics of the Earth and Planetary Interiors*, 200–201, 1–9. <https://doi.org/10.1016/J.PEPI.2012.04.002>
- Fan, W., Wei, S. S., Tian, D., McGuire, J. J., & Wiens, D. A. (2019). Complex and Diverse Rupture Processes of the 2018 Mw 8.2 and Mw 7.9 Tonga-Fiji Deep Earthquakes. *Geophysical Research Letters*, 46(5), 2434–2448. <https://doi.org/10.1029/2018GL080997>
- Frohlich, C. (2006). Deep Earthquakes. Cambridge University Press. <https://doi.org/10.1017/CBO9781107297562>
- Green, H. W., & Burnley, P. C. (1989). A new self-organizing mechanism for deep-focus earthquakes. *Nature* 1989 341:6244, 341(6244), 733–737. <https://doi.org/10.1038/341733a0>

Gutenberg, B., & Richter, C. F. (1944). Frequency of earthquakes in California. *Bulletin of the Seismological Society of America*, 34(4), 185–188.

<https://doi.org/10.1785/BSSA0340040185>

Hanks, T. C., & Kanamori, H. (1979). A moment magnitude scale. *Journal of Geophysical Research B: Solid Earth*, 84(B5), 2348–2350. <https://doi.org/10.1029/JB084IB05P02348>

Hayes, G. P., Moore, G. L., Portner, D. E., Hearne, M., Flamme, H., Furtney, M., & Smoczyk, G. M. (2018). Slab2, a comprehensive subduction zone geometry model. *Science*, 362(6410), 58–61. <https://doi.org/10.1126/science.aat4723>

Houston, H. (2015). Deep Earthquakes. *Treatise on Geophysics: Second Edition*, 4, 329–354. <https://doi.org/10.1016/B978-0-444-53802-4.00079-8>

Iidaka, T., & Furukawa, Y. (1994). Double seismic zone for deep earthquakes in the Izu-Bonin subduction zone. *Science*, 263(5150), 1116–1118. <https://doi.org/10.1126/SCIENCE.263.5150.1116>

Iidaka, T., & Obara, K. (1997). Seismological evidence for the existence of anisotropic zone in the metastable wedge inside the subducting Izu-Bonin slab. *Geophysical Research Letters*, 24(24), 3305–3308. <https://doi.org/10.1029/97GL03277>

Isacks, B., & Molnar, P. (1971). Distribution of stresses in the descending lithosphere from a global survey of focal-mechanism solutions of mantle earthquakes. *Reviews of Geophysics*, 9(1), 103–174. <https://doi.org/10.1029/RG009I001P00103>

Ishii, M. (2011). High-frequency rupture properties of the Mw 9.0 off the Pacific coast of Tohoku Earthquake. *Earth, Planets and Space*, 63(7), 609–614. <https://doi.org/10.5047/eps.2011.07.009>

Ishii, M., Shearer, P. M., Houston, H., & Vidale, J. E. (2005). Extent, duration and speed of the 2004 Sumatra-Andaman earthquake imaged by the Hi-Net array. *Nature*, 435(7044), 933–936. <https://doi.org/10.1038/nature03675>

Ishii, M., Shearer, P. M., Houston, H., & Vidale, J. E. (2007). Teleseismic P wave imaging of the 26 December 2004 Sumatra-Andaman and 28 March 2005 Sumatra earthquake ruptures using the Hi-net array. *Journal of Geophysical Research: Solid Earth*, 112(11), 1–16. <https://doi.org/10.1029/2006JB004700>

Jia, Z., Shen, Z., Zhan, Z., Li, C., Peng, Z., & Gurnis, M. (2020). The 2018 Fiji Mw 8.2 and 7.9 deep earthquakes: One doublet in two slabs. *Earth and Planetary Science Letters*, 531, 115997. <https://doi.org/10.1016/J.EPSL.2019.115997>

Kanamori, H., Anderson, D. L., & Heaton, T. H. (1998). Frictional melting during the rupture of the 1994 Bolivian earthquake. *Science*, 279(5352), 839–842. <https://doi.org/10.1126/SCIENCE.279.5352.839/ASSET/495DB2FD-CB31-4022-BED7-7848F8855ED5/ASSETS/GRAFIC/SE0786252001.JPG>

Karato, S., Riedel, M. R., & Yuen, D. A. (2001). Rheological structure and deformation of subducted slabs in the mantle transition zone: implications for mantle circulation and deep earthquakes. *Physics of the Earth and Planetary Interiors*, 127(1–4), 83–108. [https://doi.org/10.1016/S0031-9201\(01\)00223-0](https://doi.org/10.1016/S0031-9201(01)00223-0)

Kehoe, H. L., & Kiser, E. D. (2020). Evidence of a Supershear Transition Across a Fault Stepover. *Geophysical Research Letters*, 47(10), e2020GL087400. <https://doi.org/10.1029/2020GL087400>

- Kehoe, H. L., Kiser, E. D., & Okubo, P. G. (2019). The rupture process of the 2018 Mw 6.9 Hawai‘i earthquake as imaged by a genetic algorithm-based back-projection technique. *Geophysical Research Letters*, 46(5), 2467–2474. <https://doi.org/10.1029/2018GL080397>
- Kennett, B. L. N., & Engdahl, E. R. (1991). Traveltimes for global earthquake location and phase identification. *Geophysical Journal International*, 105(2), 429–465. <https://doi.org/10.1111/j.1365-246X.1991.tb06724.x>
- Kirby, S. H. (1987). Localized polymorphic phase transformations in high-pressure faults and applications to the physical mechanism of deep earthquakes. *Journal of Geophysical Research: Solid Earth*, 92(B13), 13789–13800. <https://doi.org/10.1029/JB092IB13P13789>
- Kirby, S. H., Stein, S., Okal, E. A., & Rubie, D. C. (1996). Metastable mantle phase transformations and deep earthquakes in subducting oceanic lithosphere. *Reviews of Geophysics*, 34(2), 261–306. <https://doi.org/10.1029/96RG01050>
- Kiser, E., & Ishii, M. (2017). Back-Projection Imaging of Earthquakes. *Annual Review of Earth and Planetary Sciences*, 45(1), 271–299. <https://doi.org/10.1146/annurev-earth-063016-015801>
- Kiser, E., Ishii, M., Langmuir, C. H., Shearer, P. M., & Hirose, H. (2011). Insights into the mechanism of intermediate-depth earthquakes from source properties as imaged by back projection of multiple seismic phases. *Journal of Geophysical Research: Solid Earth*, 116(6). <https://doi.org/10.1029/2010JB007831>
- Kiser, E., Kehoe, H., Chen, M., & Hughes, A. (2021). Lower Mantle Seismicity Following the 2015 Mw 7.9 Bonin Islands Deep-Focus Earthquake. *Geophysical Research Letters*, 48(13), e2021GL093111. <https://doi.org/10.1029/2021GL093111>

Krüger, F., & Ohrnberger, M. (2005). Tracking the rupture of the Mw = 9.3 Sumatra earthquake over 1,150 km at teleseismic distance. *Nature*, 435(7044), 937–939.

<https://doi.org/10.1038/nature03696>

Mandelbrot, B. B. (1967). How Long Is the Coast of Britain? Statistical Self-Similarity and Fractional Dimension. *Science*, 156(3775), 636–638.

<https://doi.org/10.1126/SCIENCE.156.3775.636>

Mandelbrot, B. B. (1977). Fractals : form, chance, and dimension.

Mandelbrot, B. B. (1983). The fractal geometry of nature.

Mao, G. L., Ferrand, T. P., Li, J., Zhu, B., Xi, Z., & Chen, M. (2022). Unsupervised machine learning reveals slab hydration variations from deep earthquake distributions beneath the northwest Pacific. *Communications Earth & Environment* 2022 3:1, 3(1), 1–9.

<https://doi.org/10.1038/s43247-022-00377-x>

McGuire, J. J., Wiens, D. A., Shore, P. J., & Bevis, M. G. (1997). The March 9, 1994 (M w 7.6), deep Tonga earthquake: Rupture outside the seismically active slab . *Journal of Geophysical Research: Solid Earth*, 102(B7), 15163–15182.

<https://doi.org/10.1029/96JB03185>

Meade, C., & Jeanloz, R. (1991). Deep-Focus Earthquakes and Recycling of Water into the Earth's Mantle. *Science*, 252(5002), 68–72.

<https://doi.org/10.1126/SCIENCE.252.5002.68>

Meng, L., Ampuero, J. P., & Bürgmann, R. (2014). The 2013 Okhotsk deep-focus earthquake: Rupture beyond the metastable olivine wedge and thermally controlled rise time near the edge of a slab. *Geophysical Research Letters*, 41(11), 3779–3785.

<https://doi.org/10.1002/2014GL059968>

- Myhill, R., & Warren, L. M. (2012). Fault plane orientations of deep earthquakes in the Izu-Bonin-Marianas subduction zone. *Journal of Geophysical Research: Solid Earth*, 117(B6), 6307. <https://doi.org/10.1029/2011JB009047>
- Obara, K., Kasahara, K., Hori, S., & Okada, Y. (2005). A densely distributed high-sensitivity seismograph network in Japan: Hi-net by National Research Institute for Earth Science and Disaster Prevention. *Review of Scientific Instruments*, 76(2), 021301. <https://doi.org/10.1063/1.1854197>
- Officer, T., & Secco, R. A. (2020). Detection of high P,T transformational faulting in Fe₂SiO₄ via in-situ acoustic emission: Relevance to deep-focus earthquakes. *Physics of the Earth and Planetary Interiors*, 300, 106429. <https://doi.org/10.1016/J.PEPI.2020.106429>
- Ogawa, M. (1987). Shear instability in a viscoelastic material as the cause of deep focus earthquakes. *Journal of Geophysical Research: Solid Earth*, 92(B13), 13801–13810. <https://doi.org/10.1029/JB092IB13P13801>
- Ohuchi, T., Higo, Y., Tange, Y., Sakai, T., Matsuda, K., & Irifune, T. (2022). In situ X-ray and acoustic observations of deep seismic faulting upon phase transitions in olivine. *Nature Communications* 2022 13:1, 13(1), 1–14. <https://doi.org/10.1038/s41467-022-32923-8>
- Okada, Y., Kasahara, K., Hori, S., Obara, K., Sekiguchi, S., Fujiwara, H., & Yamamoto, A. (2004). Recent progress of seismic observation networks in Japan - Hi-net, F-net, K-net and KiK-net -. *Earth, Planets and Space*, 56(8), xv–xxviii. <https://doi.org/10.1186/BF03353076/METRICS>
- Okal, E. A., & Kirby, S. H. (1995). Frequency-moment distribution of deep earthquakes; implications for the seismogenic zone at the bottom of slabs. *Physics of the Earth and Planetary Interiors*, 92(3–4), 169–187. [https://doi.org/10.1016/0031-9201\(95\)03037-8](https://doi.org/10.1016/0031-9201(95)03037-8)

- Pacheco, J. F., Scholz, C. H., & Sykes, L. R. (1992). Changes in frequency-size relationship from small to large earthquakes. *Nature* 1992 355:6355, 355(6355), 71–73.
<https://doi.org/10.1038/355071a0>
- Prieto, G. A., Florez, M., Barrett, S. A., Beroza, G. C., Pedraza, P., Blanco, J. F., & Poveda, E. (2013). Seismic evidence for thermal runaway during intermediate-depth earthquake rupture. *Geophysical Research Letters*, 40(23), 6064–6068.
<https://doi.org/10.1002/2013GL058109>
- Raleigh, C. B., & Paterson, M. S. (1965). Experimental deformation of serpentinite and its tectonic implications. *Journal of Geophysical Research*, 70(16), 3965–3985.
<https://doi.org/10.1029/JZ070I016P03965>
- Romanowicz, B., & Rundle, J. B. (1993). On scaling relations for large earthquakes. *Bulletin of the Seismological Society of America*, 83(4), 1294–1297.
<https://doi.org/10.1785/BSSA0830041294>
- Scholz, C. H. (1982). Scaling laws for large earthquakes: Consequences for physical models. *Bulletin of the Seismological Society of America*, 72(1), 1–14.
<https://doi.org/10.1785/BSSA0720010001>
- Scholz, C. H. (1997). Size distributions for large and small earthquakes. *Bulletin of the Seismological Society of America*, 87(4), 1074–1077.
<https://doi.org/10.1785/BSSA0870041074>
- Silver, P. G., Beck, S. L., Wallace, T. C., Meade, C., Myers, S. C., James, D. E., Kuehnel, R., Silver, P. G., James, D. E., Kuehnel, R., Beck, S. L., Wallace, T. C., Myers, S. C., & Arizona, S. (1995). Rupture Characteristics of the Deep Bolivian Earthquake of 9 June

1994 and the Mechanism of Deep-Focus Earthquakes. *Science*, 268(5207), 69–73.

<https://doi.org/10.1126/SCIENCE.268.5207.69>

Todes, J. P., Okal, E. A., & Kirby, S. H. (2021). Frequency-size distributions of Wadati-Benioff zone and near-boundary intraplate earthquakes: Implications for intermediate and deep seismicity. *Physics of the Earth and Planetary Interiors*, 321, 106707.

<https://doi.org/10.1016/J.PEPI.2021.106707>

Wadati, K. (1928). Shallow and deep earthquakes. *Geophys. Mag.*, 1(1), 162–202.

Wang, D., Takeuchi, N., Kawakatsu, H., & Mori, J. (2016). Estimating high frequency energy radiation of large earthquakes by image deconvolution back-projection. *Earth and Planetary Science Letters*, 449, 155–163. <https://doi.org/10.1016/J.EPSL.2016.05.051>

Warren, L. M., Baluyut, E. C., Osburg, T., Lisac, K., & Kokkinen, S. (2015). Fault plane orientations of intermediate-depth and deep-focus earthquakes in the Japan-Kuril-Kamchatka subduction zone. *Journal of Geophysical Research: Solid Earth*, 120(12), 8366–8382. <https://doi.org/10.1002/2015JB012463>

Warren, L. M., Hughes, A. N., & Silver, P. G. (2007). Earthquake mechanics and deformation in the Tonga-Kermadec subduction zone from fault plane orientations of intermediate- And deep-focus earthquakes. *Journal of Geophysical Research: Solid Earth*, 112(5).

<https://doi.org/10.1029/2006JB004677>

Wiens, D. A. (2001). Seismological constraints on the mechanism of deep earthquakes: Temperature dependence of deep earthquake source properties. *Physics of the Earth and Planetary Interiors*, 127(1–4), 145–163. [https://doi.org/10.1016/S0031-9201\(01\)00225-4](https://doi.org/10.1016/S0031-9201(01)00225-4)

Wiens, D. A., & Gilbert, H. J. (1996). Effect of slab temperature on deep-earthquake aftershock productivity and magnitude–frequency relations. *Nature*, 384(6605), 153–156.
<https://doi.org/10.1038/384153a0>

Wiens, D. A., McGuire, J. J., & Shore, P. J. (1993). Evidence for transformational faulting from a deep double seismic zone in Tonga. *Nature* 1993 364:6440, 364(6440), 790–793.
<https://doi.org/10.1038/364790a0>

Wiens, D. A., McGuire, J. J., Shore, P. J., Bevis, M. G., Draunidalo, K., Prasad, G., & Helu, S. P. (1994). A deep earthquake aftershock sequence and implications for the rupture mechanism of deep earthquakes. *Nature* 1994 372:6506, 372(6506), 540–543.
<https://doi.org/10.1038/372540a0>

Zhan, Z. (2017). Gutenberg–Richter law for deep earthquakes revisited: A dual-mechanism hypothesis. *Earth and Planetary Science Letters*, 461, 1–7.
<https://doi.org/10.1016/J.EPSL.2016.12.030>

Zhan, Z. (2019). Mechanisms and Implications of Deep Earthquakes.
<https://doi.org/10.1146/annurev-earth-053018>

Zhang, H., Wang, F., Myhill, R., & Guo, H. (2019). Slab morphology and deformation beneath Izu-Bonin. *Nature Communications* 2019 10:1, 10(1), 1–8.
<https://doi.org/10.1038/s41467-019-09279-7>

Supporting Information

Introduction

The supporting information includes text describing the Global Centroid Moment Tensor (GCMT: Dziewonski et al., 1981; Ekström et al., 2012) epsilon value (Text CS1). Also included are four figures supporting the main text (Figures CS1–CS4), and five tables supporting the main text (Tables CS1–CS5). Data used to create the following figures and tables were received from the Incorporated Research Institutions for Seismology (IRIS: <https://ds.iris.edu/>) consortium in January 2023 (Figures CS1–CS3 and Tables CS1–CS4), the GCMT Project in January 2023 (Figure CS4 and Table CS5), and the U.S. Geological Survey (USGS: <https://earthquake.usgs.gov/>) in January 2023 (Figure CS4 and Table CS5), unless otherwise stated. The data was processed according to the steps described in the methods section of the main text.

Text CS1.

Consider the moment tensor \mathbf{M} of the form:

$$\mathbf{M} = \begin{bmatrix} \lambda_1 & 0 & 0 \\ 0 & \lambda_2 & 0 \\ 0 & 0 & \lambda_3 \end{bmatrix} \text{ where } |\lambda_1| \geq |\lambda_2| \geq |\lambda_3|$$

A perfect double couple source is represented by the following eigenvalues:

$$\lambda_1 = -\lambda_2 \text{ and } \lambda_3 = 0$$

Moment tensor solutions using real data, however, are rarely perfect double couples.

Decomposing the moment tensor yields:

$$\begin{bmatrix} \lambda_1 & 0 & 0 \\ 0 & \lambda_2 & 0 \\ 0 & 0 & \lambda_3 \end{bmatrix} = \frac{\lambda_1 + \lambda_2 + \lambda_3}{3} \begin{bmatrix} 1 & 0 & 0 \\ 0 & 1 & 0 \\ 0 & 0 & 1 \end{bmatrix} + \begin{bmatrix} \lambda'_1 & 0 & 0 \\ 0 & \lambda'_2 & 0 \\ 0 & 0 & \lambda'_3 \end{bmatrix} \text{ where } |\lambda'_1| \geq |\lambda'_2| \geq |\lambda'_3|$$

The first term on the right-hand side is the isotropic component and the second term on the right-hand side is the deviatoric moment tensor, the latter of which may be decomposed in many ways, including into the pure double couple and compensated linear vector dipole (CLVD) components:

$$\begin{bmatrix} \lambda'_1 & 0 & 0 \\ 0 & \lambda'_2 & 0 \\ 0 & 0 & \lambda'_3 \end{bmatrix} = \begin{bmatrix} \lambda'_1 + \frac{\lambda'_3}{2} & 0 & 0 \\ 0 & -\lambda'_1 - \frac{\lambda'_3}{2} & 0 \\ 0 & 0 & 0 \end{bmatrix} + \begin{bmatrix} -\frac{\lambda'_3}{2} & 0 & 0 \\ 0 & -\frac{\lambda'_3}{2} & 0 \\ 0 & 0 & \lambda'_3 \end{bmatrix}$$

The prevalence of the double couple and CLVD components are quantified using the epsilon (ϵ) value

$$\epsilon = \frac{\lambda'_3}{\lambda'_1}$$

where $\epsilon = 0$ represents a pure double couple source and $\epsilon = \pm 0.5$ represents a pure CLVD source. The prevalence of the double couple component in USGS moment tensor solutions are instead reported as a percentage between 0% and 100%.

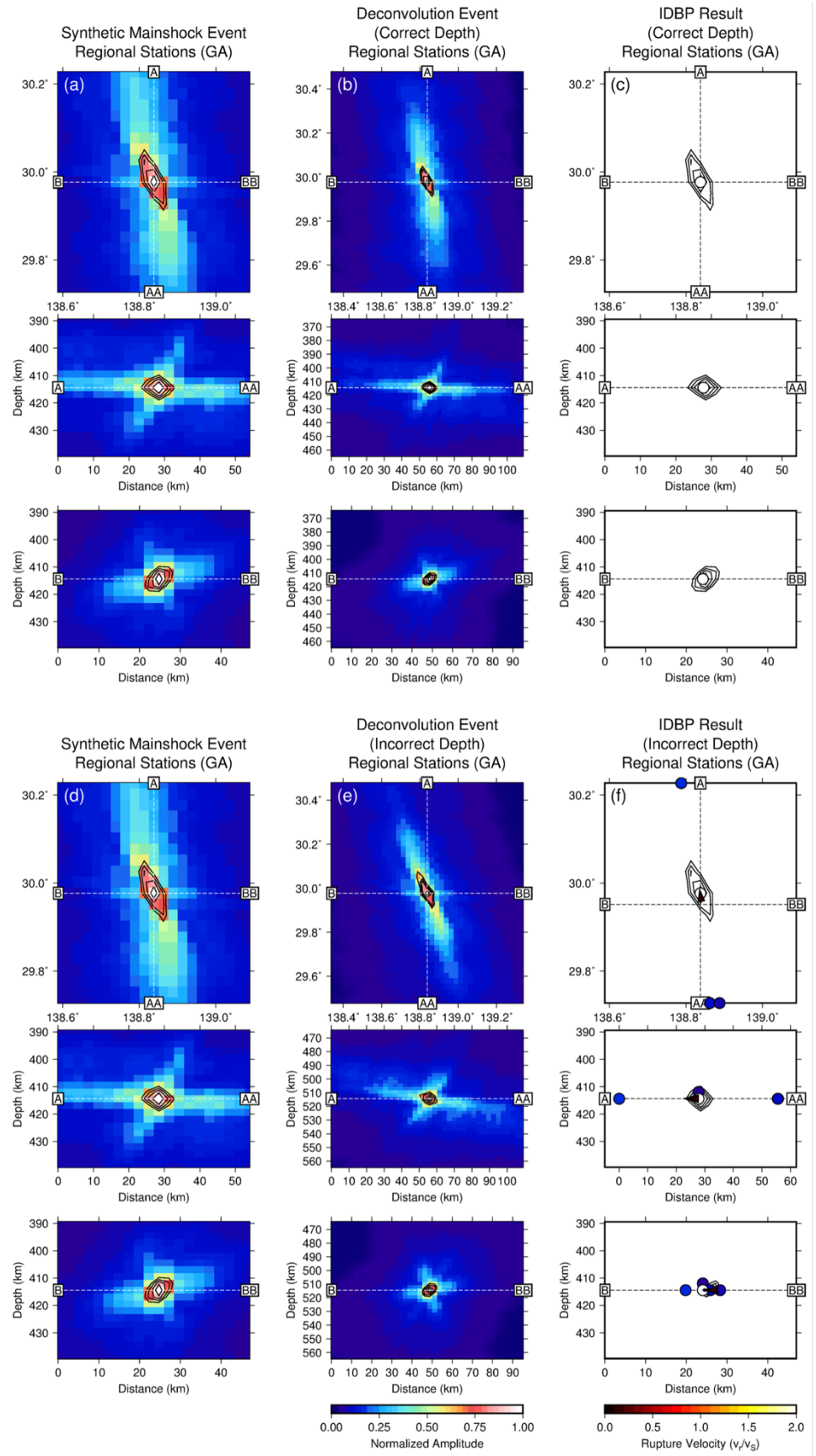


Figure CS1. Synthetic IDBP results using deconvolution events located at different depths.

(a–c) Synthetically generated mainshock and deconvolution events consisting of a spatiotemporal point source at the hypocenter and origin time of the 2013 Mw 6.5 mainshock event produce an IDBP result recovering of single source at the same hypocenter and origin time. (d–f) The same synthetically generated mainshock event and a deconvolution event with a hypocenter located 100 km below the 2013 Mw 6.5 mainshock event produce an IDBP result recovering a fictitious rupture process.

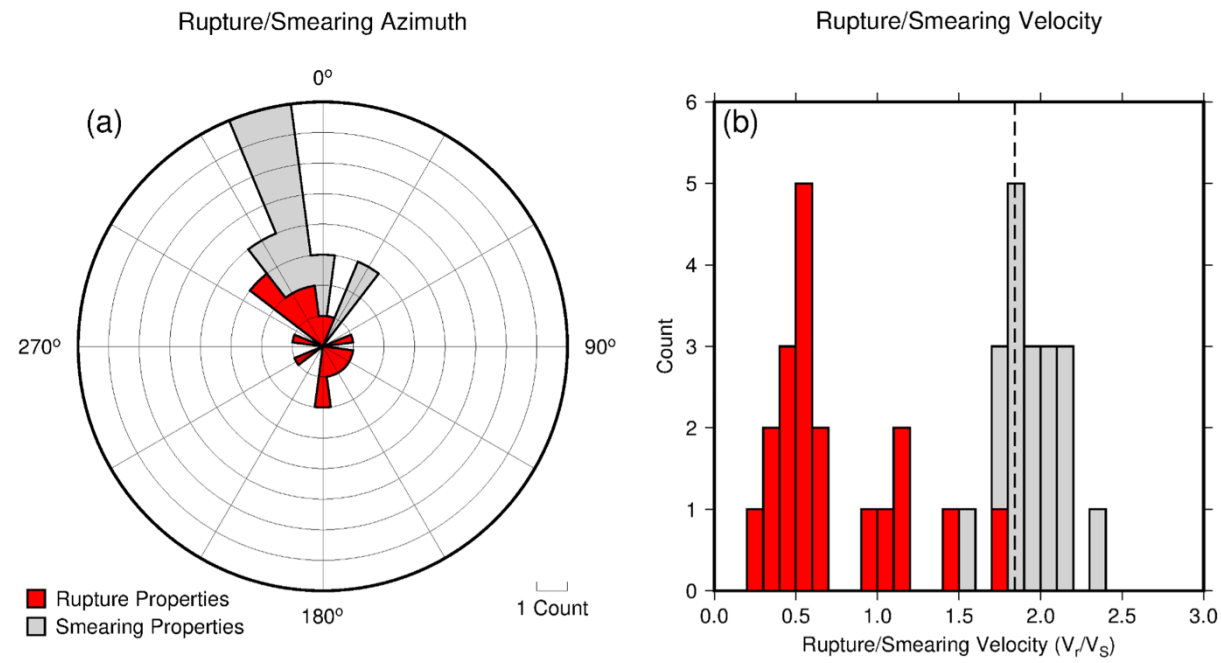


Figure CS2. Rupture and smearing properties of the mainshock events imaged by this study.

(a) The azimuth of each rupture process and smearing artifact are shown in red and gray, respectively. The smearing artifact occurs along the ray path, or towards the north in this study. (b) The velocity of each rupture process and smearing artifact are shown in red and gray, respectively. The smearing artifact manifests at the speed of the seismic phase used in

the back-projection analysis, or at P-wave speeds near $1.8 Vs$ in our study region. Our IDBP method resolves the true rupture process of each mainshock event and imaged rupture properties show minimal overlap with expected smearing properties.

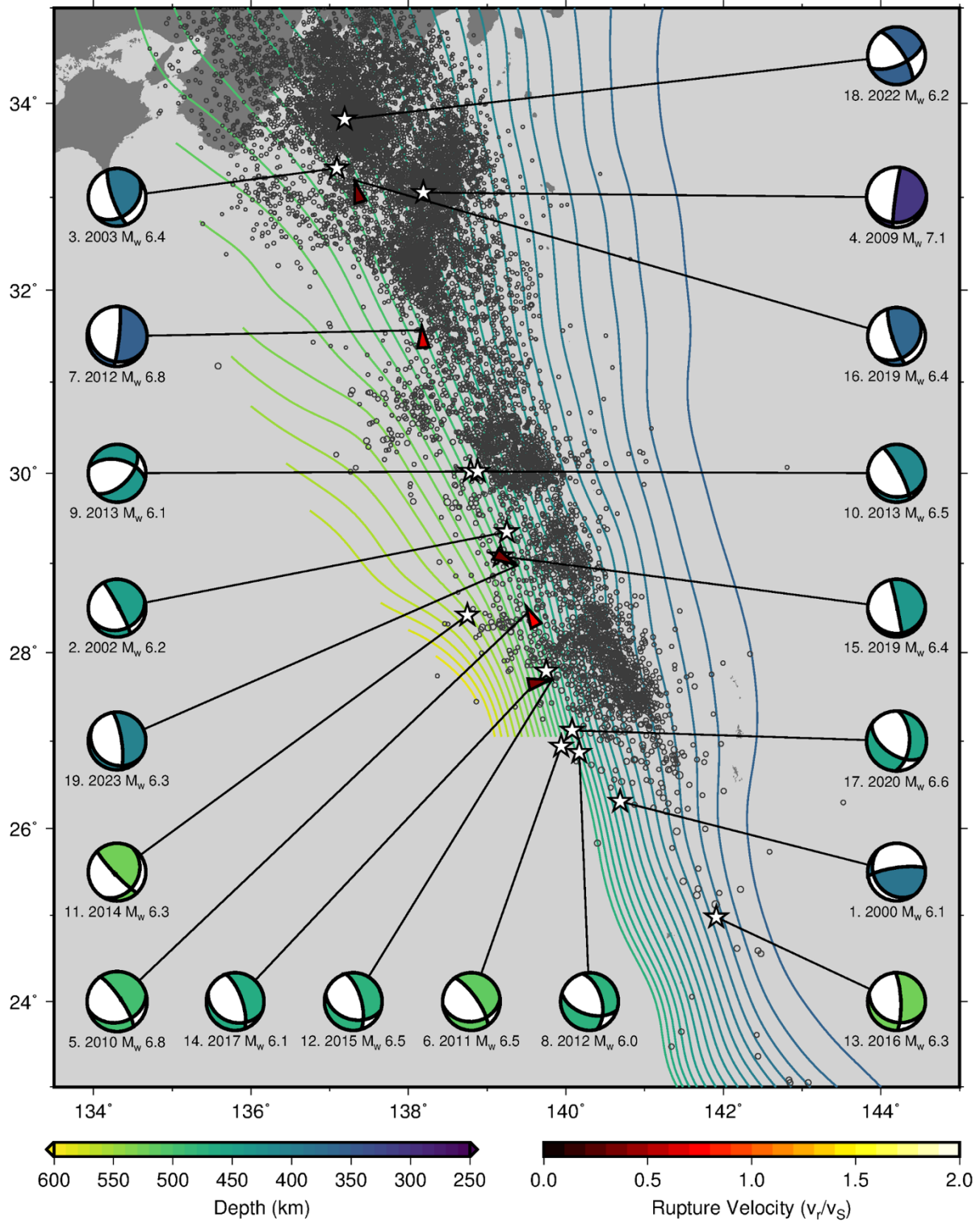


Figure CS3. Map summarizing the global back-projection results. The depth-colored contours show the subducting slabs (Slab2: Hayes et al., 2018). The magnitude-scaled black open

circles show all Japan Meteorological Agency (JMA: https://www.data.jma.go.jp/svd/eqev/data/bulletin/hypo_e.html) catalogued seismicity with depth greater than 250 km between the years 2000–2020. The colored arrows show the rupture speed and direction as determined by the two-dimensional global back-projection analysis. The arrows are colored by their rupture velocity, normalized to the local shear wave speed at the observed rupture depth. White stars are plotted in place of colored arrows if the rupture process is not resolved by the global back-projection analysis and is instead imaged as a spatiotemporal point source at the prescribed hypocenter and origin time. The depth-colored GCMT solutions associated with each event are plotted at the edge of the figure for clarity.

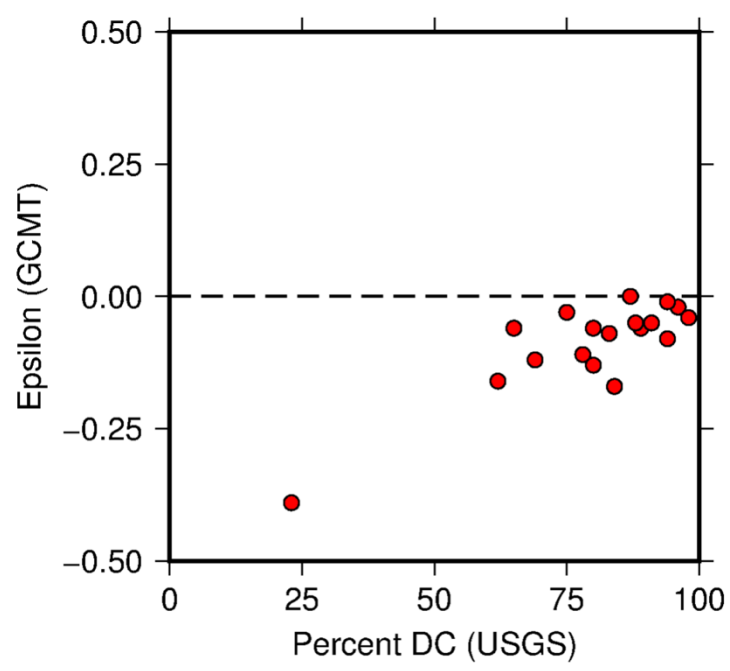


Figure CS4. Double couple components of the mainshock events imaged in this study. Pure double couple sources are indicated by an epsilon value of 0.00 (GCMT) and a percent DC value of 100% (USGS).

| Event ID | Mainshock Origin Time | Mainshock Mw (GCMT) | Mainshock Grid Volume Dimensions | Mainshock Grid Volume Spacing |
|----------|-----------------------|---------------------|----------------------------------|-------------------------------|
| 1 | 2000-10-27 04:21:53 | 6.1 | 1.50°×0.70°×100 km | 0.050°×0.050°×5.0 km |
| 2 | 2002-08-02 23:11:38 | 6.2 | 0.50°×0.50°×50 km | 0.025°×0.025°×2.5 km |
| 3 | 2003-11-12 08:26:43 | 6.4 | 0.50°×0.50°×50 km | 0.025°×0.025°×2.5 km |
| 4 | 2009-08-09 10:55:56 | 7.1 | 0.50°×0.50°×50 km | 0.025°×0.025°×2.5 km |
| 5 | 2010-11-30 03:24:41 | 6.8 | 2.00×1.00°×70 km | 0.050°×0.050°×5.0 km |
| 6 | 2011-01-12 21:32:54 | 6.5 | 0.50°×0.50°×30 km | 0.025°×0.025°×2.5 km |
| 7 | 2012-01-01 05:27:55 | 6.8 | 1.50°×0.75°×100 km | 0.050°×0.050°×5.0 km |
| 8 | 2012-05-26 21:48:09 | 6.0 | 0.60°×0.60°×50 km | 0.025°×0.025°×2.5 km |
| 9 | 2013-04-21 03:22:16 | 6.1 | 0.60°×0.60°×50 km | 0.025°×0.025°×2.5 km |
| 10 | 2013-09-04 00:18:24 | 6.5 | 0.50°×0.50°×50 km | 0.025°×0.025°×2.5 km |
| 11 | 2014-06-30 19:55:33 | 6.3 | 0.50°×0.50°×50 km | 0.025°×0.025°×2.5 km |
| 12 | 2015-06-23 12:18:30 | 6.5 | 1.20°×0.45°×57 km | 0.030°×0.030°×3.0 km |
| 13 | 2016-08-04 16:24:33 | 6.3 | 1.00°×1.00°×100 km | 0.050°×0.050°×5.0 km |
| 14 | 2017-09-07 17:26:49 | 6.1 | 0.50°×0.50°×70 km | 0.025°×0.025°×2.5 km |
| 15 | 2019-06-04 04:39:17 | 6.4 | 0.90°×0.40°×50 km | 0.025°×0.025°×2.5 km |
| 16 | 2019-07-27 18:31:07 | 6.4 | 0.50°×0.50°×70 km | 0.025°×0.025°×2.5 km |
| 17 | 2020-04-18 08:25:37 | 6.6 | 0.70°×0.50°×50 km | 0.025°×0.025°×2.5 km |
| 18 | 2022-11-14 08:08:26 | 6.2 | 0.50°×0.50°×50 km | 0.025°×0.025°×2.5 km |
| 19 | 2023-01-16 04:49:52 | 6.4 | 0.50°×0.50°×50 km | 0.025°×0.025°×2.5 km |

Table CS1: Back-projection grid volume dimensions and spacing for each mainshock presented

in this study.

| Event ID | Alignment Event Origin Time | Alignment Event Mw (IRIS) | Alignment Event Latitude (°N) | Alignment Event Longitude (°E) | Alignment Event Depth (km) |
|----------|-----------------------------|---------------------------|-------------------------------|--------------------------------|----------------------------|
| 1 | 2017-06-26 17:42:06 | 4.2 | 26.2336 | 140.6635 | 406.97 |
| 2 | 2015-01-25 10:41:14 | 5.3 | 29.2124 | 139.4683 | 426.8 |
| 3 | 2005-02-22 11:20:24 | 5.6 | 33.1993 | 137.1837 | 371.8 |
| 4 | 2009-12-09 16:06:00 | 4.9 | 33.051 | 137.9458 | 310.9 |
| 5 | 2007-07-31 12:58:29 | 5.4 | 28.2415 | 139.0192 | 510.7 |
| 6 | 2014-03-13 23:12:55 | 4.8 | 26.9149 | 140.1868 | 525.6 |
| 7 | 2020-07-06 18:19:09 | 5.6 | 31.5174 | 138.1221 | 386.89 |
| 8 | 2018-02-05 20:56:22 | 5.3 | 27.0011 | 140.1845 | 467.22 |
| 9 | 2007-09-07 09:31:00 | 4.8 | 29.9809 | 138.6886 | 422.8 |
| 10 | 2007-09-07 09:31:00 | 4.8 | 29.9809 | 138.6886 | 422.8 |
| 11 | 2007-07-31 12:58:29 | 5.4 | 28.2415 | 139.0192 | 510.7 |
| 12 | 2010-07-30 20:43:05 | 5.3 | 27.7418 | 139.7494 | 501.4 |

| | | | | | |
|----|---------------------|-----|---------|----------|--------|
| 13 | 2014-03-14 16:28:58 | 4.9 | 25.117 | 141.6632 | 520.7 |
| 14 | 2010-07-30 20:43:05 | 5.3 | 27.7418 | 139.7494 | 501.4 |
| 15 | 2015-01-25 10:41:14 | 5.3 | 29.2124 | 139.4683 | 426.8 |
| 16 | 2009-12-09 16:06:00 | 4.9 | 33.051 | 137.9458 | 310.9 |
| 17 | 2018-02-05 20:56:22 | 5.3 | 27.0011 | 140.1845 | 467.22 |
| 18 | 2021-01-15 13:38:19 | 5.2 | 33.8669 | 137.2129 | 357.77 |
| 19 | 2015-01-25 10:41:14 | 5.3 | 29.2124 | 139.4683 | 426.8 |

Table CS2: Alignment events used for each mainshock back-projection analysis.

| Event ID | Station Selection Event Origin Time | Station Selection Event Mw (IRIS) | Station Selection Event Latitude (°N) | Station Selection Event Longitude (°E) | Station Selection Event Depth (km) |
|----------|-------------------------------------|-----------------------------------|---------------------------------------|--|------------------------------------|
| 1 | 2016-04-22 00:28:22 | 4.2 | 26.3079 | 140.5803 | 398.59 |
| 2 | 2006-01-03 01:10:53 | 4.7 | 29.1624 | 139.442 | 418.1 |
| 3 | 2005-12-14 01:19:45 | 4.7 | 33.2257 | 137.0285 | 386.3 |
| 4 | 2014-08-20 19:38:25 | 5.4 | 33.1969 | 138.1144 | 307.9 |
| 5 | 2007-01-17 09:28:25 | 4.6 | 28.2557 | 139.1537 | 513.6 |
| 6 | 2016-01-21 07:17:14 | 4.2 | 26.9935 | 140.1832 | 490.38 |
| 7 | 2008-10-09 10:44:16 | 4.3 | 31.5053 | 138.1889 | 377.4 |
| 8 | 2016-01-21 07:17:14 | 4.2 | 26.9935 | 140.1832 | 490.38 |
| 9 | 2014-02-02 13:48:49 | 4.5 | 29.9279 | 138.6847 | 460.6 |
| 10 | 2014-02-02 13:48:49 | 4.5 | 29.9279 | 138.6847 | 460.6 |
| 11 | 2007-01-17 09:28:25 | 4.6 | 28.2557 | 139.1537 | 513.6 |
| 12 | 2012-10-12 21:10:58 | 4.5 | 27.7615 | 139.7629 | 491.7 |
| 13 | 2005-12-02 10:19:36 | 4.4 | 25.0728 | 141.6165 | 522 |
| 14 | 2012-10-12 21:10:58 | 4.5 | 27.7615 | 139.7629 | 491.7 |
| 15 | 2006-01-03 01:10:53 | 4.7 | 29.1624 | 139.442 | 418.1 |
| 16 | 2014-08-20 19:38:25 | 5.4 | 33.1969 | 138.1144 | 307.9 |
| 17 | 2016-01-21 07:17:14 | 4.2 | 26.9935 | 140.1832 | 490.38 |
| 18 | 2013-08-12 16:25:40 | 4.7 | 33.7752 | 137.1515 | 357.4 |
| 19 | 2006-01-03 01:10:53 | 4.7 | 29.1624 | 139.442 | 418.1 |

Table CS3: Station selection events used for each mainshock back-projection analysis.

| Event ID | Origin Time | Vr (km/s) | Vr/Vs | Rupture Azimuth (°) |
|----------|---------------------|-----------|-------|---------------------|
| 5 | 2010-11-30 03:24:41 | 3.8 | 0.7 | 333 |
| 7 | 2012-01-01 05:27:55 | 2.9 | 0.6 | 356 |
| 12 | 2015-06-23 12:18:30 | 1.6 | 0.3 | 78 |
| 16 | 2019-07-27 18:31:07 | 1.4 | 0.3 | 344 |
| 19 | 2023-01-16 04:49:52 | 1.5 | 0.3 | 118 |

Table CS4. Mainshock rupture properties determined by the teleseismic back-projection analysis.

| Event ID | Origin Time | Epsilon (GCMT) | Percent DC (USGS) |
|----------|---------------------|----------------|-------------------|
| 1 | 2000-10-27 04:21:53 | -0.39 | 23% |
| 2 | 2002-08-02 23:11:38 | -0.11 | 78% |
| 3 | 2003-11-12 08:26:43 | -0.02 | 96% |
| 4 | 2009-08-09 10:55:56 | -0.12 | 69% |
| 5 | 2010-11-30 03:24:41 | -0.06 | 65% |
| 6 | 2011-01-12 21:32:54 | -0.03 | 75% |
| 7 | 2012-01-01 05:27:55 | -0.01 | 94% |
| 8 | 2012-05-26 21:48:09 | -0.04 | 98% |
| 9 | 2013-04-21 03:22:16 | -0.13 | 80% |
| 10 | 2013-09-04 00:18:24 | -0.11 | 78% |
| 11 | 2014-06-30 19:55:33 | -0.06 | 80% |
| 12 | 2015-06-23 12:18:30 | -0.05 | 91% |
| 13 | 2016-08-04 16:24:33 | -0.16 | 62% |
| 14 | 2017-09-07 17:26:49 | 0.00 | 87% |
| 15 | 2019-06-04 04:39:17 | -0.06 | 89% |
| 16 | 2019-07-27 18:31:07 | -0.17 | 84% |
| 17 | 2020-04-18 08:25:37 | -0.07 | 83% |
| 18 | 2022-11-14 08:08:26 | -0.08 | 94% |
| 19 | 2023-01-16 04:49:52 | -0.05 | 88% |

Table CS5. Epsilon (GCMT) and percent DC (USGS) values indicating the double couple component of each mainshock events imaged in this study.